DEPARTAMENTO DE ASTROFÍSICA

Universidad de La Laguna

Solar abundances from three-dimensional empirical models

Memoria que presenta
Dña. Melania Cubas Armas
para optar al grado de
Doctor por la Universidad de La Laguna.

Trabajo dirigido por el Dr. Andrés Asensio Ramos
y codirigido por el Dr. Héctor Socas Navarro.

INSTITUTO Ð ASTROFÍSICA Ð CANARIAS
junio de 2019

Examination date: July, 2019
Thesis supervisor: Dr. Andrés Asensio Ramos
Thesis co-supervisor: Dr. Héctor Socas Navarro

ISBN: xx-xxx-xxxx-x
Depósito legal: TF-xxxx/2019
Part of the material included in this document has been already published.

Agradecimientos

En primer lugar, me gustaría agradecer a la Fundación la Caixa por realizar su convocatoria Severo Ochoa, gracias a la cuál he podido llevar a cabo mi tesis doctoral. De igual modo, quiero agradecer al Instituto de Astrofísica de Canarias por darme la oportunidad de realizar este proyecto.

Deseo agradecer también a mis directores de tesis, Andrés Asensio y Héctor Socas. Por diseñar el proyecto, y por orientarme y atender mis dudas durante estos casi cinco años.

Por colaborar conmigo, por su amabilidad y por dedicarme parte de su tiempo, mi más sincero agradecimiento a Nikola Vitas y Damian Fabbian.

Por revisar cuidadosamente este texto y por las sugerencias que me ha brindado, agradezco también a Carlos Allende.

Además, quiero agradecer al grupo de doctorandos, con los que he compartido muy buenos momentos. Agradezco en particular a mis compañeros de despacho, por crear un entorno de trabajo donde sentirnos a gusto; y en especial, a Carlos, por estar dispuesto siempre a discutir las dudas, ha sido muy constructivo.

Por otra parte, quiero agradecer a mi madre y a mi padre, que me han apoyado, me han brindado palabras de ánimo y han mostrado mucha paciencia y comprensión.

Por último, quiero agradecer a mis amigas: Cris, que siempre ha estado presente, ayudándome y confiando en mí; Laia, por nuestros emails interminables, que demuestran que la distancia no afecta a la amistad; y a Seni (Nai), Auxi, Trini, y Nati, que se han mantenido presentes en mi vida, a veces, incluso a pesar de mi misma. Gracias por vuestra comprensión y paciencia.

¡Muchas gracias a todas y todos!

Resumen

El estudio de las abundancias solares se remonta al análisis de Russell de 1929 y, desde entonces, se ha vuelto un tema muy relevante para la astrofísica en general. Esto es debido a que conocer la composición química del Sol es fundamental para construir modelos precisos de la atmósfera y el interior del Sol y de otras estrellas. Además, la composición solar actual es crucial para determinar la composición del Sol inicial y predecir cuál ha sido y será su evolución y su estructura interna. Por otra parte, las abundancias solares se utilizan como referencia para los análisis químicos de otros objetos astronómicos. Por último, también se emplean para obtener información sobre la formación y la evolución del sistema solar.

En particular, el estudio de la abundancia de oxígeno es crucial, debido a que es el metal más abundante en el Universo y juega un papel fundamental en la estructura del núcleo del Sol y otras estrellas. Además, es una fuente dominante de opacidad cerca de la base de la zona de convección solar y contribuye también a la opacidad del núcleo. En el desarrollo de esta tesis explicamos más detalladamente por qué la determinación de la abundancia de oxígeno es tan importante, así como resumimos brevemente las escalas de abundancias más usadas en astrofísica. También indicamos cómo se miden las abundancias y mostramos cuáles son los indicadores disponibles para determinar la abundancia fotosférica de oxígeno. Además, hacemos un resumen sobre los estudios que se han realizado para determinar la abundancia de oxígeno en el Sol, y en particular sobre los que se han realizado con la línea de oxígeno prohibida en 6300 Å, que es la línea espectral que usamos en esta tesis. También incluímos una sección sobre los modelos atmosféricos solares, ya que son un punto clave en las determinaciones de abundancias, así como para el entendimiento del Sol en general.

El objetivo del segundo capítulo es comparar los resultados de simulaciones de fáculas solares realizadas con los códigos `MURaM` y `STAGGER` . Primero comparamos las cantidades físicas computadas por los códigos y las confrontamos con resultados de inversiones obtenidas por Buehler et al. (2015) a partir de observaciones del Sol. Computamos el continuo en el visible y en el infrarrojo, y los parámetros de Stokes para el par de líneas espectrales de Fe I en la región de 6301-6302 Å. Comparamos los perfiles obtenidos a la resolución de la simulación y tras degradarlos a la resolución de SP/SOT en HINODE. Finalmente, determinamos la abundancia de oxígeno con las dos simulaciones.

En el tercer capítulo, queremos entender los límites de confianza de la abundancia de oxígeno fotosférico solar derivado a partir de modelos tridimensionales usando la línea de oxígeno prohibido en 6300 Å. Trabajamos con un modelo tridimensional empírico y dos atlas solares de intensidad. Además, empleamos inferencia Bayesiana como una herramienta para determinar el valor más probable para la abundancia de oxígeno solar dado el modelo elegido e incluyendo correlaciones con otros parámetros.

En el capítulo cuatro, realizamos una determinación de la abundancia de oxígeno solar utilizando observaciones resueltas espacialmente e inversiones. Invertimos observaciones de la VTT con el código NICOLE para obtener un modelo tridimensional empírico solar. Además, empleamos inferencia Bayesiana para obtener el valor más probable para la abundancia de oxígeno usando la línea de oxígeno prohibida en 6300 Å y teniendo en cuenta todos los parámetros del modelo.

Finalmente, en el último capítulo resumimos lo que hicimos en esta tesis y concluímos cuáles son los principales resultados obtenidos. Además, damos algunas indicaciones sobre cómo podríamos mejorar estos estudios en el futuro o qué nuevos estudios podrían realizarse.

Abstract

The study of the solar abundances dates back to the analysis of Russell of 1929. Since then, its become a very relevant topic in astrophysics. This is due to the fact that knowing the solar chemical composition is fundamental to build accurate models of the atmosphere and interior of the Sun and other stars. Furthermore, the present-time solar abundances are crucial to determine the composition of the Sun at birth, and to predict the past and future evolution and internal structure of our star. Besides, the solar abundances are used as a reference for the chemical analysis of other astronomical objects. Finally, they are also employed to obtain information about the formation and evolution of the solar system.

The study of the oxygen abundance, in particular, is especially relevant since it is the most abundant metal in the Universe, and it plays a fundamental role in the structure of the solar core and the cores of other stars. Moreover, it is a dominant source of opacity close to the base of the convection zone and it also contributes to the core opacity. In this thesis, we explain in detail why the determination of the solar oxygen abundance is so important, and summarize as well the abundance scales most used in astrophysics. We further indicate how the abundances are measured, discussing what are the spectroscopic indicators available to determine the photospheric abundance of oxygen. Furthermore, we provide an overview of the studies that have been made to determine the solar oxygen abundance and, in particular, about the studies based on the forbidden oxygen line at 6300 Å, which is the main transition employed in this thesis. We also include a section about atmospheric solar models, because they are a key tool for abundance determinations and for the understanding of the Sun in general.

The goal of the second chapter is to compare results of simulations of solar facular-like regions performed using the `MURaM` and `STAGGER` codes. We first interpolate the physical quantities computed by the codes to surfaces of constant optical depth. We then compare those quantities and confront them with inversion results obtained by Buehler et al. (2015) from real-Sun observations. We compute the continuum in the visible and infrared, and the full Stokes vector of the pair of Fe I spectral lines around 6301-6302 Å. We compare the computed profiles of the spectral lines (at the simulation resolution and after smearing them to the resolution of SP/SOT on board HINODE) in terms of the line-core intensity, equivalent width, and full-width at half-maximum for the Stokes I line profiles, as well as the area and amplitude asymmetry for the Stokes V

profiles. Finally, we determine the solar oxygen photospheric abundance with both simulations.

In the third chapter we aim at understanding the confidence limits of the photospheric solar oxygen abundance derived from three-dimensional models using the forbidden [O I] line at 6300 Å. We work with a three-dimensional empirical model and two solar intensity atlases. Bayesian inference is employed as a tool to determine the most probable value for the solar oxygen abundance given the model chosen, and including correlations with other parameters involved.

In the fourth chapter, we report the results of a determination of the solar oxygen abundance by using spatially-resolved observations and inversions. We invert observations from the Vacuum Tower Telescope with the NICOLE code to get a solar three dimensional empirical model. Moreover, we employ Bayesian inference to obtain the most probable value for the oxygen abundance, using the [O I] forbidden line at 6300 Å, and taking into consideration all the parameters of the model.

Finally, in the last chapter, we summarize the work and the conclusions. Moreover, we give some hints about what could be done in the future to improve this research.

Contents

1

Introduction

The Big Bang theory is the most accepted cosmological model to explain the origin and evolution of the Universe. This model describes how the observable Universe starts being extremely small and dense, and how it expanded and cooled being able to form atoms. There are three main sites for the formation of atomic nuclei: the first one occurred in the early Universe, the second one inside the stars and the last one in the interstellar medium. These processes through which new atomic nuclei are created from existing nucleons are called nucleosynthesis.

The Big Bang nucleosynthesis is the first phase of formation of atoms. It started about three minutes after the Big Bang and ended up leaving an Universe composition of approximately 75% hydrogen, 24% helium, and traces of lithium.

The second type of nucleosynthesis is the stellar nucleosynthesis, which occurs in the center of the stars and is responsable for the formation of all the elements from helium to iron and nickel through nuclear fusion. The stellar nucleosynthesis takes place because stars fuse different elements in their cores while they evolve. First, they burn hydrogen, then helium and progressively heavier elements.

The hydrogen fusion is made by two different processes, although the final result of both is to burn hydrogen to create helium. The first one is the proton-proton chain or pp chain, which is the dominant mechanism in stars with masses less or equal than those of the Sun. The chemical reactions that form the pp chain are shown in Fig. 1.1, where the percentages shown there correspond to the probability for each reaction in the solar case. The second process of hydrogen burning is the CNO cycle, which is the major mechanism in stars

more massive than the Sun. It is call CNO cycle because it uses nuclei of carbon, nitrogen and oxygen to finish creating helium. The main reactions involved in this cycle are represented in Fig. 1.2. These reactions constitute what is call the cold CNO cycle where the CNO-III and IV are important just for massive stars.

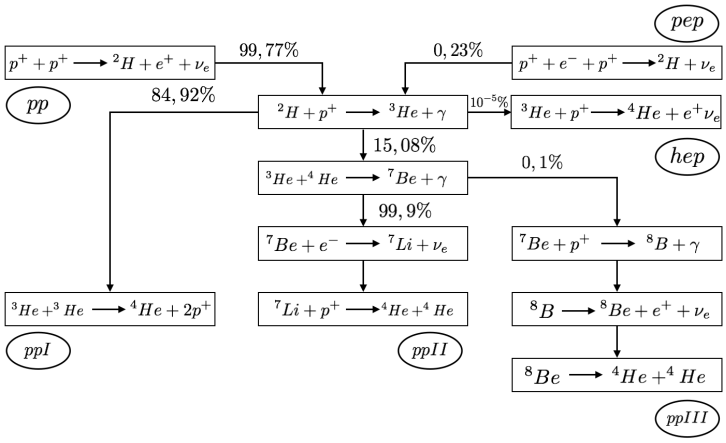

Figure 1.1: Nuclear reactions that takes place in the pp chain. The percentages shown in the figure are those for the Sun. This figure and Fig 1.2 are taken from the book Stasińska et al. (2012b).

The hydrogen fusion produces an accumulation of helium in the core of the stars. Thus, when the hydrogen in the core is consumed, it collapses until reaching a temperature high enough to start burning helium. The burning of helium is driven by the triple-alpha process, which increases the carbon concentration in the core. Moreover, when the carbon concentration is sufficiently high, the alpha process may take place forming oxygen, neon, and heavier elements up to nickel. This process is not able to produce heavier elements than nickel because these reactions are endothermic, require energy instead of releasing it. The reactions for helium burning are written below:

$$
\begin{aligned}
{}^4He + {}^4He &\rightarrow {}^8Be \\
{}^8Be + {}^4He &\rightarrow {}^{12}C + 2\gamma \\
{}^{12}C + {}^4He &\rightarrow {}^{16}O + \gamma
\end{aligned}
$$

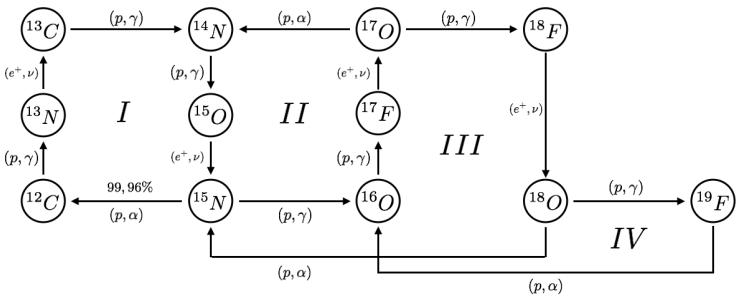

Figure 1.2: Nuclear reactions that take place in the cold CNO cycle. Here, the parenthesis notation is used, which means that the first element uses the first component of the parenthesis to form the other element and the second component of the parenthesis. For example, the first reaction of this cycle is $^{12}C + p^+ \rightarrow^{13} N + \gamma$.

$$^{16}O +^4 He \rightarrow^{20} Ne + \gamma$$
$$^{20}Ne +^4 He \rightarrow^{24} Mg + \gamma$$
$$^{24}Mg +^4 He \rightarrow^{28} Si + \gamma$$
$$^{28}Si +^4 He \rightarrow^{32} S + \gamma$$
$$^{32}S +^4 He \rightarrow^{36} Ar + \gamma$$
$$^{36}Ar +^4 He \rightarrow^{40} Ca + \gamma$$
$$^{40}Ca +^4 He \rightarrow^{44} Ti + \gamma$$
$$^{44}Ti +^4 He \rightarrow^{48} Cr + \gamma$$
$$^{48}Cr +^4 He \rightarrow^{52} Fe + \gamma$$
$$^{52}Fe +^4 He \rightarrow^{56} Ni + \gamma$$

The final stages in the lives of stars are different depending of their masses: a low mass star ends forming a planetary nebula after ejecting its envelope; while a massive star ends its life via a catastrophic event called supernova. The supernova nucleosynthesis is the last type of nucleosynthesis and it describes the creation of elements during the final stages of evolution and explosion of a massive star. This process forms the rest of the heavy elements in the Universe.

The research on what chemical elements exist in the Universe, and in which quantities, have multiple motivations. In particular, the composition of the solar system is investigated to understand how the diversity of planetary compositions can be explained. Moreover, the solar system composition is useful as a local Galactic composition standard. It is often assumed that the Sun and all other objects in the solar system are formed from a hot gaseous nebula with a well defined chemical composition. The solar system composition is quite similar to that found in most stars and interstellar material in our neighborhood (see the solar system composition in Fig 1.3). Furthermore, as the Sun corresponds to more than 99% of the solar system mass, it is, therefore, the major target for studying the solar system composition.

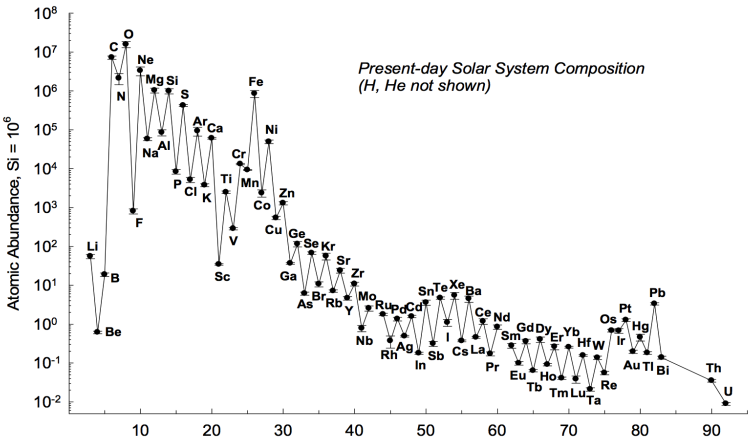

Figure 1.3: Solar system composition. Figure taken from Lodders (2010).

The Sun has been investigated since antiquity, looking by eye on a cloudy day, using smoked glasses or projection methods. In the seventeenth century, Galileo Galilei studied the Sun with his telescope and discovered that it was not a perfect sphere as previously thought, but on the contrary, it had dark spots that moved along its surface. Two centuries later, in 1802, William Hyde Wollaston discovered that the spectrum of the Sun was not continuous but was composed of dark lines called absorption lines. A few years later, in 1814, Joseph von Fraunhofer rediscovered the absorption lines and began a systematic study measuring their wavelengths. These absorption lines and their positions

indicated that the Sun contained elements known at that time, such as iron; but it also allowed discovering new chemical elements, such as helium. Thus, the solar spectrum could be used to determine what the Sun is made of.

The chemical composition of the solar photosphere was studied for the first time by Russell (1929). Since then, this topic has become very relevant in astrophysics, due to several reasons:

- the knowledge of the chemical composition of the Sun is fundamental to build detailed and accurate models of the solar atmosphere and interior,
- the solar composition is frequently used as a reference for the chemical analysis of other stars and astronomical objects,
- the current solar composition is crucial to infer the chemical composition of the initial Sun and to predict its future evolution, as well as its internal structure.
- Moreover, comparison of photospheric and meteoritic compositions provides us with information about the formation and evolution of the solar system.

In particular, the amount of oxygen present in the Sun is crucially important because it is the most abundant of all metals in the Universe, and the third element after hydrogen and helium (see Fig. 1.3). Due to that, oxygen is an important constituent of the clouds of gas and dust in space. Further, the amount of some specific elements, such as oxygen, carbon and nitrogen can affect the energy generation rates through the CNO cycle, which can change the structure of the core of the Sun and other stars. Moreover, oxygen is the dominant source of opacity in the region near the base of the solar convection zone, and it also contributes to the opacity in the solar core. Furthermore, some of the other important elements for interior models (especially Ne and Ar) cannot be directly measured (or only with much difficulty) and are typically measured relative to oxygen. Additionally, these elements also affect the equation of state.

1.1 Abundance scales

In astrophysics, the term abundance is used to indicate the amount in which a chemical element is present in an astronomical object, and there are several ways to express it. The astronomical scale is one of the most used abundance scales in astrophysics, and this is the scale that we use in this thesis. It makes reference to the ratio of the number density of the element, n_X (where X is the

chemical element of interest), with respect to hydrogen, n_H. It is a logarithmic scale in which the hydrogen value is set to 12 by convention. For a particular chemical element, for example oxygen, it is written as

$$A(O) = \log(\epsilon_O) = \log(n_O/n_H) + 12. \tag{1.1}$$

Another abundance scale widely used in solar physics is the meteoritic or cosmochemical scale. Meteorites have been used to determine the abundances of the solar system. More specifically, the type CI1 carbonaceous chondrites are commonly used because they are considered to be the best preserved samples of material available. Furthermore, the solar photosphere and meteoritical abundances exhibit very good agreement for most elements. The meteoritical scale gives the number of atoms relative to 10^6 atoms of Si:

$$N(E) = \frac{n(E)}{n(Si)} 10^6. \tag{1.2}$$

It is common to couple the previous scales to be able to compare studies made with photospheric abundances and with meteorites. To transform meteoritic to astronomical abundances we take into consideration that the difference of the logarithmic meteoritical abundances to the abundances in the astronomical scale is roughly constant for many elements (we note that some elements are volatiles and, therefore, they are depleted in meteorites). Thus we follow the next equation:

$$A(E) = R + \log[N(E)], \tag{1.3}$$

where the scale conversion constant is $R = 1.533 \pm 0.042$ using 40 elements (Lodders 2010). Previously, this value was larger, for example, Anders & Grevesse (1989) used only 12 elements and obtained $R = 1.554 \pm 0.020$. There is an agreement of 10% using these 40 elements, and the largest differences are found for the volatiles elements. However, in most cases the uncertainties of the determination of abundances, either meteoritic or photospheric, are larger than the difference in abundances, and the meteoritic and photospheric abundances agree within the errors.

Another way to determine abundances is by using the number of atoms per 10^6 atoms of H, measured in parts per million (ppm). This scale is easily transformed to the astronomical scale by applying the logarithm.

A further measure of abundances is the mass fraction. It is a useful form to express the composition because it allow us to define the metallicity as the summation of the mass fraction of all the elements heavier than helium. Usually, we represent the fraction of hydrogen as X, helium as Y and the metals

as Z, so that $X + Y + Z = 1$. Note that, in astronomy, all the elements except hydrogen and helium are called metals. In the oxygen example, its mass fraction would be expressed as follows

$$w(O) = \frac{\mu_O n_O / n_H}{\sum_E \mu_E n_E / n_H}, \tag{1.4}$$

where μ_E is the atomic weight of the element E and the summation in the denominator includes all the elements.

The bracket notation is normally used for cool stars, where the abundances are expressed in logarithm with respect to the solar value. Thus, for oxygen it would be

$$[O/H] = \log(n_O/n_H) - \log(n_O/n_H)_\odot. \tag{1.5}$$

This way to express abundances has the advantage that comparison is very easy, as it only consist of analyzing how much the composition of a start differs from solar. However, every time that the solar chemical composition is revised, it is mandatory to make a revision of all the previously published abundances determined in this manner. Moreover, recently, the solar chemical composition has being revised substantially. Thus, it is of crucial importance to have an accurate solar chemical composition to be able to trust not only the solar composition but also those for other stars and objects whose abundances are determined in this way.

1.2 Measuring solar abundances

As discussed above, the absorption lines in the solar spectrum may be used to determine the chemical composition of the Sun, since they give us information about the atoms and molecules responsible for their formation and the conditions where they originate. The absorption lines are formed when photons that come from a hot source (with a continuum spectrum) pass through a material that is cooler than the source (in the case of the Sun, its atmosphere) and are absorbed by the particles present there (see Fig. 1.4). The absorption is made at a specific wavelength that depends on the type of atom and molecule when the photon has an energy equal to the difference between two energy states of the particle. Therefore, absorption lines are the chemical fingerprint that tell us which elements (and in what amount) are contained in the source. Thus, using spectroscopy we can derive the solar chemical composition as well as the composition of other stars.

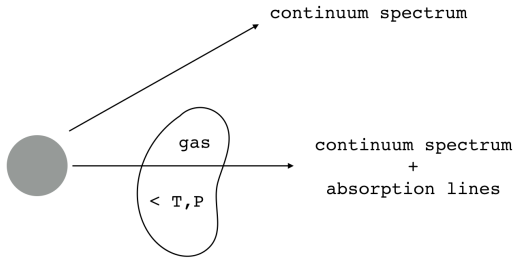

Figure 1.4: Ilustration of how an absorption line originates.

1.2.1 The radiative transfer equation

The explanation above implies that a beam of light that travels through a medium (in the direction s) experiences a change of intensity. This change is determined by the radiative transfer equation as follow:

$$\frac{dI_\nu}{ds} = -\alpha_\nu I_\nu + j_\nu; \tag{1.6}$$

where I_ν is the intensity, α_ν is the extinction coefficient and j_ν the emission coefficient for a given frequency (or wavelength).

It is useful to introduce the optical depth, τ_ν, which is a measure of the extinction coefficient up to a specific height, $d\tau_\nu = -\alpha_\nu dz$. In this equation, z is the vertical height or geometric depth, which is related to the direction s in this manner: $dz = \cos\theta ds = \mu ds$. A material with a high absorption coefficient will absorb lots of light in a small range of heights. However, a material with a lower absorption coefficient will need a more wide range of heights to absorb the same amount of light. This is the reason why the optical depth is a much more convenient depth scale. Moreover, if we define the source function as the ratio between the emission and the extinction coefficients, $S_\nu = j_\nu/\alpha_\nu$, the radiative transfer equation may be written as follow:

$$\frac{dI_\nu}{d\tau_\nu} = -I_\nu + S_\nu; \tag{1.7}$$

whose formal solution is

$$I_\nu(\tau_\nu) = I_\nu(0)e^{-\tau_\nu} + \int_0^{\tau_\nu} S_\nu(t_\nu)e^{-(\tau_\nu - t_\nu)}dt_\nu. \tag{1.8}$$

We can take into account the contributions of the continuum and the lines separately, so that the source function and the optical depth are respectively:

$$S_\nu^{tot} = \frac{j_\nu^c + j_\nu^l}{\alpha_\nu^c + \alpha_\nu^l} = \frac{S_\nu^c + S_\nu^l \eta_\nu}{1 + \eta_\nu} \tag{1.9}$$

and

$$d\tau_\nu^{total} = -(\alpha_\nu^c + \alpha_\nu^l)dz = (1 + \eta_\nu)d\tau_\nu^c, \tag{1.10}$$

where $\eta_\nu = \alpha_\nu^l / \alpha_\nu^c$ is the line to continuum ratio of extinction. Moreover, the extinction line coefficient is a variable that depends on the atomic parameters of the line, such as the gf factor; but also of the temperature of the media, the wavelength (or frequency), the number of free electrons, and the abundance of the element that form the line, i.e., $\alpha_\nu^l = f(gf, \nu, T, n_e, A)$.

1.2.2 Methods to measure solar abundances

Spectroscopy allows us to determine the photospheric abundances in two main ways: measuring the equivalent width of a spectral line, or using the line fitting method. The equivalent width of a spectral line is a measure of the line area and it is given by the equation

$$W_\lambda = \int_0^\infty \frac{I_c - I_\lambda}{I_c} d\lambda, \tag{1.11}$$

where I_c is the continuum intensity and I_λ is the intensity across the wavelength range. Its name is a consequence of the fact that it may be viewed as the width of a rectangle with the same area as the line. The equivalent width is a measure of the strength of a spectral line and, as the strength depends on the chemical composition, it may be used to calculate the abundance of elements by comparing the observed widths to those synthesized from a model atmosphere.

The line fitting method is the one that will be used in this work. It is based on fitting observed spectral lines with synthetic spectra (calculated with different abundance values). It follows the same idea that the equivalent width method. However, in this way we take into account the line strength and the line shape at the same time.

Otherwise, as explained above, meteorites are widely used to calculate the solar composition. Abundances for refractory elements can be determined very precisely from chondrites, having the advantage that the uncertainties are smaller than the photospheric determinations. However, volatiles elements, such as oxygen (the element studied in this thesis), are incompletely condensed in meteorites. Therefore, the photospheric determination is necessary to infer the abundances of such elements.

There are other less used methods that may be employed to obtain solar abundances. Particle detection techniques from space are used to measure the chemical composition of the solar wind (e.g., von Steiger & Zurbuchen 2016). Moreover, inversion of helioseismic observations allow us to derive the abundance of helium, which is not present in the photospheric spectrum and it is a volatile element that has been depleted in meteorites. Furthermore, from the Borexino experiment it is possible to obtain solar core abundances from solar neutrinos, in particular CNO neutrino fluxes (e.g., Haxton & Serenelli 2008).

1.3 Solar atmospheric models

1.3.1 Solar atmosphere

The solar atmosphere is defined as the outer region of the Sun, just above the surface where the optical depth at 500 nm reaches unity. It is traditionally divided in different layers, where different physical mechanism dominate.

The photosphere is the bottom of the atmosphere, just above the surface, where the temperature is around 6300 K. It reaches 500 km of height, where a minimum of temperature is found (T≈4400 K). The evolution of the solar plasma in this layer is dominated by convective motions, that creates convection cells called granules. These cells have a size of approximately 1000 km and a lifetime of around 10 minutes. They are bright plasma rising from lower layers due to the convective movements. After a while, the velocity becomes zero and the plasma goes down around the granules forming the intergranular lanes, which are smaller and darker structures than the granules (see Fig.1.5, which is taken from the NASA webpage[1]). Moreover, in the photosphere there are also pores and sunspots; which are dark spots on the surface of the solar disk. Sunspots appears dark compared to the granulation because they are colder than the granules and have a higher magnetic field. The magnetic field is strongest in the umbra, the darker part of the sunspot, and it becomes weaker in the penumbra, which is around the umbra. They can live for several weeks and are normally organized in groups with different magnetic polarity. Pores are like small sunspots with just a tiny umbra (see Fig.1.5, where a sunspot appears in the upper left corner of the figure and there are also several pores). The photosphere is our main source of information since most of the light that reaches us originates there. Further, most of the spectral lines available to measure abundances are formed in the photosphere. Thus, we focus our study

[1] See https://svs.gsfc.nasa.gov/3412

in this layer; but the solar atmosphere is composed also by the chromosphere, the transition region, and the corona.

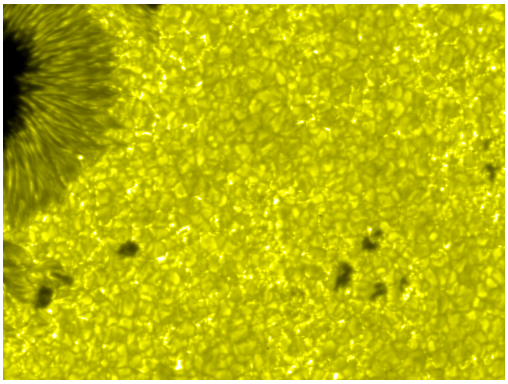

Figure 1.5: Image of a sunspot, pores and the granulation. This image is taken from the NASA webpage.

The chromosphere is the next solar layer and it has around 2.000 km of thickness and temperatures that vary from 4.400 to 20.000 K. This layer is dominated by the magnetic field, which is responsable for the formation of some of the features present in the chromosphere, such as spicules and filaments. The spicules are long thin structures that grow upwards from the photosphere in form of a field of grass. The filaments are also called prominences and are huge plumes of plasma supported by the magnetic field.

The solar transition region is a very thin layer that is defined because the temperature experiences a sharp increase. It is located between the chromosphere and the corona.

Finally, the corona is the outermost layer of the solar atmosphere and it extends several solar radii. The temperature in this region varies from around 30.000 K to $1.5{\cdot}10^6$ K. The solar corona is also dominated by the magnetic field.

1.3.2 Solar atmospheric models

To determine the chemical composition of the Sun, one needs to use models from which a synthetic spectrum is calculated and then compared to the observations. The model employed is then a fundamental ingredient of the

process, and the results are necessarily model-dependent. The first models made use of a simplified one-dimensional (1D) geometry. These models were static, in radiative, hydrostatic and local thermodynamic equilibria. Some examples of such 1D models are those of Kurucz (1979) or MARCS (Gustafsson et al. 1975). Modern reincarnations of these models have been described in Mészáros et al. (2012) and Gustafsson et al. (2008). These models are derived from theoretical principles, but some of the most successful 1D solar models were developed using a semi-empirical approach, namely, a model atmosphere where the temperature is deduced from observations by fitting many spectral lines and continua. Some of the most widely used semi-empirical models are the VAL models (Vernazza et al. 1976), HOLMU (Holweger & Mueller 1974), and HSRA (Gingerich et al. 1971).

In the last two decades much progress has been made in the theoretical modeling of the solar atmosphere, creating more realistic models where the simplification of 1D geometry and stationarity has been eliminated. These 3D models (like the ones discussed in Chapter 2) solve the equations for conservation of mass, momentum and energy, as well as the radiative transfer equation. They also use state-of-the-art equation of state (EoS) and opacities. Mainly, two family of models based on different computer codes and set of assumptions, have been used to carry out abundance determinations. The first family is built using the code developed by Nordlund & Stein (Stein & Nordlund 1998), later refined by Asplund and collaborators (Asplund et al. 2000b). The second one is based on CO^{5}BOLD (COnservative COde for the COmputation of COmpressible COnvection in a BOx of L Dimensions with L=2,3) developed by Freytag & Steffen (Freytag et al. 2002). These new 3D models have been checked by comparing them to observations in different test, with rather satisfactory results (e.g., Asplund 2000; Danilovic et al. 2008; Pereira et al. 2009a), giving confidence in their realism. Moreover, in three-dimensional models, concepts such as micro- and macroturbulence (necessary in 1D models) are no longer needed, since the average line profiles obtained by 3D theoretical models agree almost perfectly with the average observed profiles. On the other hand, a semi-empirical model may be able to capture better the mean thermal properties of the atmosphere and might be more adequate for abundance determinations. An attempt to resolve the issue was made by Socas-Navarro & Norton (2007) who employed spatially resolved observations of Fe I lines to derive a 3D semi-empirical model by inversion. They used an innovative approach, but the analysis was inconclusive due to instrumental problems and/or uncertainties in the non-LTE formation physics of the oxygen triplet lines that they observed.

1.4 The solar oxygen abundance in the photosphere

Oxygen plays a fundamental role in determining stellar and galaxy metallicities. In addition, because metallicity is a parameter in stellar models, the abundance of oxygen is important when it comes to creating stellar models that describe the structure and evolution of stars, and in particular the Sun. The current solar metallicity gives us an indication of how the star has evolved since its creation, and also comparing photospheric and meteoritic metallicities gives clues on how the solar system has evolved. Furthermore, it is difficult to determine absolute abundances in other stars. These are usually given in reference to their corresponding solar value. Thus, determining accurately the solar composition and, in particular, the amount of oxygen, is a crucial task.

The solar photospheric composition is not accurately known yet. Currently, a debate exits about the photospheric abundances and, in particular, the oxygen abundance. At the end of the 20th century, the accepted abundance set was the compilation by Anders & Grevesse (1989), in which oxygen abundance was $\log(\epsilon_O) = 8.93 \pm 0.04$ (in the astronomical scale). This value was based on the use of a one-dimensional semi empirical model and local thermodynamic equilibrium (LTE) line formation (Holweger & Mueller 1974) to fit spectral features produced by oxygen atoms and molecules. This value is similar to the $\log(\epsilon_O)$=8.92 previously found by Lambert (1978), but it was later revised downward to $\log(\epsilon_O) = 8.83 \pm 0.06$ in the work of Grevesse & Sauval (1998). With this abundance set, there is excellent agreement between solar interior models and the helioseismological predictions (see Basu & Antia (2008) and references inside). However, at the beggining of the 21st century, the solar spectrum was reanalyzed comparing it to calculations from three-dimensional hydrodynamical models, updated atomic line information and a treatment of departures from LTE leading to a lower solar metallicity (e.g. Allende Prieto et al. 2001; Asplund et al. 2004). For example, Asplund et al. (2004) determined $\log(\epsilon_O) = 8.66 \pm 0.05$. Such a low value spoils the previous agreement with helioseismology (see Basu & Antia 2008). On the other hand, this new low oxygen abundance helps with another problem, namely that the Sun is apparently oxygen-rich when compared with the local interstellar medium (e.g. Meyer et al. 1998; André et al. 2003). However, Ecuvillon et al. (2006) points out that planet-hosting stars exhibit a higher abundance, and the expected value should instead be 8.77.

The solar interior models, validated by the agreement between their predictions and helioseismological inversions, are based on the opacities computed with the solar chemical composition by Anders & Grevesse (1989), the high-Z composition. With the proposed downward revision (in particular the revision

of C, N, O and Ne), the solar metallicity in the photosphere decreases from Z = 0.0194 to Z = 0.0126. This produces a modification of the opacity because C, N, O and Ne are large contributors to the opacity in different layers below the convection zone. Therefore, the solar internal structure is altered, affecting the predicted sound speed profile. As a result, the agreement between sound speed variation with depth predicted by the models and inferred using helioseismology deteriorates considerably. The main reason for this discrepancy is the difference in the position of the base of the convection zone between the models and the Sun. Aditionally, solar models with low-Z composition have lower helium abundances than the Sun (Basu 2009). This discrepancy, often refereed to as the solar modeling problem, has stirred controversy in the community. Some authors consider it evidence that the low-Z composition is incorrect, others put the blame on the opacity data incorporated in the models (usually based on outdated calculations), while a third category is questioning the validity of the solar standard model itself.

Opacities affect the structure of the radiative zone and the convective envelope of the star. However, it is very difficult to make experimental determinations of opacities for solar conditions due to the combination of high temperatures and densities. Most data come from theoretical calculations of transition probabilities. In the context of the solar abundance problem, Christensen-Dalsgaard et al. (2009) have shown a degeneracy between solar composition and opacities. In fact, the solar problem could be resolved if the mean opacity for the solar interior were approximately 15-20% higher than previously thought because the increased opacity compensates for the decreased abundances (Bailey et al. 2015). There are two sets of opacities widely used in solar calculations, OPAL (Iglesias & Rogers 1996) and OP (Badnell et al. 2005). Badnell et al. (2005) found that the differences in the Rosseland mean opacities between OPAL and OP are up to 3%, much smaller than needed for compensating changes in solar abundances. More recently, a new set of opacities has been produced (Blancard et al. 2012). A comparison with OP shows large differences that can reach 40%; however, when the Rosseland mean is compared, it agrees with OPAL and OP within 4%. Therefore, the upward revisions in interior opacities needed to accommodate the new low oxygen abundance are larger than permitted by uncertainties (Antia & Basu 2006). On the other hand, laboratory measurements of iron yielded values much higher than expected (Bailey et al. 2015), which also creates uncertainty about the existing opacities.

Moreover, the latest generation of three-dimensional solar convection models have become rather realistic. This is an important advance in the modeling and understanding of the structure of the solar photosphere. Therefore, if the

revised solar oxygen abundance is correct, this would imply that the standard solar structure model may be missing, or have a inadequate treatment of important physical processes.

The solar abundance problem has also motivated further work on the improvement of nuclear reaction rates, theoretical and experimental work on radiative opacities, and on the equation of state appropriate for solar conditions. On the side of photospheric abundance determinations, the situation has induced a re-analysis of photospheric models, resulting in support for high (e.g. Ayres et al. 2006; Centeno & Socas-Navarro 2008; Ayres 2008), low (e.g. Scott et al. 2006; Socas-Navarro & Norton 2007; Meléndez & Asplund 2008; Pereira et al. 2009a; Grevesse et al. 2010), and intermediate (e.g. Caffau et al. 2008, 2011) solar oxygen abundances. The differences in the abundances originate in the calculations of line formation, the choice of atomic data and/or the selection of lines used in the analysis, as well as practical details of the analysis such as the selection of continuum level or the wavelength scale. On this side, Socas-Navarro (2015) showed that minor variations of these parameters could change the abundance values up to 0.2 dex.

1.5 Indicators of photospheric oxygen abundance in the Sun

The solar photospheric oxygen abundance is extremely difficult to measure because there are very few atomic oxygen lines available in the solar spectrum, and most of them are either very weak and/or blended or exhibit departures from local thermodynamical equilibrium. The most commonly used abundance indicators in the Sun are the forbidden [O I] line at 6300 Å, the infrared triplet around 7774 Å, and molecular bands of OH and CO. In addition to those, we also find other forbidden lines at 5577 and 6363 Å, and two more triplets around 6150 and 9270 Å.

Forbidden lines are formed in LTE in the photosphere because collisions dominate their pumping. For this reason these lines are very popular. However, the three lines are very weak and blended. The line at 6300 Å has a Ni I blend, the line at 6363 Å is blended with two CN lines and the line at 5577 Å is blended with two C_2 lines.

The triplet of atomic lines at 7774 Å is affected by non-LTE effects (e.g., Kiselman 1991) and some degree of uncertainty remains with respect to its formation physics, particularly collisional rates. However, despite this, it is a widely used indicator. In particular, Asplund et al. (2004) analyzed OH, O I and [O I] lines with a detailed oxygen atom model and taking non-LTE effects into account. They found good agreement among the different indicators. On the other hand, the other two triplets, at around 6150 and 9270 Å, are seldom

used in the literature because they are strongly blended with telluric lines.

The molecular OH lines that have been used in the literature are pure rotation lines and vibration-rotation transitions and have been studied by e.g. Asplund & García Pérez (2001); Asplund et al. (2004, 2009). Similarly, the CO lines may be used to derive combined carbon and oxygen abundances, in particular from the fundamental and first overtone bands of ro-vibrational lines (e.g. Ayres et al. 2006; Scott et al. 2006).

In this thesis, we used the forbidden [O I] line at 6300 Å with the Ni I blend to derive the solar photospheric oxygen abundance. We chose this line because it is a well known feature, and we are able to compare our results with those in the literature. Moreover, its atomic parameters are probably rather well known. Finally, this spectral line is very close to the two popular photospheric Fe I lines at 6301.5 and 6302.5 Å. We take advantage of these nearby lines to produce local empirical model atmospheres with which we derive the oxygen abundances.

1.6 Oxygen abundance from the [O I] forbidden line at 6300 Å

The oxygen atomic forbidden lines, and in particular the relatively strong [O I] 6300 Å line, are considered good indicators of the oxygen abundance, given they are formed in LTE conditions. However, this line has a blend with Ni I (originally noted by Lambert 1968) which plays a pivotal role in this feature. Without taking into account the Ni I line, the predicted [O I] line has the wrong central wavelength and a line shape that differs from the observed one. Nevertheless, for a long time, it was assumed that the Ni I line was unimportant, leading to a much larger derived solar oxygen abundance. Here, we briefly summarize some results that have been obtained with this line, since it is the one that we used in our work. It is clear that the derived oxygen and nickel abundances using this feature are related: any increase in the oxygen abundances implies a decrease in the nickel abundance and viceversa. This situation is summarized in Fig. 1.6, where some previous results of abundances using this features are shown. This figure present the relative abundances of oxygen and nickel that have been obtained in the literature. The squares represent the values obtained in this thesis, where CAS1, CAS2 and CAS3 are the results obtained in the Chapter 2, Chapter 3 and Chapter 4 respectively.

Allende Prieto et al. (2001) analyzed this line using a three-dimensional time-dependent hydrodynamical model, and they obtained an oxygen abundance of $\log(\epsilon_O)$=8.69±0.05. They attribute this value mainly to the model used and the consideration of the Ni I line, because they treat the product $gf\epsilon(Ni)$ as a free parameter. Similarly, Asplund et al. (2004) obtained

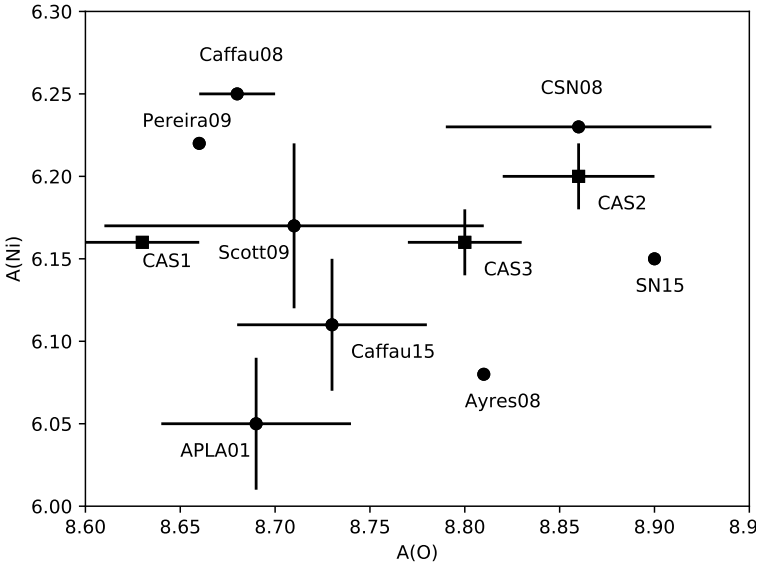

Figure 1.6: Oxygen and nickel abundances derived in the literature.

$\log(\epsilon_O) = 8.69 \pm 0.05$ using the same 3D hydrodynamical model.

Later, Caffau et al. (2008) used a CO^{5}BOLD 3D solar model atmosphere to obtain the oxygen abundance. They adopted the nickel abundance of Grevesse & Sauval (1998), $\log(\epsilon_{Ni})$=6.25, and considered it as a fixed parameter obtaining $\log(\epsilon_O)$=8.68±0.15. They claimed that their main error sources were: the $\log(gf)$ value, the broadening theory, blending error and the statistical error. They proposed a possible approach using a multi-parameter fit, with oxygen and nickel abundances, wavelength shift, and continuum level as free parameters. They considered the wavelength shift because the convective line shifts predicted by their simulations had an accuracy of the order of 50 m/s. Moreover, they noted that the wavelength shift and the nickel abundance will be correlated parameters, producing degenerate solutions for the best fit.

Moreover, Ayres (2008) used a 3D convection snapshot from CO^{5}BOLD and found a value about 650 ppm (or $\log\epsilon_O$=8.81 dex). Furthermore, Cen-

teno & Socas-Navarro (2008) used the asymmetry of the Stokes V profile[2] as an indicator of the relative abundances of the two elements (oxygen and nickel). Their goal was to observe a sunspot umbra, because the different Zeeman splittings of the lines would allow them to differentiate the lines in the polarized spectrum. They obtained $\log\epsilon_O$=8.86±0.07, later correct by Scott et al. (2009), who indicated that the abundance obtained by Centeno & Socas-Navarro (2008) should be revised downward to $\log\epsilon_O$=8.71±0.10. They made this correction taking into account that the gf value taken by Centeno & Socas-Navarro (2008) was outdated, using also the new nickel abundance that they obtained ($\log\epsilon_{Ni}$=6.17±0.07), adopting the carbon abundance of Asplund et al. (2005), and fully propagating all errors. Similarly, Pereira et al. (2009b) made a detailed treatment of the line including the nickel abundance of Asplund et al. (2009), $\log\epsilon_{Ni}$=6.22, obtaining an oxygen abundance of $\log\epsilon_O$=8.66.

More recently, Caffau et al. (2015) analyzed intensity spectra observed at different limb angles in comparison with a CO^{5}BOLD 3D hydrodynamical simulation of the solar atmosphere. They used a slightly lower nickel abundance ($\log\epsilon_{Ni} \approx 6.1$) from the commonly adopted value of $\log\epsilon_{Ni}$=6.25, and they obtained consistent fits indicating an oxygen abundance of $\log\epsilon_O = 8.73\pm0.05$. This reduction of the nickel abundance could be excessive, since the meteoritic nickel abundance recommends a value of $\log\epsilon_{Ni} = 6.22\pm0.03$ (Lodders 2003). Finally, Socas-Navarro (2015) made a new determination using an observational 3D model obtaining $\log\epsilon_O = 8.90$ using $\log\epsilon_{Ni} = 6.15$. Nevertheless, they concluded that it is possible to obtain up to $\log\epsilon_O = 8.70$, a 0.2 dex lower oxygen abundance, by small perturbations in the temperature of the model, or changes in the atomic parameters of the lines, the wavelength calibration, or the continuum reference.

1.7 Outline and motivation

Nowadays, three dimensional theoretical models agree quite well with solar observations. However, several simulation codes are available which embrace different physical approximations. Moreover, the spatial resolution of these simulations is usually higher than that of the observations, and different codes and snapshots tend to have different pixel sizes. Further, to our knowledge there is only one study comparing the results of different simulation codes (Beeck et al. 2012). Because of that, in Chapter 2, we perform a study extending the

[2]The Stokes parameters describe the polarization state of the light. There are four parameters: the intensity, I, which represent the unpolarized light; the parameters Q and U, which express the light polarized lineally; and the Stokes V, which correspond to the circularly polarized light.

work of Beeck et al. (2012) by comparing snapshots from MURaM and STAGGER 3D MHD simulations. Both simulations are carried out with a mean magnetic field of around 200 G (instead of the HD case of Beeck et al.) and we push for having as similar setups as possible. However, we use each code with its usual choice of free parameters. By doing that, we are able to compare the results of different simulation codes and check the realism of the simulations and the internal consistency of the codes. Moreover, we want to see the effect of the magnetic field and the influence of these factors in the abundance determinations. This is very important as some of the recent set of solar abundances are determined using a three dimensional theoretical HD model (e.g. Ayres 2008; Asplund et al. 2009; Caffau et al. 2015).

In Chapter 3, our objective is to better understand the confidence limits of the photospheric solar oxygen abundance derived from three-dimensional models. We work with a three dimensional empirical model and consider a number of error sources, such as uncertainties in the continuum derivation or in the wavelength calibration. This is a much needed task because of the many parameters involved in abundance determination. It is crucial to consider all of them to obtain reliable abundances.

In Chapter 4, we carry out a similar study; but with the novelty of using spatially resolved observations to create the solar three dimensional empirical model. This allows us to compare the synthetic profiles in each pixel of the model with the corresponding pixel in the observational map, having complete coherence instead of comparing with an observational atlas as in Chapter 3. Thus, we fit each individual profile, observed at each pixel using the same instrument and configuration as that used to derive the atmosphere, obtaining therefore an oxygen abundance value for each point. In other words, we take advantage of the uniqueness of the Sun, the only star that can be observed with high spatial resolution. We use different spatial locations, including granules and intergranular lanes, spanning a temperature range of nearly 1000 K in the photosphere.

Finally, in Chapter 5, we give some conclusions of the work performed in this thesis and some future analysis that may be execute to improve our knowledge about the solar photospheric abundances.

2

Comparison between MURaM and STAGGER simulations of solar faculae

2.1 Introduction

The strongest (kilo-Gauss) magnetic fields in the solar photosphere are organized in structures that vary significantly in size, brightness and total magnetic flux forming hierarchy of observed solar magnetic patterns (Zwaan 1978). The small magnetic structures are typically bright in the continuum images, while the larger ones appear dark. The small structures are always present in the Sun (irrespectively of the solar cycle phase) and are typically situated in between the convective granules (see de Wijn et al. 2009). In the quiet Sun they appear as individual magnetic elements, while in active regions they are arranged into chains, crinkles, or small clusters named *filigree* by Dunn & Zirker (1973). In active regions, their collective appearance is known as solar faculae when seen in the photospheric diagnostics, and as solar plage when seen in the cores of the strong chromospheric lines.

The knowledge about the solar photosphere and its magnetic structure and evolution has dramatically advanced by the combined use of three-dimensional (3D) numerical magnetohydrodynamic (MHD) simulations (see extensive reviews by Nordlund et al. 2009 and Stein 2012), and high-resolution observations. Starting from the pioneering work of Nordlund (1982), numerical simulations of the near-surface convection experienced rapid development in the last decades, in terms of the complexity of the physics included in the simulations (see e.g., Vögler 2003; Vögler et al. 2005; Stein & Nordlund 1998). In these and similar (magneto-)convection simulations, a complex set of non-local

physical equations (the Navier-Stokes equations of fluid dynamics, Maxwell's equations, the equation of state, and the radiative transfer equation) are numerically solved on a geometrical grid by using physically meaningful boundary conditions and very few free parameters (e.g., effective temperature, gravity, metallicity).

The results of the simulations of various solar magnetoconvection regimes are confronted with observations in various diagnostics and typically very good agreement is found. Some impressive examples of a good match between quiet-Sun simulations and observations are those of the shapes of photospheric spectral lines (e.g. Asplund et al. 2000a), of the quiet-Sun granular root-mean-square (RMS) contrast (e.g. Danilovic et al. 2008), and of the center-to-limb variation of the continuum intensity (e.g. Pereira et al. 2009b).

Three-dimensional numerical simulations designed to study faculae/plage are commonly initiated with vertical unipolar hecto-Gauss magnetic fields, providing a magnetic flux similar to that found in the active regions out of sunspots (Bercik 2002; Bercik et al. 2003; Vögler 2003; Vögler et al. 2005). Keller et al. (2004) and Carlsson et al. (2004) used snapshots from this type of simulations to explain and reproduce the appearance of bright granulation walls and faculae in observations toward the solar limb.

However, it should also be kept in mind that the good match between the synthetic observations produced from the numerical simulations of the photosphere and the actual solar observations does not guarantee that the simulations fully replicate processes in the real Sun, for two main reasons. First, the radiative diagnostics are naturally insensitive to the subphotospheric layers, which can be probed only by indirect observations, e. g. via local helioseismology (Gizon & Birch 2005). Therefore, the match between simulations and observations in the radiative diagnostics does not necessarily mean that there is a match below the photosphere. Secondly, the spatial resolution of the simulations is usually significantly higher than that of the available observations. The comparison between the two is performed after the synthetic observations (and, eventually, the corresponding spectra) are degraded to the resolution of the observations, smearing out any possible fine differences between the model and the observation. For this reason, the realism of the simulations can be said to safely hold validity at a resolution no higher than that of the observations that they are able to match.

Beeck et al. (2012) performed an important cross-validation of the results of hydrodynamical simulations of the solar convection obtained with three different R(M)HD codes: CO^{5}BOLD (Freytag et al. 2002; Wedemeyer et al. 2004), MURaM (Vögler 2003; Vögler et al. 2005) and STAGGER (Nordlund 1982; Stein & Nordlund 1998). They compared the vertical stratification of several variables

computed by the codes as well as the centre-to-limb variation of the continuum intensity at various wavelengths synthezised on the basis of the snapshots. Despite the different simulation setups used to obtain each of their datasets, they found that the results for the different codes agree quite well in the variables they studied. Their results are encouraging in terms of being able to apply the simulation snapshots. They also give additional confidence in the reliability of the numerical simulations themselves. However, Beeck et al. (2012) focused only on hydrodynamical simulations.

Including magnetic fields adds complexity to the problem. Observational evidence shows that magnetism is an essential part of solar phenomena (Trujillo Bueno et al. 2004), and recent theoretical work shows that solar convection is inherently magnetized (Khomenko et al. 2017). When comparing non-magnetic and magnetic simulations, considerable differences have been found in the flow structure in layers up to the temperature minimum (Moll et al. 2012). Thus, especially for studies requiring highly realistic model atmospheres (e.g., in relation to the accurate determination of the solar chemical composition, or to solar irradiance and its variability), accounting for the effects of solar magnetic fields is a necessary step. For example, Fabbian et al. (2010) for the first time showed that direct (magnetic) and indirect (thermal) effects in 3D MHD simulations significantly impact the derived solar composition. In the context of solar irradiance studies, faculae are believed to give the major contribution to solar variations on timescales of solar rotation. The result of 3D MHD solar simulations do suggest that photospheric magnetic fields, depending on their spatial distribution and on the wavelength considered, can affect the solar continuum intensity and flux (Vögler 2005; Fabbian et al. 2012; Danilovic et al. 2013; Criscuoli & Uitenbroek 2014a; Fabbian & Moreno-Insertis 2015). Along with the inclusion of atomic and molecular spectral lines, a more comprehensive description based on 3D MHD photospheric simulations, should thus further improve the understanding of solar irradiance variations on different time scales (and, thus, of solar irradiance reconstruction models), and in fact also of the variable magnetic activity of solar-type stars (see e.g. the review by Fabbian et al. 2017).

In the work presented in this chapter, we aim to extend the study by Beeck et al. (2012) by comparing snapshots from `MURaM` and `STAGGER` 3D MHD simulations with a mean magnetic field of the order of 200 G, i.e. representing a solar plage. The setups of the two simulation runs selected for comparison are more similar to each other than those selected by Beeck et al., but they still differ considerably. Although it would also be interesting to study setups as close as possible (for example the same equation of state, opacities, and boundary conditions are adopted), such comparison would address more the numerical

side of the two codes, and their particular algorithms and implementations, whereas our aim is to study how consistent the simulations are and therefore, the results derived from them obtained by different groups. In particular, we want to carry out a deep study of the simulations used to check their realism and the consistency of the codes, to determine the influence that these factors may have in the abundance determinations. Therefore, we opt to use each of the codes with its own usual choice of free parameters and supplemental data. The MURaM simulation run is described in Vögler et al. (2005) and it has been extensively used and extended by Keller et al. (2004), Shelyag et al. (2007), Vitas et al. (2009), Afram et al. (2011), Danilovic et al. (2013), Riethmüller & Solanki (2017), and others. The STAGGER run is described and used in Fabbian et al. (2010), Fabbian et al. (2012), Fabbian & Moreno-Insertis (2015) (see also Carlsson et al. 2004 for a description of the setup) and has also been employed in Beck et al. (2013), Criscuoli (2013), Criscuoli & Uitenbroek (2014a), Criscuoli & Uitenbroek (2014b), and Beck et al. (2017).

In Section 2.2, we briefly introduce the two codes and the one used for line synthesis. The details of the simulation setup and the line synthesis are specified in Section 2.3. In Sect. 2.4 we compare the quantities computed with the two codes to each other and versus the inversion results of Buehler et al. (2015). The synthetic spectra computed from the two codes are compared and discussed in Sect. 2.5. We compare the radiative diagnostics averaged over the horizontal extent of the snapshots, then the spatially resolved diagnostics at the simulation resolution, and finally the diagnostics after they have been smeared to mimic observations at a real telescope. Finally, in Sect. 2.6, we make a determination of the oxygen abundance using a MURaM snapshot and the [O I] line at 6300 Å.

2.2 Tools

In the following subsections, we briefly introduce the tools used in this work: namely, the numerical 3D MHD simulation codes MURaM (Vögler 2003; Vögler et al. 2005) and STAGGER (Galsgaard & Nordlund 1996); the spectral synthesis code NICOLE (Socas-Navarro et al. 2015); and the procedure for spectral and spatial degradation, in terms of resolution, of the line profiles computed from the snapshots produced by the two codes, to the resolution of the spectropolarimeter (SP) of the solar optical telescope (SOT) on board the Hinode satellite (Kosugi et al. 2007a; Tsuneta et al. 2008; Lites et al. 2001a).

2.2.1 MURaM

The **M**PS/**U**niversity of Chicago **Ra**diation **M**agneto-hydrodynamics (MURaM) code was developed to study the interaction between convective fluxes and magnetic fields in the solar photosphere. The version of the code we use here is the "old" one described in Vögler (2003) and Vögler et al. (2005), not to be confused with a more modern version with numerous upgrades and additional features necessary for large-domain simulations (see Rempel et al. 2009; Rempel 2014, 2017). Still, the two versions share the basic principles and there is no reason to expect that significantly different results would be found in the experiment we present here if the new version of the code were to be employed with a similar simulation setup as we adopt. MURaM uses a 4th-order central difference spatial scheme and a 4th-order Runge-Kutta temporal scheme. As described in Vögler (2003) and Shelyag (2004), the code employs a realistic EoS to compute temperature and pressure (needed for computing the radiative energy exchange) in terms of density and internal energy density, which are native thermodynamical quantities in the code. The EoS takes into account the effects of partial ionisation. The Anders & Grevesse (1989) solar chemical mixture was adopted (both in the EoS and for the subsequent derivation of opacities). An open boundary condition was applied at the bottom of the simulation box with an algorithm implemented to control fluctuations of the total mass in the box and of the mean radiative output (see detailed description in Vögler 2003). The simulation used in this study was carried with the top boundary closed for the mass flow and with a vertical magnetic field. The radiative transfer equation in MURaM is solved assuming local thermodynamical equilibrium and using a short-characteristics formal solver (Olson & Kunasz 1987, Kunasz & Olson 1988) with 24 rays (3 per octant). The horizontal boundary condition is periodic for all the quantities. Local interpolation of the opacity is done with a bilinear formula. The approximation of the quantities along the line of sight is linear. Opacity distribution functions (ODFs) used for the opacity binning (Nordlund 1982) are computed using the ATLAS9 code (Kurucz 1993). The main features of the MURaM version used here are shown in Table 2.1.

2.2.2 STAGGER

The 3D radiative-magnetohydrodynamics Copenhagen STAGGER code was originally developed by Nordlund (1982)[1]. The code is MPI-parallelised. To solve the equations for the conservation of mass, momentum and energy, it employs

[1]For further details, see e.g. Galsgaard & Nordlund (1996), and Beeck et al. (2012).

Property	MURaM	STAGGER
Spatial scheme	4th-order central difference	6th-order finite difference
Temporal scheme	4th-order Runge-Kutta	3rd-order Runge-Kutta
RT solver	LTE short-characteristics	LTE long-characteristics
Equation of state	ideal with partial ionization	non-ideal
Opacities	ATLAS 9	Uppsala/MARCS
Opacity bins	4	4
Number of rays	12	9 (8 inclined + vertical)

Table 2.1: Main features of the MURaM and STAGGER simulation codes.

a 6th-order finite-difference Cartesian scheme in space with 5th-order interpolations and a 3rd-order Runge-Kutta scheme for time-stepping of the magnetohydrodynamic variables.

The EoS follows Mihalas et al. (1988) and accounts for the effects of excitation, ionization, and dissociation of the most abundant chemical elements in the solar photosphere. Their solar abundances, needed in the EoS and also for the computation of opacities, is taken from the set used in Table 1 of Gustafsson et al. (1975).

Opacities due to continuum (Gustafsson et al. 1975, and subsequent updates) and to spectral lines (Gustafsson et al. 2008, and subsequent updates) come from the Uppsala/MARCS opacity package. Given the dependence of the opacity on wavelength, a large set of wavelength points has to be used to obtain accurate data to be used as input for the opacity sampling (OS) technique employed by the code. Then, when solving the radiative transfer equation according to a Feautrier-like scheme (Feautrier 1964) along eight inclined rays (two inclination angles, four azimuth angles) plus the vertical, the code uses the opacity binning method of Nordlund (1982) to group the OS data into only a few opacity bins, with the assumption of LTE adopted throughout these calculations. The snapshots used here employed 4 opacity bins, as done in the MURaM run.

The code uses open boundary conditions vertically, both at the bottom and at the top of the simulation box. The inflow of entropy at the bottom boundary controls the radiative output in the simulation and is set as initial input by the user. At the top boundary, potential electric field extrapolation guides the magnetic field configuration. Horizontally-periodic boundary conditions are imposed for all variables on the sides of the simulation box. The main features of the STAGGER version employed to obtain the snapshots used here are shown in Table 2.1.

2.2.3 NICOLE

NICOLE (Non–LTE Inversion COde using the Lorien Engine, Socas-Navarro et al. 2015) is a forward synthesis and inversion code to compute the Stokes profiles emerging from solar and stellar atmospheres. In this work we use only the forward module of the code to compute the two Fe I spectral lines at 6301 and 6302 Å at the disk center assuming LTE.

The code can synthesize the spectra from 2- and 3-dimensional atmospheres, but the radiative transfer equation is solved only in the vertical direction (1.5D approach). Numerical formulas to calculate collision rates were adapted from MULTI (Scharmer & Carlsson 1985) to facilitate the transfer of atomic models and data.

The input atmosphere has to contain at least the temperature and another thermodynamical quantity (density, pressure or electron pressure), the magnetic field vector and the line-of-sight bulk velocity. NICOLE does not account the polarization produced by scattering processes or modified by the Hanle effect. It only takes into account the polarization induced by the Zeeman effect. Several opacity packages and equations of state are implemented in the code. We use the opacity package and EoS of Wittmann (1974). Finally, the abundances set used is the one from Grevesse & Sauval (1998).

2.3 MHD simulations and synthetic spectra

2.3.1 Simulation setup

We used 25 snapshots computed by each of the two MHD codes. The two chosen datasets are representative of typically-used setups for each of the two codes, therefore making them a good choice for the comparison we propose here, and useful to corroborate the results of previous works applying these codes and using similar setups.

The STAGGER snapshots were chosen as a subset of the simulation of Fabbian et al. (2010), so as to cover a total of 36 solar minutes at regular intervals of 1.5 solar minutes. In the case of the STAGGER simulation run, a uniform vertical magnetic field of ~ 225 G was introduced into an already evolved HD simulation. The MURaM simulation run was re-initiated from a plage snapshot (saved from a run that was originally initiated with the unipolar vertical magnetic field of 200 G, Vitas et al. 2009) and the snapshots were saved at the same time interval as in the STAGGER case.

Each simulation covers an area of ~ 6.0 x 6.0 Mm^2 horizontally (i. e., ~ 15 granules). Vertically, the STAGGER snapshots reach from ~ 0.5 Mm above the

height corresponding to the level of optical depth unity (τ_{5000}=1, where τ_{5000} is the continuum optical depth at a wavelength of 5000 Å) down to $\sim$ 2.0 Mm below it. The MURaM snapshots have a vertical domain of $\sim$ 1.4 Mm, reaching $\sim$ 0.5 Mm above $\tau_{5000} = 1$. An illustration of the geometry of the simulations is given in Fig2.1, where a temperature cube is show for a CO^{5}BOLD simulation[2].

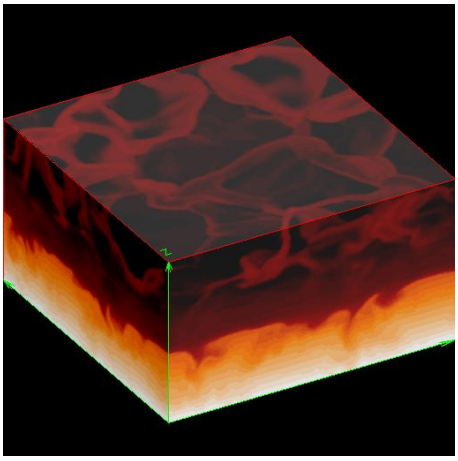

Figure 2.1: Illustration of the geometry of the simulations. The cube represent the temperature of a CO^{5}BOLD simulation, for STAGGER and MURaM the result is similar.

The original STAGGER snapshots have 252 grid points (giving a uniform horizontal grid spacing of $\sim$ 24 km) in each of the two horizontal directions, and 126 non-uniformly distributed grid points vertically (with a maximum resolution in height of $\lessapprox$ 15 km at the photosphere). The MURaM snapshots have 288 grid points uniformly distributed in each horizontal direction (20.8 km per cell) and 100 grid points uniformly distributed in the vertical direction (14 km per cell).

2.3.2 Spectral synthesis

The output snapshots from the MHD simulations contain the mass density of the plasma, the linear momentum vector, the total energy density (for MURaM,

[2]The picture is taken from the PhD thesis of Sven Wedemeyer. See https://folk.uio.no/svenwe/research/phd/images/chro3D02b1_Tcube.jpg

Table 2.2: Atomic parameters (central wavelength, lower level excitation potential, oscillator strength and effective Landé factor) of the spectral lines considered in this study.

λ_0 [Å]	χ_e [eV]	$\log(gf)$	$g_L^{\rm eff}$
6301.501	3.654	-0.718	1.67
6302.494	3.686	-1.13	2.49

while for STAGGER the internal energy density is saved), and the magnetic field vector. Each of these quantities is given for every vertical grid point along the common (i.e. being the same for every pixel) geometrical height scale. The quantities are interpolated to a common optical depth scale at 5000 Å and prepared in the file format required by NICOLE.

NICOLE is then employed to synthesize the two Fe I spectral lines at 6301 and 6302 Å. The atomic data needed for the synthesis (the central wavelength λ_0, the excitation potentials of the lower level χ_e, the weighted logarithmic oscillator strengths $\log(gf)$ and the effective Landé factor[3] g_L^{eff}) for the two lines are listed in Table 2.2. The value we adopted for the iron abundance is $\log(\mathrm{Fe}_\odot)$=7.50 dex (Asplund et al. 2009).

2.3.3 Data degradation

To be able to compare the computed line profiles to the profiles observed with the SOT onboard Hinode (Tsuneta et al. 2008) we convolved the computed intensities with a point spread function (PSF, see e.g., Nordlund 1984). We applied the ideal part of the PSF of SOT provided by Wedemeyer-Böhm (2008) and scaled to 6300 Å. The ideal part of the PSF accounts only for the geometry of the telescope, the size, the spider, etc.; and it widens with wavelength, being narrower in the blue and wider in the red (giving us more resolution in the former and less in the latter). Moreover, Hinode has three broad-band channels at three wavelength intervals. In each of the three channels actual observations are used to model the realistic PSF that includes the entire optical path with all imperfections. Thus, we took the ideal part for and scaled it linearly to the wavelength of 6300 Å. Then, we re-gridded the smeared profiles to mimic the pixel size of the SP/SOT detector (Lites et al. 2001a). Finally, we convolved each of the profiles with the instrumental profile of the spectrograph, and interpolated the convolved profiles to the wavelength sampling of the instrument. The entire procedure is described in detail in Vitas (2011).

[3]The effective Landé factor is taken from the VALD3 database, http://vald.astro.univie.ac.at/∼vald3/php/vald.php

2.4 Results: *Simulated atmosphere*

2.4.1 Mean vertical stratifications

As the first measure of similarity between the two simulation runs, we checked the average stratification of the quantities computed by the two codes. We performed the averaging over constant vertical τ_{5000} surfaces. In Fig. 2.2 we show the mean (iso-τ_{5000}) vertical stratification of the temperature, total magnetic field strength, inclination angle of the magnetic field and vertical velocity. The red curve corresponds to the MURaM results, the blue one to the STAGGER ones. Throughout this work, we use the same choice of colors to show the various results of the two codes.

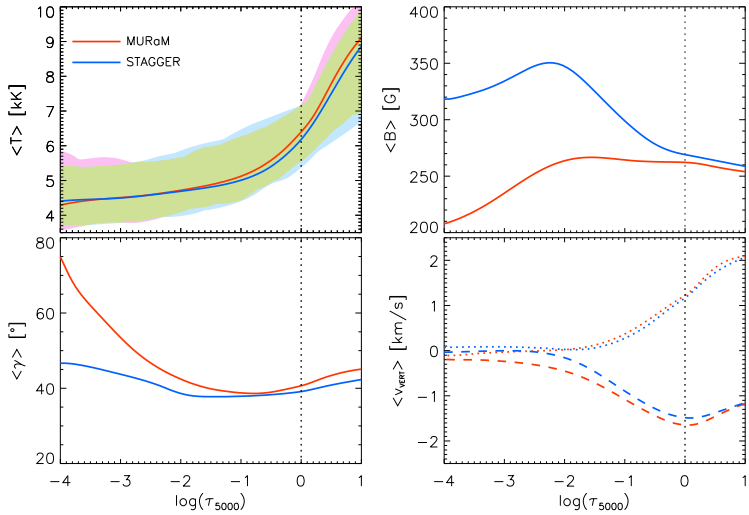

Figure 2.2: The mean temperature (*upper left*), the mean total magnetic field (*upper right*), the mean inclination angle of the magnetic field defined in the range $\pm 90°$ (*lower left*), and the mean vertical velocity (*lower right*). The averaging of quantities was performed over the iso-τ_{5000} surfaces. The mean velocity is shown separately for the upflowing (dotted) and for the downflowing (dashed) material. The blue curves correspond to the STAGGER distributions and the red curves the MURaM ones. The colored areas in the upper left panel show the range of the mean temperature at each optical depth (pink, MURaM; pale/light blue, STAGGER; green, the overlap). The dotted vertical line in all panels indicates $\tau_{5000} = 1$. All the plots are clipped to the range of $\log \tau_{5000} \in [-4, 1]$.

The mean temperature for MURaM and STAGGER is similar over the entire optical depth range, as seen in the upper left panel of Fig. 2.2. The MURaM mean model is cooler (by ≈ 100 K) at the very top layers ($\log(\tau_{5000}) \sim -4$). The two models are virtually identical for $-3.5 \leq \log(\tau_{5000}) \leq -2$. Finally, the MURaM mean model is hotter for $\log(\tau_{5000}) > -2$ (in particular, at continuum-forming layers). The difference with the STAGGER mean model reaches up to ≈ 250 K for the deepest layers (in the optical depth range $\log(\tau_{5000}) \sim 1$). Therefore, the MURaM mean model has slightly larger mean temperature gradient throughout the photosphere. The colored areas in this figure panel show the range of the mean temperature values in the two simulations at each optical depth. The range is similar at all optical depths. At top photospheric layers the MURaM run reaches significantly hotter temperatures (the highest MURaM temperature being up to ≈ 400 K hotter than the highest STAGGER value), as well as generally slightly cooler temperatures. However, as already seen, at such high layers the MURaM average stratification tends to be slightly below that of the STAGGER run. In the mid-photosphere, the STAGGER simulation reaches slightly cooler and slightly hotter values. In the deeper part of the simulation boxes, i.e. below continuum-forming layers (i.e., in the optical depth range $\log(\tau_{5000}) > 0$), the hottest pixels of the MURaM run are hotter than those of STAGGER (while the latter still shows the coolest pixels of the two runs).

The upper right panel in Fig. 2.2 highlights the different behaviour of $\langle B \rangle$ for optical depths above the surface, where STAGGER has larger mean magnetic field than MURaM. In the plot showing the average inclination angle of the magnetic field (lower left panel), the STAGGER and MURaM iso-τ_{5000} distributions are similar for the deeper part of the simulation boxes ($-1 \leq \log(\tau_{5000}) \leq 1$). The STAGGER curve stays within $\langle \gamma \rangle = 37^\circ - 47^\circ$ at all heights, while the inclination in MURaM for $\log(\tau_{5000}) < -1$ increases more rapidly, and very markedly starting for layers above $\log(\tau_{5000}) \approx -2$, with the field finally becoming nearly vertical at the top of the optical depth range. This is due to the boundary condition in the MURaM run, which forces the magnetic field at the boundaries of its simulation box to be vertical (Vögler 2003, Ch. 3.4.1), while potential field extrapolation is used in the STAGGER run, causing $\langle \gamma \rangle$ to assume a value of about 45 degrees at the top of the simulation domain. The vertical velocity (lower right panel) is averaged separately for pixels showing upflow and downflow motions at $\tau_{5000} = 1$ (unit optical depth). The two simulation runs have a remarkably similar mean velocity stratification in each of the two components. The mean 1D stratifications give initial confidence that the two codes provide overall similar results in the hydrodynamical part (temperature and velocity), but they also indicate rather different magnetic field topology, likely due to the different top boundary condition for the magnetic field. In the next subsec-

tion we show and analyze the projection of the physical quantities on the iso-τ surfaces to compare the two snapshots in more detail.

2.4.2 Maps of the physical variables

Figure 2.3 shows maps and histograms at the $\tau_{5000} = 1$ optical depth level for the temperature, vertical component of the magnetic field, inclination angle of the magnetic field and vertical velocity for the first saved snapshots of the MURaM and STAGGER runs. The corresponding maps for the $\tau_{5000} = 0.1$ and for the $\tau_{5000} = 0.01$ optical depth levels are available in Fig. 2.4 and Fig. 2.5, respectively. Next to each pair of maps, we show the corresponding normalized histograms to complete the picture.

We compare these maps with the findings of Buehler et al. (2015), who performed spatially-deconvolved inversions of the Hinode SP/SOT observations of faculae/plage. In their data, they identified the cores of strong magnetic concentrations and the surrounding canopy. We used their criterion for pixels in our snapshots, namely identifying as "core" pixels those with $B > 1000$ G at $\log(\tau_{5000}) = 0$ and magnetic field strength decreasing with height, and as "canopy" pixels those having $B > 300$ G at $\log(\tau_{5000}) = -2.3$ and magnetic field strength increasing with height. Canopies and cores can be explained because it has been proposed that the magnetic field has small-scale closed loop or vault like canopy around the network cores (McIntosh & Judge 2001; Schrijver & Title 2003). In the canopy structure we find weak-field plasma, where the magnetic field spreads out over the region until it is blocked by the magnetic field of the opposite part of the region and is forced again in the vertical direction (see i.e. Jurčák et al. 2006; Kuridze et al. 2008). The contours plotted over the maps in Figs. 2.3, 2.4, and 2.5 show the spatial distribution of the cores and the canopies.

In all maps, the MURaM and STAGGER snapshots show familiar features and properties of solar convection (Nordlund et al. 2009; Stein 2012), such as hot bright expanding upflowing plasma in granules and cool dark downflowing drafts of dense (compressed) plasma in intergranular lanes. The magnetic field is organized at meso-granular scales with strong concentrations of predominantly vertical field between the granules (Cattaneo et al. 2001; Vögler 2003). Locally, these fields are organized as points and ribbons having temperature at $\tau_{5000} = 1$ higher than the temperature of the surrounding downflows, but lower than the hottest granular tops. Higher up in the atmosphere, the granulation pattern reverses (Leenaarts & Wedemeyer-Böhm 2005; Cheung et al. 2007, e.g) and at $\tau_{5000} = 0.1$ the magnetic elements are the hottest structures in the map (whilst at $\tau_{5000} = 0.01$ their temperature is comparable to that

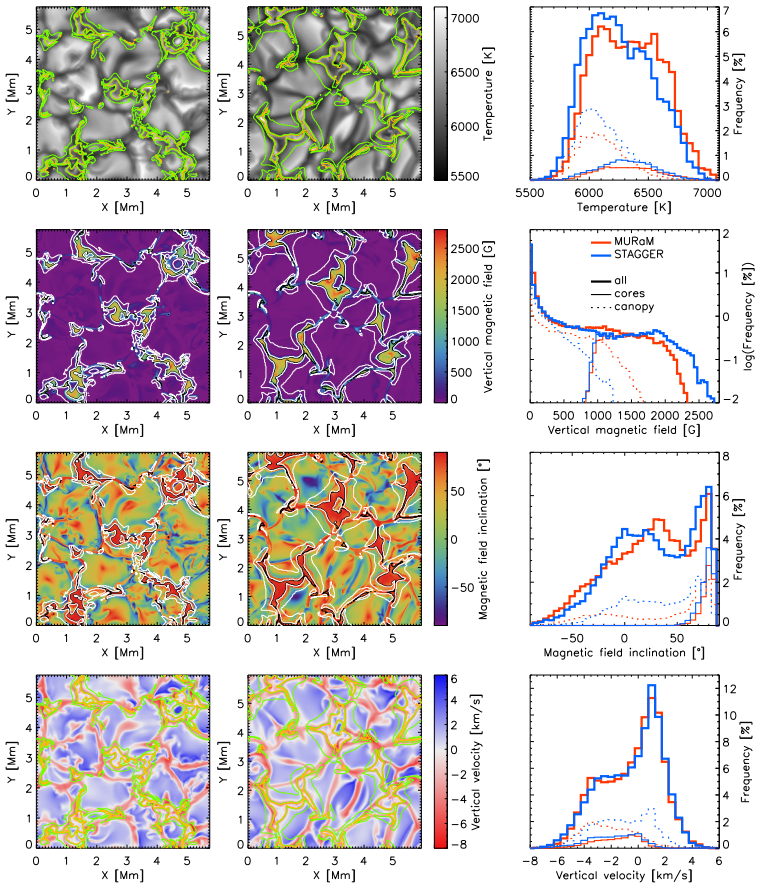

Figure 2.3: Maps at $\tau_{5000} = 1$ for `MURaM` (left column) and `STAGGER` (middle column), and the corresponding histograms (right column). From the top to the bottom: temperature, vertical magnetic field strength, magnetic field inclination angle, and vertical velocity are shown. The contours show the spatial distribution of the cores (orange in the first and the last row, black in the second and the third) and the canopies (green in the first and the last row, white in the two middle rows).

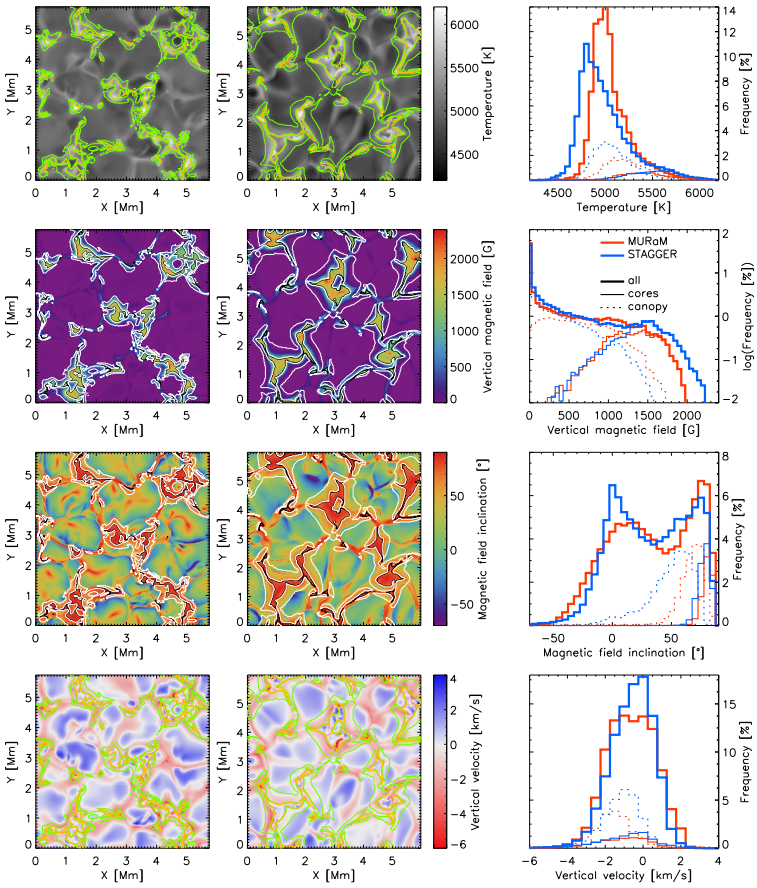

Figure 2.4: Same as Fig 2.3, but here for $\tau_{5000} = 0.1$.

of the hot component of the reverse granulation). In all four quantities, the MURaM run appears less diffusive, showing more fine structure than the STAGGER simulation, especially within the downflows.

Focusing now on the temperature at $\tau_{5000} = 1$ (Fig. 2.3, first row), the

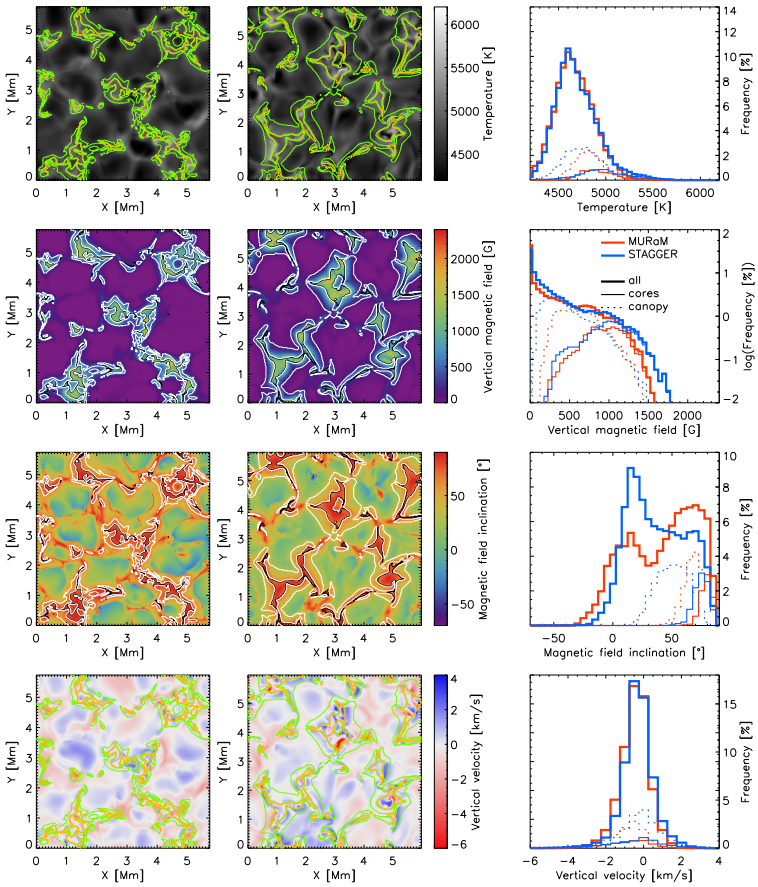

Figure 2.5: Same as Fig 2.3, but here for $\tau_{5000} = 0.01$.

histogram of the MURaM temperatures is shifted towards higher values, and it has a flat top with a hint of two populations, as opposed to the STAGGER data. The biggest difference between the two histograms appears at around $T = 6700$ K, corresponding to the high granular layers in MURaM being hotter

than in STAGGER, causing an excess in the mean temperature stratification (Fig. 2.2) and the brighter continuum (see Sect. 2.4.1). The MURaM snapshot is still significantly hotter than STAGGER at $\tau_{5000} = 0.1$, but they have nearly identical distribution at $\tau_{5000} = 0.01$ in agreement with Fig.1. The change from granulation to reverse granulation qualitatively follows the change seen in Fig. 13 of Buehler et al. (2015). Quantitatively, the simulations show a somewhat wider range in temperature. Although the PSF has been deconvolved in the inversion process of Buehler et al., their pixel size is still considerably larger than the grid cell of the simulations (approximately by a factor of 15 in area) leading to intrinsic smearing even with δ-function PSF. The partial histograms (normalized to the total number of pixels) for the cores and canopy identified in the simulation are shown Fig. 2.3 (solid and dotted thin curves, respectively). At the three optical heights, the temperature distribution in the cores shows an excellent match between the two codes. In the canopy, there is a good agreement in the shape of the histograms at $\tau_{5000} = 1$, whilst the STAGGER distribution is systematically cooler than the MURaM one higher up in the model[4].

All these results can be directly compared to the histograms in Fig. 14 of Buehler et al.: at $\tau_{5000} = 1$ the agreement between the observations and the cores in the two snapshots is excellent, with all distributions peaking at about the same value (6300 K). At increasing heights, the observations suggest slightly higher temperature in the cores than found in the simulations. This discrepancy may be due to the limited temperature sensitivity of the Fe lines.

The vertical component of the magnetic field (Fig. 2.3, second row) has a similar distribution at $\tau_{5000} = 1$ in both snapshots. The magnetic field concentrations are dominated by the field strength of 1.5 to 2 kG. The strongest vertical fields in the STAGGER snapshot are stronger than the strongest ones in MURaM, as it may be expected since the field used to initiate the STAGGER run was $\approx$ 24 G stronger (see Sect. 2.3.1). From the histograms of the two snapshots, it is clear that the difference in the strong-B tail is due to a small fraction of all pixels. The difference in the vertical magnetic field strength remains similar at $\tau_{5000} = 0.1$ and $\tau_{5000} = 0.01$, in accordance with Fig. 2.2. The distribution of the vertical component of the magnetic field in the cores shows a nearly perfect match between the two codes at all three optical depths. At $\tau_{5000} = 0.01$ (close to $\log(\tau_{5000}) = -2.3$, the actual value where the canopy was defined in Buehler et al. (2015)) the two histograms show similar shapes,

[4]However, note that the canopy is defined from $\log(\tau_{5000}) = -2.3$ maps and thus the contours at $\tau_{5000} = 1$ in Fig. 2.3 correspond to the material underneath the canopy, not to the canopy itself.

with the STAGGER canopy having a larger relative area and a slightly weaker field. Our histograms of the magnetic field in the cores can be compared to Fig. 5 of Buehler et al.: the range of values (between 800 G and 2.3 kG) and the median (1.5 kG) agree remarkably between observations and simulations.

In both snapshots the strongest vertical fields at $\tau_{5000} = 1$ are oriented within 25° around the vertical direction (Fig. 2.3, third row). Outside the magnetic concentrations both histograms reveal a population of inclined fields. However while the distribution of the MURaM inclinations peaks at 30°, in STAGGER it is nearly horizontal. When moving up through the snapshot, there is an evident difference between the two codes: in the STAGGER snapshot the frequency of nearly horizontal fields increases with height, and clearly dominates at $\tau_{5000} = 0.01$, with the fully developed canopy; opposite to that, in the MURaM snapshot the inclined fields become more inclined, but there is less of them, while the population of fields with inclination between 50° and 90° increases significantly (compare the 3rd row histograms in Figs. 2.3, 2.4 and 2.5). The differences in magnetic field inclination and its distribution are likely due to a combination of two factors: a slightly different $\langle B \rangle$ and, more significant, a different top boundary condition for B. The latter directly affects the size of the canopy, making it easier to develop further in the STAGGER case. On the other hand, the ratio of areas occupied by the canopy and the cores is 2.52 and 2.82 for MURaM and STAGGER, respectively. It is also worthwhile noting that MURaM at all three optical heights has more occurrence of magnetic field with negative inclination (opposite polarity). These pixels are located in the downdrafts surrounding magnetic elements. The MURaM snapshot shows overall more small scale structure, especially at the granular edges and in between the granules, suggesting that this run is less diffusive. The distribution of the field inclination in the cores shows another aspect where there is good agreement between the two simulations at all heights. In the canopy, the field in the MURaM run is less inclined than in the STAGGER one, in accordance to the already explained difference in canopy appearance. Nevertheless, the observations of Buehler et al. (2015) (the left panel of their Fig. 17)[5] show more inclined field in the cores (up to 60° from the line of sight) and a nearly horizontal field in the canopy. This is the only remarkable difference between their observations and our simulations.

The vertical velocities at $\tau_{5000} = 1$ in Fig. 2.3 display the same pattern in the maps and in the histograms for the two codes. With increasing height, the two distributions narrow down in a similar way, with the MURaM one exhibiting a flatten top histogram at $\tau_{5000} = 0.1$, and slightly shifted to more negative

[5]Note that the inclination in their work is measured in the range from 0 to 180°.

velocities at $\tau_{5000} = 0.01$. A comparison with the lower-right panel of Fig. 2.2 shows that this difference is mainly due to the mean MURaM downflows being faster than the STAGGER ones. The histograms in the cores of the MURaM and STAGGER snapshots match each other closely at all heights, and show an excellent agreement with the observations of Buehler et al. (2015): the magnetic cores in all three are nearly at rest, whilst the surrounding material contains narrow downflows. These downflows are visible in our histograms in the form of a negative-velocity tail[6].

Figure 2.6 shows the mean stratification within the magnetic cores and the canopy identified in Fig. 2.3. All quantities are averaged over iso-τ_{5000} surfaces. The temperature stratifications of the cores and the canopies derived from MURaM match well those derived from STAGGER, with MURaM showing a slightly steeper gradient in the canopy and less steep in the cores. The difference between the cores and the canopy for both codes fits well expectations from semi-empirical models (Keller et al. 1990; Solanki & Brigljevic 1992). The strength and the inclination of the magnetic field show again significant differences between the two MHD runs, due to different magnetic field boundary conditions at the top of the respective simulation boxes. In the MURaM run, the magnetic field everywhere at the top of the domain is forced to be vertical (thus, resulting in a small difference there between the cores and the canopy in B and γ), whilst in STAGGER at the top of the domain the magnetic field in the canopy is still significantly more inclined than the field in the cores. The vertical velocity (bottom right panel of Fig. 2.6) for the canopy shows curves with similar shape for the two codes, but with a range of values that significantly differ. The MURaM canopy has downflows that reach nearly -2 km/s at $\tau_{5000} = 1$, while they do not exceed -1 km/s in the case of the STAGGER run. For higher layers ($\tau_{5000} \lesssim 0.01$) in the canopy, MURaM predicts downflows and STAGGER upflows, both of the order of a few hundred m/s. The curves for the magnetic cores indicate that the velocity has a smaller gradient with height in the MURaM snapshot, with a velocity difference of less than 400 m/s at any depth in the line formation region ($\log \tau_{5000} \in (-2, 0)$).

[6]Note that Buehler et al. use the spectroscopic convention for velocity, therefore in their case it is the outward propagating material (upflows) which is characterised by negative (radial) velocities (decreasing distance between source and observer).

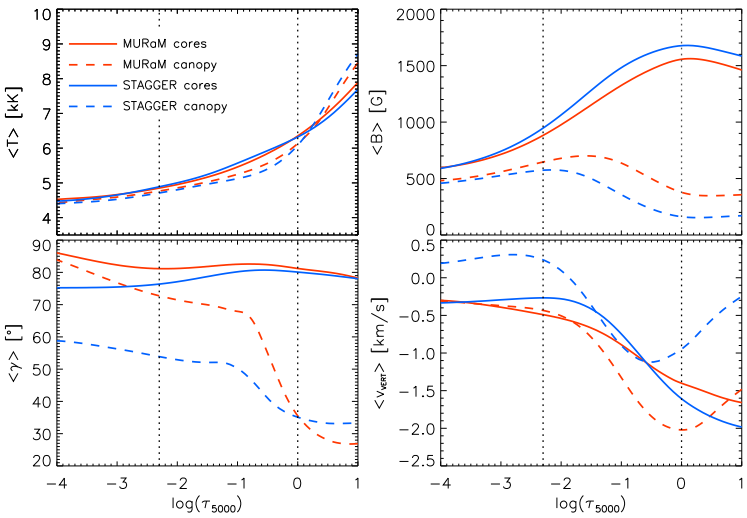

Figure 2.6: The temperature (*upper left*), the total magnetic field (*upper right*), the inclination angle of the magnetic field (*lower left*) and the vertical velocity (*lower right*) averaged over the iso-τ_{5000} surfaces separately for the cores of the magnetic concentrations (solid curves) and for the surrounding canopy (dashed curves). The blue curves correspond to the `STAGGER` distributions and the red curves to the `MURaM` ones. The dotted vertical lines indicate $\log(\tau_{5000}) = 0$ and $\log(\tau_{5000}) = -2.3$, the optical depth levels used to define the cores and the canopies, respectively.

2.5 Results: *synthetic observations*

2.5.1 Mean continuum intensity

We compute the continuum intensity in the 4.000-16.000 Å wavelength range from the snapshots and, for comparison, from the Harvard Smithsonian Reference Atmosphere (HSRA, Gingerich et al. 1971). Figure 2.7 shows the computed continuum intensities (HSRA: black line; `MURaM`: red; `STAGGER`: blue) and (in grey color) the Fourier Transform Spectrometer (FTS) solar atlas of Neckel (1999). Note that, as could be expected from a semi-empirical model, the HSRA intensity values are similar to those characterising the pseudo-continuum of the FTS atlas. In the figure, `MURaM` closely coincides with HSRA, while the synthetic continuum computed for the `STAGGER` run is systematically lower than

those two in the entire wavelength range, with a maximum difference of $\sim 10\%$ at 4000 Å.

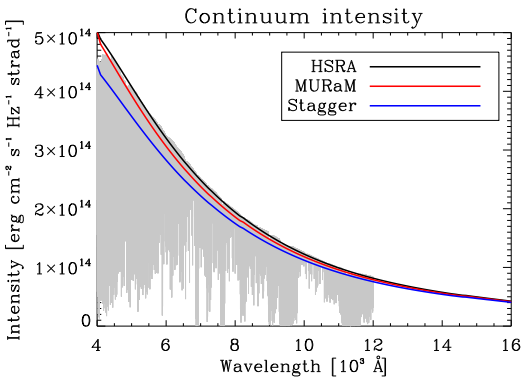

Figure 2.7: Continuum intensity from the HSRA model (black curve), STAGGER (blue curve) and MURaM (red curve) (adopting the Wittmann opacity package in all cases), and from the FTS solar atlas (gray colour).

The differences in continuum intensity may be explained by different bottom boundary conditions used in the two simulations. The mass inflow at the bottom of the MURaM simulation is regulated so that the emergent radiative flux fluctuates around a prescribed value that corresponds to the quiet Sun radiative output ($6.3 \cdot 10^{10}$ erg s^{-1} cm^{-2}), which explains the good match of the MURaM results with HSRA (a model representing the quiet Sun). On the other hand, the radiative output of STAGGER is not driven by the code to the solar value, resulting instead as a consequence of the bottom entropy adopted by the user for the simulated physical processes. In this case, thus, the adoption of approppiate input bottom entropy values has to be checked a posteriori after the simulation run. In the case of the STAGGER data we employed here, the effective temperature of the resulting snapshots was within $\sim \pm 20$ K of the solar value.

The magnetic field adopted in these facular-like simulations is sufficiently strong to affect the granulation and partly inhibit the convective energy transfer, thus leading to the output atmospheric models in the STAGGER run generally being cooler and darker than those in the MURaM one. This explanation needs to be verified by detailed analysis of the non-local processes in both simulations, and by evaluation of the impact of differences in the opacities adopted

in the *a posteriori* spectral synthesis as compared to those originally used by the simulation codes. This is, however, outside the scope of our present study.

2.5.2 Mean Stokes line profiles

The spatially-averaged intensity profiles we obtained for the Fe I 6301.5 Å and 6302.5 Å lines are shown in the left panel of Fig. 2.8, together with the observed profiles from the "Hamburg" FTS atlas of the solar disc centre intensity (Neckel 1999).

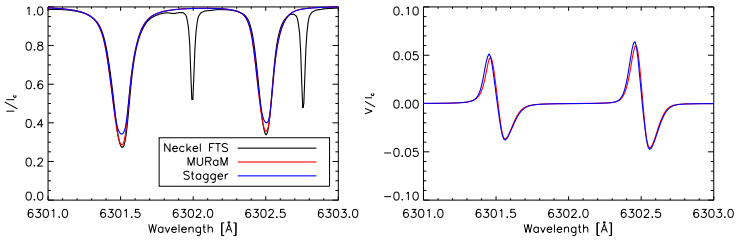

Figure 2.8: Mean profiles of the Fe I spectral lines for Stokes I (*left panel*) and Stokes V (*right panel*) in `MURaM` (red) and `STAGGER` (blue) snapshots. The synthetic Stokes I profiles are shown together with the FTS solar spectrum (black), which includes two O_2 lines formed in the Earth's atmosphere.

The wings of the `STAGGER` and of the `MURaM` Stokes I profiles of the Fe I lines show an exceptionally good match of the observed profiles. Small differences with the FTS atlas data in the line wings could be expected, since our simulations represent a plage region with strong magnetic field and the overall kinematics somewhat differ from those of the quiet Sun, which the FTS atlas data should be representative of. The line width depends mainly on the thermal, Doppler, and Zeeman broadenings, which are related in highly non-linear ways to the temperature structure and to the structure of the velocity and magnetic field. To disentangle the effects of these three would require extensive tests outside the scope of this investigation. The excellent agreement found seems to indicate, in any case, that the summed effects felt by the wings of the two Fe I lines due to the presence of strong magnetic field are negligible.

The line centre intensity of the synthetic Fe I profiles, instead, differs quite significantly between the `STAGGER` and `MURaM` results. The `MURaM` Fe I profiles show only slightly shallower absorption at line centre than the FTS ones, while the `STAGGER` profiles are significantly weaker (almost 0.1 in normalised intensity). The fact that the two Fe I line cores reach deeper in the `MURaM` case than

in the STAGGER one can be understood by looking again at Fig. 2.2. The mean temperature changes by roughly 1500 K between $\tau_{5000} = 1$ and $\tau_{5000} = 0.01$ (the approximate formation range of these Fe I lines, see Khomenko & Collados 2007). One sees, however, that the mean temperature stratification of the MURaM model has significantly higher gradient (the MURaM mean temperature reaching higher values than STAGGER in the deep layers). The cores of the two Fe I absorption features we consider sample relatively high atmospheric layers. We thus cannot exclude that the difference between the synthetic line cores may be influenced by the top boundary in the STAGGER simulation being ≈ 100 km lower than in MURaM.

The slightly stronger magnetic field in the STAGGER run induces a somewhat larger splitting of the Zeeman components in the line profiles, making them wider and, thus, shallower. As previously discussed though, the Zeeman broadening is in itself generally small for spectral lines in the visible spectral range, and the very good match of the respective line widths in the synthetic line profiles signifies that this broadening contribution does not play a dominant role when compared to the Doppler and thermal effects.

Regarding the difference between the synthetic and observed line core intensities, we firstly remark that we do not here take into account non-LTE effects (Shchukina & Trujillo Bueno 2001). However, the correction for these lines are nearly negligible if we consider the studies done by Bergemann et al. (2012) and Lind et al. (2017), who found smaller corrections than Shchukina & Trujillo Bueno (2001). Moreover, regarding the solar Fe abundance we adopted for the spectral synthesis, if we had employed the lower (by 0.05 dex) value in the latest update (Scott et al. 2015) in the series of 3D HD solar abundance compilations initiated by Asplund et al. (2000b); Asplund (2000), the synthetic profiles from both runs would be even weaker. Even when high-fidelity data are used i.e. with all care taken to reduce errors on the observational side, the effects of magnetic fields, departures from LTE, and adopted input atomic and opacity data make the problem of matching the solar spectrum and deriving the solar chemical composition particularly difficult. For example, since magnetism is present on the Sun and its indirect effect is to weaken the cores of the two Fe I lines, it is expected that a slightly higher value for the input Fe abundance should be adopted than in the non-magnetic case to match observations.

In the right-hand panel of Fig. 2.8 we show the Stokes V profiles of the two Fe lines computed from the two codes. The STAGGER Stokes V profiles of both spectral lines are slightly wider and stronger than the MURaM ones due to the $\sim 10\%$ stronger magnetic field in the former simulation run. We will return to this question in Sect. 2.5.5 where we discuss spatially resolved area and amplitude asymmetries of Stokes V.

2.5.3 Continuum intensity maps and histograms

The continuum intensity maps at 6300 Å, each synthesised from one representative snapshot of the MURaM and of the STAGGER simulation run, are compared in the upper row of Fig. 2.9. Each of the two maps is normalised to the respective mean intensity. In the lower row of Fig. 2.9 the continuum maps are shown after smearing and re-binning to match the Hinode resolution. The color scale and the range of values are identical for all panels. The respective histograms are shown next to the maps (panels in third column of Fig. 2.9).

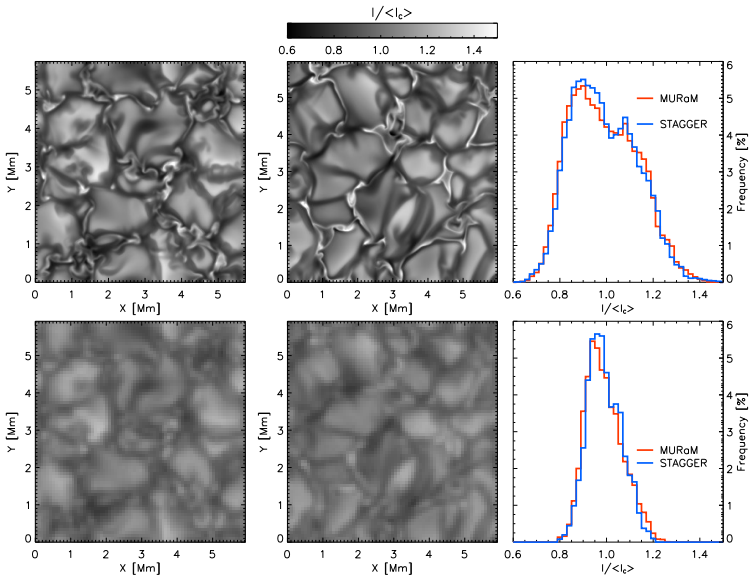

Figure 2.9: Continuum intensity maps for MURaM (*left*) and STAGGER (*middle*) snapshots, and their respective histograms (*right*) normalised to the mean value of each one. Upper row: at the simulation resolution; lower row: after the synthetic data is spatially degraded to the resolution of SP/SOT onboard the HINODE satellite.

At the simulation resolution the two snapshots have a very similar range of normalised continuum intensities, with the darkest pixels at a value of 0.6 and the brightest ones at ≈ 1.5 of the mean intensity. The RMS contrast of the continuum at 6300 Å is 14.4% for MURaM and 14.3% for STAGGER at the

simulation resolution, and 7.9% and 7.5% respectively after smearing. These results are close to the values found in the MURaM quiet-Sun simulations (14.4% and 7.5%) and in the Hinode observations (Danilovic et al. 2008).

The width of the histograms of the continuum intensity at 6300 Å at the full resolution is similar for the two runs although its double-peaked shape is more pronounced for STAGGER. This difference disappears at the Hinode resolution. The brightest areas in both snapshots are small bright-points located in the intergranular lanes. Comparison with the second row of Fig. 2.3 reveals that these are the location of the strongest magnetic concentrations with the vertical component of the magnetic field up to 2.3 kG for MURaM and 2.7 kG for STAGGER at $\tau_{5000} = 1$ (2.0 and 2.2 kG at $\tau_{5000} = 0.1$, and 1.6 and 1.8 kG at $\tau_{5000} = 0.01$, respectively). In Fig. 2.10, we compare the continuum intensity versus the total magnetic field strength at $\tau_{5000} = 1$ for the two snapshots. Both simulations show the typical hook shape (Shelyag et al. 2007; Vitas et al. 2009; Danilovic et al. 2016).

Another difference between the two snapshots at full resolution is in the shape of the brightenings related to magnetic elements: in MURaM these brightenings (and the magnetic elements, see Fig. 2.3) have their peaks in the centres of the lanes, while in STAGGER we see them often split in two ribbons with a region of reduced B in the middle. In MURaM they also appear more wiggly, while they remain rather stretched in STAGGER. This replicates different appearance of the magnetic elements in the simulation variables and, therefore, it is likely to be due to different numerical schemes and artificial diffusivities used in the two codes. At the Hinode resolution the two snapshots look indistinguishably similar and their histograms are almost identical.

2.5.4 Stokes I

In Fig. 2.11, we present maps and histograms of line centre intensity, equivalent width and FWHM for MURaM and STAGGER simulation runs for the Fe I 6301.5 Å line. The corresponding figure for the Fe I 6302.5 Å line is shown in the Fig. 2.12. To more easily compare the results, in Table 2.3 we list the mean value and the standard deviation of the three line parameters for each line.

The mean STAGGER line profiles (Table 2.3) are less deep and, therefore, the STAGGER snapshot appears brighter in the line core. The difference is especially clear in the granular tops (where MURaM is considerably darker) and in the magnetic elements (where STAGGER shows more bright points). These differences due to the temperature gradients in the MURaM snapshot, are present in both the mean model (Fig. 2.2) and in the temperature maps at $\tau_{5000} = 1$ and $\tau_{5000} = 0.1$ (cf. Fig. 2.3 and 2.4, note that MURaM is hotter at $\tau_{5000} = 1$

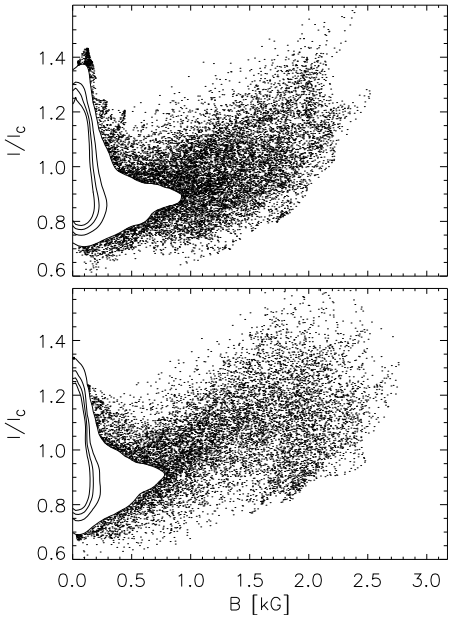

Figure 2.10: Continuum intensity at 6300 Å versus the total magnetic field strength at $\tau_{5000} = 1$ for `MURaM` (upper panel) and for `STAGGER` (lower panel). The contours are set to the same density levels in both panels.

Table 2.3: Mean values of the line centre intensity, equivalent width and FWHM for both lines (Fe I 6301Å and Fe I 6302Å) and their statistic deviations for `MURaM` and `STAGGER` snapshots.

	`MURaM`		`STAGGER`	
	Fe I 6301Å	Fe I 6302Å	Fe I 6301Å	Fe I 6302Å
$\langle \mathrm{I_{CORE}} \rangle \pm \sigma_{\mathrm{I_{CORE}}}$	0.27 ± 0.10	0.34 ± 0.16	0.32 ± 0.10	0.38 ± 0.14
$\langle \mathrm{EW} \rangle \pm \sigma_{\mathrm{EW}}[\mathrm{Å}]$	0.13 ± 0.02	0.10 ± 0.02	0.13 ± 0.03	0.10 ± 0.02
$\langle \mathrm{FWHM} \rangle \pm \sigma_{\mathrm{FWHM}}[\mathrm{Å}]$	0.15 ± 0.02	0.13 ± 0.03	0.15 ± 0.02	0.14 ± 0.03

and cooler at $\tau_{5000} = 0.1$). The standard deviation of I_{core} in both snapshots is similar.

Finally, the mean values of EW and the full-width half-maximum for the two lines and the two simulation runs have same mean values and dispersion

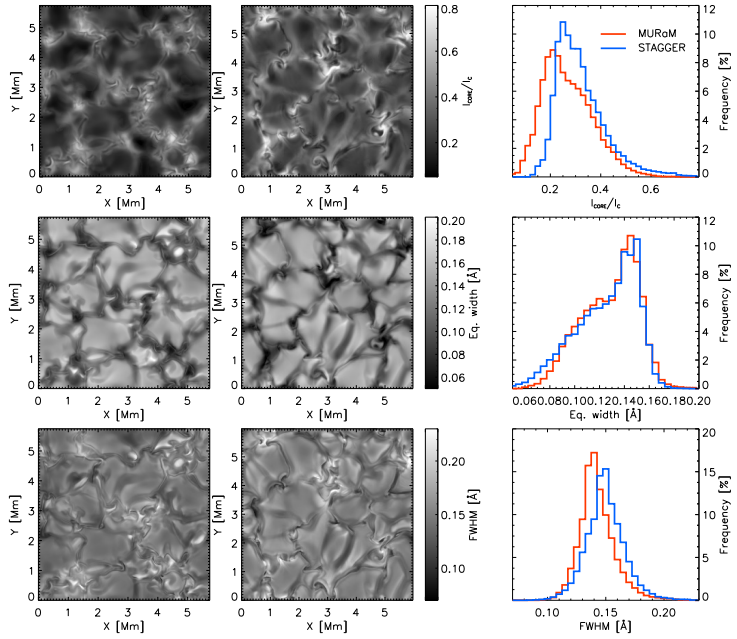

Figure 2.11: *From top to bottom*: line-centre intensity (I_{CORE}), equivalent width (EW) and full width at half maximum (FWHM) are shown. *Left panels* correspond to the results for MURaM snapshots, *middle panels* are for Stagger snapshots, and *right panels* are the corresponding histograms. These results are presented for the Fe I 6301.5 Å line. The results for the Fe I 6302.5 Å line are shown in the Fig. 2.12.

until the second decimal (see Table 2.3).

2.5.5 Stokes V

As pointed out above, the radiation field can be expressed in terms of the Stokes parameters, where I is the intensity of the light (the parameter that we were analyzing before in this chapter). Moreover, Q and U characterize the linear polarization, being Q the difference between the light polarized linearly at 0°and at 90°and U the corresponding between 45°and -45°. Finally, the Stokes V represent the difference between the light circularly polarized right-

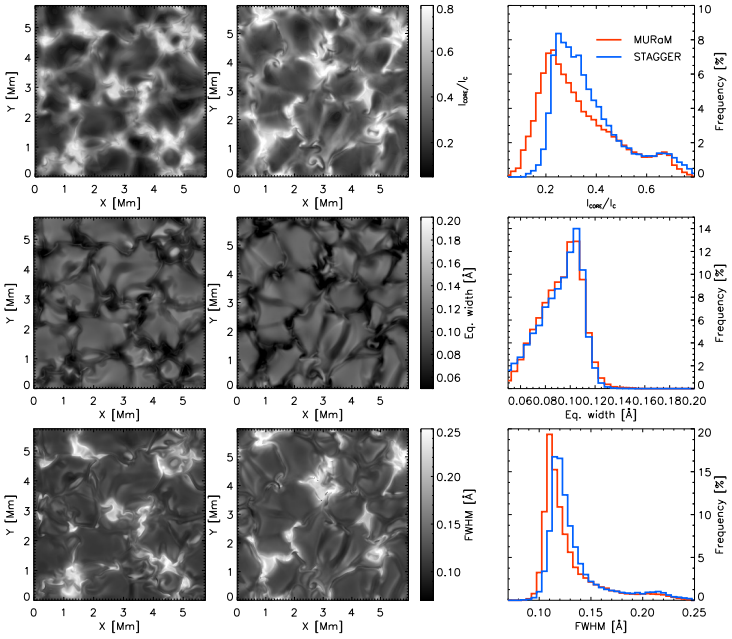

Figure 2.12: Same as Fig 2.11, but here for Fe I 6302.5 Å.

handed and left-handed. In this section, we are going to analyze the Stokes V profiles computed from the simulation snapshots because they show many deviations from the antisymmetric two-lobes shape. These deviations reflect the complex variation of the magnetic field, the velocity and the temperature along the line of sight.

Number of lobes. The first indicator of the profile complexity is the number of lobes. Khomenko et al. (2005) defined all profiles with two lobes as "regular" and used only them in their asymmetry analysis. The magnetic field of the individual column-atmospheres in the snapshots has many small-scale variations of the physical parameters with height, especially at the weak-field locations, causing tiny fluctuations in the circular polarization in the essentially noise-free synthetic profiles. It is, thus, impractical to count the lobes of these profiles

simply by counting zeros of the profile function. Instead, prior to counting the lobes, we introduce an artificial amplitude-depending threshold to discard the small intensity variation around zero circular polarization. All profiles are normalized to their own continuum intensity and the threshold t is set to eliminate all wavelength points in Stokes V profiles with values t-times smaller than the maximum normalized amplitude of the profile. Alternatively, we could model realistic noise with constant level for the entire sample. However, by doing that some of the weak profiles and their lobes would be discarded and our aim is to compare the profiles of the two simulations also at the weak-field locations.

Table 2.4: Fraction of profiles at the simulation resolution depending on the number of lobes

	MURaM		STAGGER	
n lobes	Fe I 6301 Å	Fe I 6302 Å	Fe I 6301 Å	Fe I 6302 Å
2	75.7	77.3	79.3	82.1
3	10.4	11.5	9.7	10.1
4	11.8	9.7	9.1	6.8
5	1.5	1.2	1.1	0.8
6	0.6	0.3	0.8	0.2

The abundance of profiles depending on their number of lobes at the simulation resolution is shown in Table 2.4. The results obtained from the two simulations are very similar. The slightly higher number of the two-lobes regular profiles in the STAGGER simulation is possibly due to slightly stronger field in that simulation. The profiles with more than two lobes are located within the granules (the least magnetic regions) and have weak absolute amplitudes. After applying the PSF, the fraction of "regular" profiles in both simulations is over 99% and it remains at that level after re-sampling to the pixel size of SP/SOT, and after applying the instrumental profile. Khomenko et al. (2005) in their simulation with $\langle B \rangle = 140$G found 31% of the regular profiles at the simulation resolution (same grid spacing and size of the simulation domain as in our experiment) and 17% after the image degradation using a PSF slightly narrower than the one we use here (the resolution of their synthetic observation is 0.5 arcsec corresponding to a telescope with a 70 cm-mirror). Comparison with other simulations of Khomenko et al. (2005) with less $\langle B \rangle$ reveals that the fraction of the regular 2-lobes profiles decreases with the field strength. Our result fits perfectly into that trend.

Stokes V asymmetries. The formation of the Stokes V asymmetries in the solar photosphere is still an open question. There is a number of interpretations

considering different topologies of the magnetic and velocity field, but also observational effects. Steiner (2000) reviews some of the possible scenarios.

The formation of asymmetries in Stokes V profile could be explained considering an atmosphere with two layers of separate flow and magnetic properties, like we show in Fig. 2.13. The first layer is extended from τ=0 to τ=τ_1 and it has a vertical magnetic field without a velocity. The second layer is extended from τ=τ_1 to τ=∞, and it is field-free but has a vertical velocity. The transition region at τ=τ_1 is called *magnetopause*.

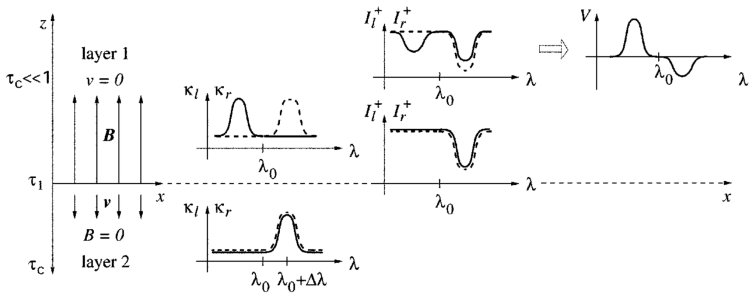

Figure 2.13: Representation of how the asymmetries in Stokes V are formed from an atmosphere with two layers of separate flow and magnetic properties. κ_l and κ_r represent the opacity for right (*dashed curve*) and left (*solid curve*) circularly polarized light. $I^+_{l,r}$ are the corresponding outgoing intensities. This figure has been taken from Steiner (2000).

In layer 1, a spectral line will split due to the Zeeman effect and in layer 2, velocity shifts the spectral line to the red or to the blue. Thus, the outgoing intensities in the τ_1 layer are superposed; but then, considering the Zeeman effect over the absorption coefficient, there are two lobes in the left circularly polarized intensity and only one in the right one, which is also deeper. Since we know that the emerging Stokes V profile at optical depth τ=0 is V = I^+_r - I^+_l, we find that the Stokes V profile is asymmetric, with the right lobe smaller than the left lobe. Therefore, to have asymmetries in Stokes V profiles one needs to have a magnetopause between two layers; but also, we need to have very deep lines, because in weak lines the effects balance out and there is no asymmetry. One must note that in this study, we do not consider the emission of the magnetic layer.

Thus, the area, δ_A, and amplitude, δ_a, asymmetry of Stokes V profiles are important quantities indicating gradients of magnetic and velocity field along the line of sight (Illing et al. 1975; Solanki 1989). The two quantities are defined

as:

$$\delta_a = \frac{\mid a_b \mid - \mid a_r \mid}{\mid a_b \mid + \mid a_r \mid} \tag{2.1}$$

$$\delta_A = \frac{\int V \mathrm{d}\lambda}{\int \mid V \mid \mathrm{d}\lambda}, \tag{2.2}$$

where a_b and a_r are the amplitudes of the blue and the red lobe of Stokes V profile, and V is the profile itself.

Various types of Stokes V asymmetries are observed in the quiet Sun and active regions. Their complexity is interpreted in terms of one-dimensional 1- or 2-component models of magnetic concentrations (Grossmann-Doerth et al. 1988, 1989; Martínez Pillet et al. 1997; Grossmann-Doerth et al. 2000; Bellot Rubio et al. 2000; Steiner 2000; López Ariste 2002; Sigwarth 2001; Socas-Navarro et al. 2004) or in terms of 2D (Sigwarth et al. 1999) and 3D simulations (Khomenko et al. 2005; Shelyag et al. 2007) of the quiet Sun and solar faculae/plage. Rezaei et al. (2007), with the SP/SOT Hinode, observed the internal structure of a magnetic element and the related asymmetries, and identified the same structure in 3D numerical simulations. Using the same instrument, Viticchié et al. (2011) observed the Stokes V asymmetries in the quiet Sun and interpreted them in terms of micro-structured atmospheres. In a sequel paper Viticchié & Sánchez Almeida (2011) performed a more detailed classification of the Stokes V shapes finding that 93% of all the profiles in their sample show asymmetries.

In Fig. 2.14, we show the amplitude asymmetries (δ_a) and in Fig. 2.15 the area asymmetries (δ_A), as they are defined by Eqs. 2.1 and 2.2, for the two snapshots and the Fe I 6301.5 Å spectral line. The upper row shows the quantities evaluated at the full resolution of the simulation; the lower row the quantities evaluated after the synthetic profiles have been degraded to the resolution of SP/SOT Hinode. The corresponding figures for Fe I 6302 Å are similar (see Fig.2.16 and Fig.2.17).

Some of the profiles are so distorted from the anti-symmetric shape that the above definition of the asymmetries makes little sense. A clear example of such profiles are those with two negative lobes or "two-humped profiles" (Steiner 2000); in our simulations such heavily distorted profiles always correspond to the low magnetic fields. Nevertheless, to compare our results with those of Shelyag et al. (2007), we applied directly Eq. 2.1 to all synthetic profiles including the extremely distorted ones. The distribution of our MURaM results (upper left panels of Figs.2.15 and 2.17) show the same pattern as in their Fig. 3 (the middle row, second and third column). The area asymmetry is dominantly positive with small negative patches located mostly at the granu-

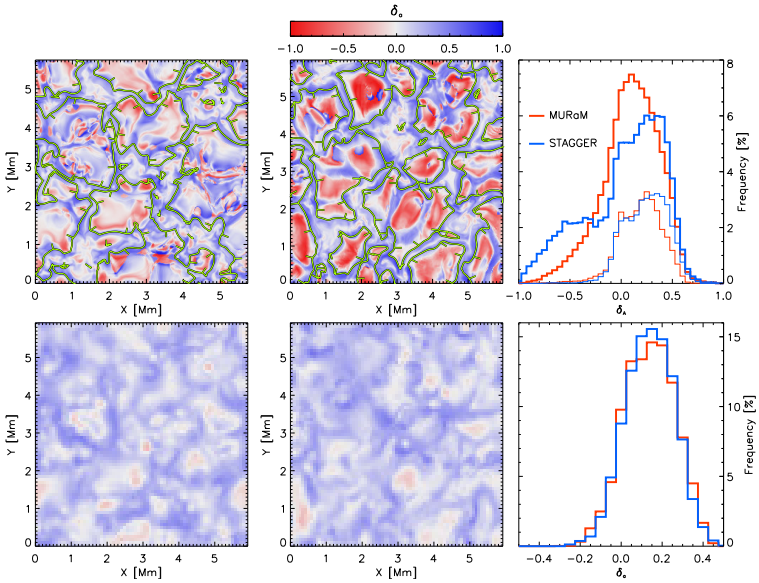

Figure 2.14: Stokes V amplitude asymmetry of Fe I 6301.5 Å from `MURaM` (*left panels*) and `STAGGER` (*middle panels*) snapshots at the simulation grid (*upper row*) and after degradation to the SP/SOT Hinode spatial and spectral resolution (*lower row*). The black contour separates locations with the absolute Stokes V above and below a threshold (see the text, the ticks at the contour indicate the low-amplitude side of it). Histograms in the *right column* compare the distribution of the amplitude asymmetry between the two codes. The thick curves count all profiles, the thin curves only the high-amplitude profiles. All histograms are normalized to the total number of pixels in each of the snapshots.

lar edges. On the other hand, at the simulation resolution there is a striking difference between `MURaM` and `STAGGER` in both asymmetries and in both lines: the `STAGGER` profiles (the top right panels of Figs. 2.14, 2.15, 2.16 and 2.17) show large patches of negative asymmetries that are entirely missing in the `MURaM` data. This difference is clearly visible in the corresponding histograms as well as in the mean values listed in Table 2.5. At the Hinode resolution (the lower panels of Figs. 2.14 and 2.16), however, the difference in the Stokes V asymmetries between the two codes disappear: both snapshots show only small patches of the negative asymmetry in dominantly positive distribution and the corresponding histograms match excellently.

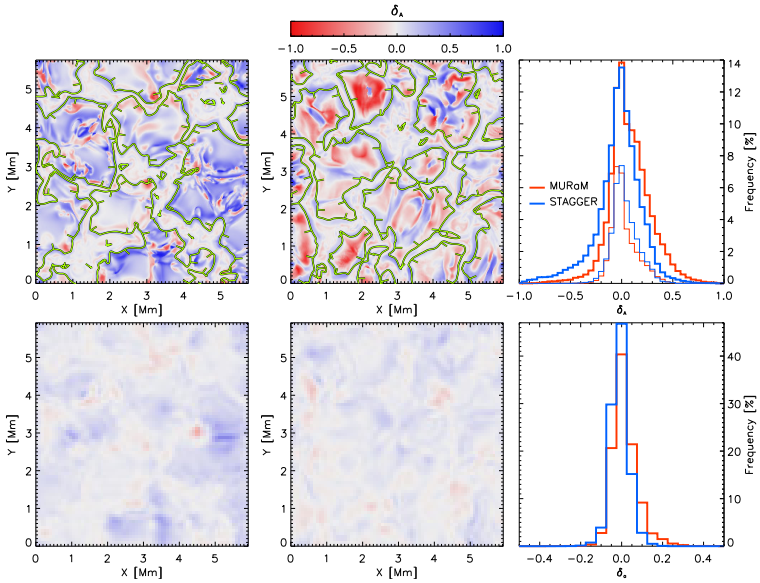

Figure 2.15: Stokes V area asymmetry of Fe I 6301.5 Å from MURaM (*left panels*) and STAGGER (*middle panels*) snapshots at the simulation grid (*upper row*) and after degradation to the SP/SOT Hinode spatial and spectral resolution (*lower row*). Histograms in the *right column* compare the distribution of the area asymmetry between the two codes. The thick curves count all profiles, the thin curves only the high-amplitude profiles. All histograms are normalised to the total number of pixels in each of the snapshots.

To explain the change in the distribution of the asymmetries with smearing, we added a contour to the panels with the simulation resolution showing where amplitude of the Stokes V profiles is larger than a threshold (8×10^{-2})[7]. The contours surround all the large patches of negative asymmetries that correspond to the locations of granular tops. Due to their low V amplitudes, these profiles contribute insignificantly to the asymmetry of the profiles at the Hinode resolution. Histograms of the asymmetries at the full resolution for the profiles with the V amplitudes above the threshold are added to the histograms in Figs. 2.14, 2.15, 2.16 and 2.17 (thin curves): they show a close match between the

[7] A similar threshold was applied to the Stokes V profiles in the work of Khomenko et al. (2005). Their threshold was 10^{-3}, but the mean field in their simulation was only 140 G.

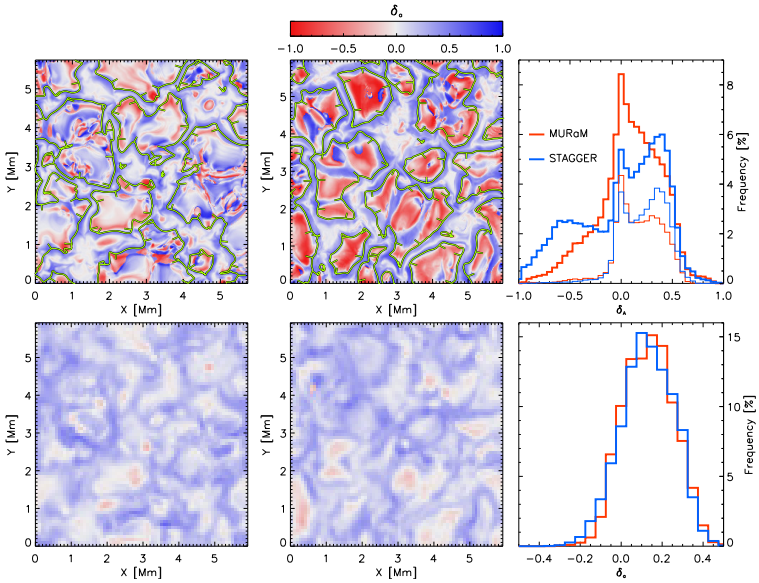

Figure 2.16: Same as Fig 2.14, but for Fe I 6302.5 Å.

results of the two codes.

Furthermore, Table 2.5 lists the mean values of the asymmetries for the cores of the magnetic field concentrations and the surrounding canopy sampled as in Buehler et al. (2015) and plotted over the maps in our Fig. 2.3. In the cores, the two snapshots show good match in both the area and the amplitude asymmetry, and at both resolutions. The 6301 line has larger δ_a, but smaller δ_A than the 6302 one at the full resolution, whilst both lines give the same result at the resolution of Hinode ($\delta_A \approx -0.01, \delta_a \approx 0.1$). The amplitude asymmetry in both lines is always positive. The mean area asymmetry can be both positive and negative. It has negative contribution from the magnetic core and positive from the canopy. This applies to both snapshots and in both Fe lines and it agrees with the observations of Martínez Pillet et al. (1997).

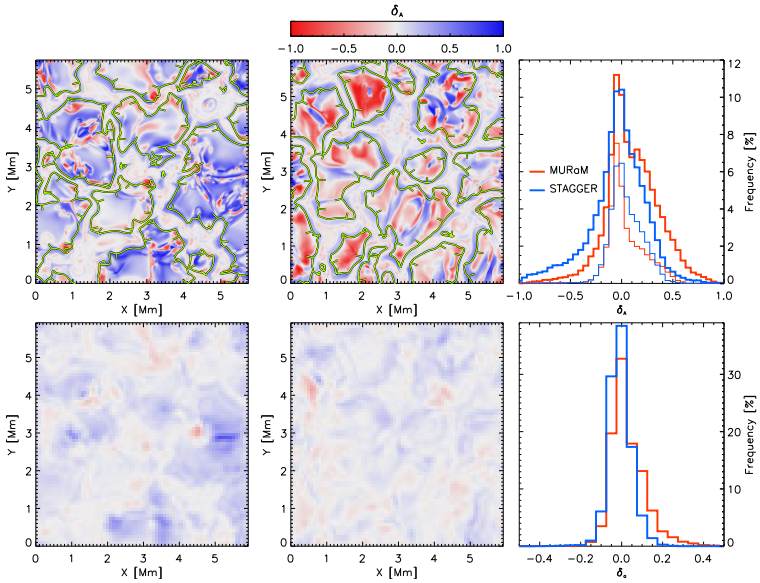

Figure 2.17: Same as Fig 2.15, but for Fe I 6302.5 Å.

Table 2.5: Mean Stokes V area and amplitude asymmetry computed for the two Fe lines from MURaM and STAGGER snapshots at the simulation resolution and after smearing the data

		Full resolution				Hinode resolution		
Code	Line [Å]	All	> 0.08	Cores	Canopy	All	Cores	Canopy
Amplitude asymmetry								
M	6301	0.118	0.211	0.072	0.214	0.164	0.111	0.176
	6302	0.111	0.197	0.040	0.194	0.160	0.093	0.157
S	6301	0.056	0.269	0.075	0.266	0.166	0.106	0.206
	6302	0.029	0.246	0.043	0.236	0.153	0.098	0.193
Area asymmetry								
M	6301	0.103	0.046	-0.033	0.048	0.040	-0.009	0.006
	6302	0.125	0.067	-0.042	0.067	0.057	-0.010	0.011
S	6301	-0.007	0.056	-0.033	0.084	0.016	-0.010	0.023
	6302	-0.017	0.071	-0.041	0.096	0.019	-0.011	0.031

2.6 Oxygen abundance

The objective of this chapter is to study in depth the three dimensional theoretical models and their influence in the solar abundances determination. Therefore, in this section, we take the 25 snapshots of each simulation to analyze the oxygen abundance that we obtain with them. We use the forbidden line in 6300 Å, which is one of the most frequently used oxygen lines due to its weakness and the fact it is formed very close to LTE conditions. However, it has a blend with a nickel line that has to be taken into account. We consider the two major isotopes of nickel, ^{58}Ni I and ^{60}Ni I, with a log(gf) value of -2.11 and a fraction of 72% and 28% for each isotope respectively (Johansson et al. 2003).

The `NICOLE` code was used to make the spectral synthesis of this line and the Sc II line close to it. Table 2.6 shows the atomic parameters of the lines synthesized. The Sc II line is introduced to check if the model represents the photosphere correctly enough to fit this line. To do that, we compare the synthesis with the Kitt Peak intensity FTS atlas by Neckel (1999). We perform the spectral synthesis in all of the 25 snapshots and then, we calculate the mean spectral line profile which is the one that we compare with the FTS, obtaining wider profiles that those of each snapshot separately. We point out that, despite of using theoretical models, we need to add an enhancement to the velocities in order to compensate for missing dynamics in the lower layers of the atmosphere, where these weak lines are formed, as evidenced by too narrow synthetic line profiles. However, we can not indicate a reason that explains why this widening is necessary in our case and not in other studies (e.g., Asplund et al. 2000a; Fabbian et al. 2010).

We follow the procedure of Socas-Navarro (2015), and we multiply all velocities in the snapshots by a factor to obtain a good fit of the Sc II line. Once we get a good fit of the Sc II line, we follow a "trial to error" procedure to get the oxygen abundance, which means that we make the synthesis taking abundances approaching to the better fit with the FTS atlas.

The values obtained after synthesize each snapshot and obtaining the mean intensity profile for `MURaM` and `STAGGER` simulations are presented in Table 2.7. Moreover, Fig 2.18 shows the fit of the mean profile of `MURaM` (upper panel) and the same for the `STAGGER` simulation (bottom panel) for the oxygen (left) and scandium (right) lines.

It is clear from the figure that we get a good fit of the spectral lines. However, the models present discrepancies with the atlas in the continuum region between the two lines, where they set the continuum to a higher level. It is probably produced by CN absorption lines as Allende Prieto et al. (2001)

Ion	λ [Å]	χ [eV]	log(gf)	γ_{rad}	γ_{Stark}	γ_{Waals}
[O I]	6300.304	0.000	-9.717[a]	0.0	0.05	1.00
^{58}Ni I	6300.335	4.266	-2.253[b]	2.63	0.054	1.82
^{60}Ni I	6300.355	4.266	-2.663[b]	2.63	0.054	1.82
Sc II	6300.678	1.507	-1.898[c]	2.30	0.05	1.30

Table 2.6: Adopted atomic parameters. χ is the excitation potential. γ_{rad}, γ_{Stark} and γ_{Waals} are the radiative, the Stark and the van der Waals damping parameters (units 10^8 $rad\ s^{-1}$). The log(gf) are taken from: [a] Storey & Zeippen (2000), [b] Johansson et al. (2003), [c] VALD database. We note here that the log(gf) values for the ^{58}Ni I and ^{60}Ni I isotopes are calculated taking the 72% and 28% of the gf value of Ni, which is $10^{-2.11}$ (Johansson et al. 2003).

	log(ϵ_O)	log(ϵ_{Ni})	log(ϵ_{Sc})	v$_{factor}$
MURaM	8.66	6.16	3.09	1.10
STAGGER	8.60	6.15	3.04	1.30

Table 2.7: Values obtained for the oxygen, nickel and scandium abundances, as well as the velocity factors for the MURaM and STAGGER simulations.

pointed out. Moreover, we note that the winds of both lines are not flat because the solar spectrum contains spectral lines at both sides of the spectral region represented in the figure, and the continuum is affected by the winds of these other spectral lines.

The values for oxygen abundance in the case of MURaM simulation are completely compatible with the low-Z value of log(ϵ_O)=8.66±0.05 (Asplund et al. 2004). However, the oxygen abundance obtained with STAGGER is lower. The difference between the results of the two codes could be due to the temperature close to the continuum is different between the snapshots of STAGGER and MURaM by around 250 K, being the MURaM snapshots hotter than the STAGGER ones. Moreover, the fact that the magnetic field in the STAGGER simulation is higher than in the MURaM simulation, even though is small, it could certainly have an effect of the derived abundance in the correct direction (lower abundance for the STAGGER models).

Fabbian & Moreno-Insertis (2015) carried out a study with STAGGER simulations of $\sim$ 50 G, $\sim$ 100 G, and $\sim$ 200 G, where the 200 G case correspond to the same simulation that we use here. Their best fit was obtained, in the case of $\sim$ 200 G, with an oxygen abundance of log(ϵ_O)=8.73 and with a nickel abundance of log(ϵ_{Ni})= 6.22. There are numerous factors that may contribute to create the big difference between their results and ours:

- they used two spectral lines, the [O I] lines at 5577 and 6300 Å, while we only use the last one;

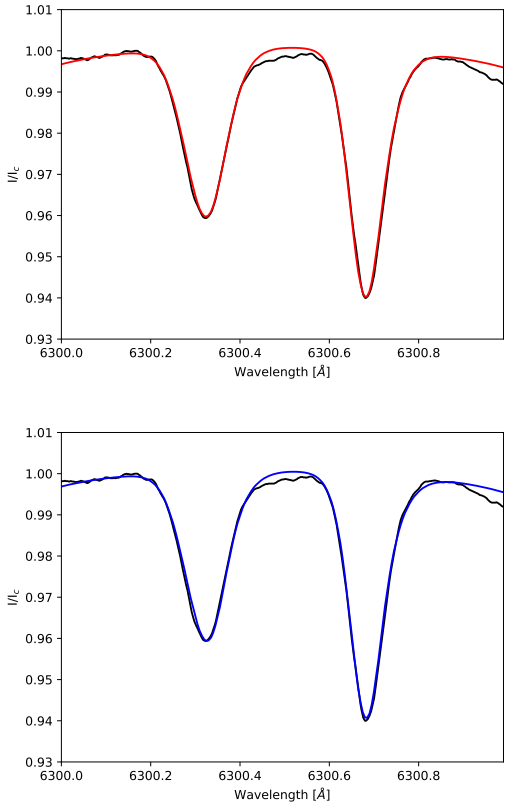

Figure 2.18: Oxygen (*left*) and scandium (*right*) lines at 6300 Å, black profiles correspond to the FTS, red profiles are a fit of one `MURaM` model (*upper panel*), and blue profiles correspond to a fit of one `STAGGER` model (*bottom panel*).

- they did their study considering just one simulation snapshot, while we have a subset covering a temporary interval;
- they have less spatial resolution that us, since they took 63x63 horizontal

points and 64 points in depth;

- their spectral synthesis is carried out with the RH code (Uitenbroek 2001; Pereira & Uitenbroek 2015), while we employed the NICOLE code.

All of these factors could be enough to explain the difference found. Furthermore, in the case of STAGGER is not very easy to adjust the temperature of the model to the solar one, and in the case of 200 G a variation of ±20 K could exist.

Finally, we note that the abundances of scandium obtained are in agreement with values found in the literature, e. g. $\log(\epsilon_{Sc})$=3.04±0.13 of Pehlivan Rhodin et al. (2017). The same happens for the nickel abundance, which is compatible with the value of Scott et al. (2009).

2.7 Conclusions

We analyzed results of 3D MHD simulations of the solar plage performed by two well-known and much-used numerical codes and initiated with similar setups. In addition, we compared radiative diagnostics synthesized from these results at the grid resolution of the simulations and after these diagnostics are spatially and spectrally smeared to the resolution of the SP/SOT Hinode.

The results of the two codes show an overall agreement, confirming the conclusions of the cross-validation study that Beeck et al. (2012) performed in the case of hydrodynamical quiet-Sun simulations. Both codes show similar convective patterns with kilo-Gauss magnetic fields concentrated in the intergranular space. The basic quantities (temperature, magnetic and velocity field) averaged over the iso-τ surfaces in both codes are similar as well. The distribution of physical quantities for the samples of 1D columns (extracted from the 3D snapshots) that are representative of the cores of the magnetic field concentrations and of the surrounding canopy, is nearly identical in the two codes, as well as exceptionally similar to that derived from spatially coupled inversions of a plage region recently observed with SP/SOT by Buehler et al. (2015). In addition to the comparison that we have done, it would also be interesting to compare in detail our synthetic line profiles to those in the data acquired by Buehler et al. (2015) as well as those they obtained after inversion/deconvolution.

Besides the overall similarity, there are differences in the details of the results of the two simulation runs that call for caution. Although the simulations differ only slightly in numerical diffusivities, equation of state, opacities, radiative transfer solution and geometrical grid, there are significant differences in

some of the boundary conditions (namely, in the way of adjusting the entropy at the bottom boundary and in the condition for the magnetic field at the top boundary) which are likely to cause differences in the results: the `MURaM` run is somewhat hotter across almost the whole range of optical depths considered, while the `STAGGER` one has more inclined magnetic fields in the mid photosphere. These differences leave imprints on the continuum and spectral lines computed from the snapshots. However, after smearing the radiative diagnostics to replicate the SP/SOT Hinode observations, the differences between the two simulation runs entirely disappear. Comparison with observations obtained with the new 4-meter class of solar telescopes (DKIST (Tritschler et al. 2016), EST (Collados et al. 2013)) and eventually with a next-generation space mission for solar data at ultrahigh spatial resolution (Collet et al. 2016) should clarify which (if any of the two) setup provides the most realistic solar simulations of solar faculae.

As far as we are aware, there is no comprehensive study on the effect of different numerical algorithms, mathematical implementations, and boundary and initial conditions in 3D solar/stellar atmospheric magneto-convection simulations. While this would certainly be interesting, it remains not only outside the scope of this work, but is in fact prohibitive (even without comparing different codes) due to the extremely time-consuming task of repeating such computationally-intensive 3D MHD calculations for a systematic test of each parameter. A few major efforts have, however, been accomplished at least for the non-magnetic case, providing important indications and hinting the way forward.

Regarding some of the key diagnostics that could be analyzed in future research efforts comparing the results of different 3D MHD codes between each other and with observations, these include: the center-to-limb variation of the emergent radiation in the continuum and in the spectral lines, the linear polarization signal, and the line profiles of other spectral lines that are more sensitive to certain physical parameters of the atmosphere.

With respect to the abundance analysis, we obtained an oxygen abundance of $\log(\epsilon_O)$=8.66±0.01 with the `MURaM` simulation, which is compatible with the low oxygen abundances obtained by some groups; for example Asplund et al. (2004) obtained $\log(\epsilon_O)$=8.66±0.05. However, when we used the `STAGGER` simulation, we got a lower abundance of oxygen, $\log(\epsilon_O)$=8.60±0.01, which is not compatible with the work of Fabbian & Moreno-Insertis (2015), who got $\log(\epsilon_O)$=8.73 using the same simulation. We are not sure of the exact reason why this difference happens, however, we have noted several factors that may have influenced. Finally, we emphasize that can not be concluded that three-dimensional theoretical models give low-Z abundances, since Caffau and

collaborators had obtained intermediate-Z values with models computed with CO^5BOLD (Caffau et al. 2015). Thus, we conclude using three-dimensional empirical models obtained from observations seems like a good avenue to take. This is the purpose of the following chapters.

3

Uncertainties in the solar photospheric oxygen abundance

Most of the contents of this chapter are published in Cubas Armas et al. (2017).

3.1 Introduction

The solar chemical composition is still under debate, the case of oxygen being particularly important. On one hand, some studies found a relatively low oxygen abundance (e.g. values between $\log(\epsilon_O) = 8.60$ to 8.69, Socas-Navarro & Norton 2007; Pereira et al. 2009a; Grevesse et al. 2010); but, on the other hand, high oxygen abundance has also been obtained (e.g. values between $\log(\epsilon_O) = 8.80$ to 8.90, Centeno & Socas-Navarro 2008; Ayres 2008; Socas-Navarro 2015). Perhaps an intermediate value, such as $\log(\epsilon_O) \approx 8.75$ (e.g., Caffau et al. 2008, 2015) might be able to satisfy all of the constraints if the uncertainties had been underestimated thus far.

A key factor in the abundance derivation is the solar atmosphere model used in the inference. It seems natural that a three-dimensional model should be preferred over a one-dimensional one. However, when the three-dimensional model is a numerical simulation and the one-dimensional model has been obtained empirically by fitting observations, it is not clear that the former is better than the latter for work that requires fitting observations, like the determination of abundances (Ayres 2008).

Deriving elemental abundances is far from trivial. The results are not determined solely by the solar atmosphere model used. They are also dependent of the solar observations adopted to fit the model, the atomic data and even

some details on the calibration (choice of the continuum level, spectrum rectification, wavelength calibration, etc). Recently, some studies have noted differences among solar atlases (e.g., Caffau et al. 2008, 2009; Doerr et al. 2016) and the need to use more than one in the analysis. In particular, Caffau et al. (2008) choose more than one solar atlas due to that, even if signal to noise is very high for solar spectra, the abundances obtained from different spectra do not always agree within one σ. Another obvious factor is the value of the employed oscillation strengths (parameterized in terms of $\log(gf)$), which have been discussed in some works (e.g., Storey & Zeippen 2000; Johansson et al. 2003). Thus, it is mandatory to establish all the sources of uncertainty and take them into account when solar abundances determinations are made.

In this chapter, we present a study of the oxygen abundance in the solar photosphere with the novelty that we applied Bayesian inference to properly disentangle the effects of the relevant parameters involved. In order to do that, we used a three-dimensional empirical model of the solar atmosphere (Socas-Navarro 2011, 2015) to fit the forbidden [O I] line at 6300.3 Å observed in two different solar atlases. In Section 2, we describe the solar model used, the syntheses made and the solar atlas observations. A summary of the Bayesian inference and a table with our priors are given in Section 3. Then, we present the results in Section 4 and, finally, some conclusions in Section 5.

3.2 Model atmosphere and observational data

3.2.1 Solar model

The solar atmosphere model that is used in this work was derived by Socas-Navarro (2011, 2015) based on observations of the SP (Lites et al. 2001b) of the SOT onboard the Hinode satellite (Kosugi et al. 2007b). The observations consist of a field of view located very close to the solar-disk center and the wavelength range covers from 6300.89 to 6303.27 Å with a sampling of 21.4 mÅ. The data is reduced from Level 0 to Level 1 following the procedures of Hinode SOT/SP and, after that, some other corrections are applied as explained in Socas-Navarro (2011). The spectrum for each pixel was inverted using the code NICOLE to determine a column with the height stratification of temperature, line-of-sight velocity, and magnetic field vector.

The inversion procedure consist of comparing the observational profiles with synthetic profiles (that are created as a function of some atmospheric parameters) and finding the synthetic profile that best fit the observations. The code follows an iterative process, where it applies perturbations to the variables of the model (for example, the temperature) to create a new synthetic profile.

Finally, the code outputs the model for which the synthetic spectra are most similar to the observational one. This similarity is calculated by an algorithm that minimizes the difference between the observational and synthetic profiles.

In this case, the inversions fit the profile shapes of the Fe I line at 6301.5 and 6302.5 Å simultaneously. Since these lines are affected by non-LTE effects, we introduced a correction using the departure coefficients computed by Shchukina & Trujillo Bueno (2001) in the 3D model of Asplund (2000). We take the departure coefficients in a typical granule and intergranular lane in the simulation and we assign them to a particular granule and lane in the observations. For all other pixels, we use linearly interpolated departure coefficient based on their continuum intensity. Although this method is not exact, it allow us to introduce non-LTE effects approximately much faster than of the full non-LTE problem is solved for every pixel.

In the inversion procedure the stratification of the model's variables is controlled by so-called *nodes*. The number of nodes selects the complexity of the stratification. For example, if we set only one node for a variable, the selected stratification is allowed to be modified with a constant. If we set two nodes, the variable could change linearly with optical depth, etc. Moreover, it is possible to choose the specific height at which we want the nodes. Besides to the nodes, there are also *cycles*, which are set of inversions. Making an inversion using more than one cycle is interesting. For instance, if we use two cycles, in the first cycle we can obtain a first approximation of the atmosphere by using few nodes; and in the second cycle we may use more nodes to obtain a better fit of the spectral lines. It could be better that using just one cycle with more nodes since the beginning, because it may produce complex stratifications that are not smooth and realistic.

Moreover, to obtain our model two components of the atmosphere were used, one magnetic and a one non-magnetic. It is an useful way to account for the existence of different structures inside one observational pixel. For example, the magnetic concentrations have sizes smaller than a granule and it is necessary to include both structures to determine the atmosphere accurately. To determine the non-magnetic component, the inversion is made taking into account only the Stokes I profile. The nodes used in each cycle are given in Table 3.2 and the atomic data used are shown in Table 3.1. For more details of the inversion procedure to create the model, the reader is referred to the two papers cited above.

λ [Å]	χ_e [eV]	log(gf)	Term (lower)	Term (upper)	σ [r_0^2]	α
6301.5	3.654	-0.718	$^5P_2$	$^5D_2$	834.4	0.243
6302.5	3.686	-1.160	$^5P_1$	$^5D_0$	850.2	0.239

Table 3.1: Spectral line data used in Socas-Navarro (2011).

	Magnetic pixel				Nonmagnetic pixel	
Physical	Inversion 1		Inversion 2			
parameter	Cycle 1	Cycle 2	Cycle 1	Cycle 2	Cycle 1	Cycle 2
Temperature	3	5	2	3	3	5
L.o.s velocity	1	3	1	2	2	3
Microturbulence	1	1	0	0	0	0
B_{long}	0	0	1	2	0	0
B_x	0	0	1	2	0	0
B_y	0	0	1	2	0	0
Filling factor	0	0	1	1	0	0

Table 3.2: Inversion nodes used. Table from Socas-Navarro (2011).

3.2.2 Observational data

In this study, we also intend to assess the impact of the choice of the specific solar observation on the abundance determination. Due to that, we used two different intensity atlases of the solar photosphere which have a good signal-to-noise (S/N) ratio and have been widely used in previous works (e.g. Caffau et al. 2008, 2009; Ayres 2008; Maiorca et al. 2009).

The first one is the disk center intensity atlas of the solar spectrum from 3000 Å to 10000 Å by Delbouille et al. (1973). The spectrum was obtained with a grating spectrometer at the International Scientific Station of the Jungfraujoch at 3580 m. The spectral resolving power varies from 1.250.000 to 500.000 and the signal to noise ratio is very high, being $\sim$ 6000 in the continuum at 6300 Å. The wavelength are given in the solar frame of reference and are corrected for the radial velocities of the observations, but not for the gravitational redshift. This atlas may be downloaded from the BASS2000 web server[1].

The second atlas that we considered was the Kitt Peak intensity FTS atlas by Neckel (1999)[2]. This atlas was produced with the FTS instrument at the McMath telescope at an altitude of 2096m, and spans the wavelength range from 3290 to 12510 Å. There are a disc-centre atlas (the one that we use here)

[1] http://bass2000.obspm.fr/solar_spect.php
[2] This atlas can be downloaded from https://github.com/aasensio/pyiacsun

and a flux atlas, both with a spectral resolving power of at least 350.000 (Neckel & Labs 1984; Neckel 1999). The signal to noise ratio is not specified but Doerr et al. (2016) measured at S/N $\sim$ 3000 in the continuum at 6300 Å.

Doerr et al. (2016) compared these two atlases very detailed taking into account the different instrumental degradations. From their Table 1, the FTS seems to be of higher quality than the grating spectrograph, but they found that the noise level on their figures is similar and that the spectral resolving power of the FTS is between two to six times lower than specified. Despite this, the authors found a remarkably good agreement between the two atlases.

3.2.3 Synthesis

Our main goal is to obtain the most probable value for the oxygen photospheric abundance using the forbidden [O I] line at 6300.3 Å and determine the uncertainties in this determination. Because of that, we synthesize the line profiles with NICOLE and compare them with those observed in different atlases of the solar spectrum (see previous section). To make the line synthesis, we select a wavelength range from 6300 to 6303 Å, including also the Fe I lines at 6301.5 and 6302.5 Å. We introduced the Fe I lines because the [O I] line is formed in the far wing of the 6301.5 Å Fe I line. Consequently, one needs to include this effect in our synthesis, since it affects the continuum estimate. To consider the nickel line in the feature of interest, we took into account the two major isotopes of nickel, ^{58}Ni I and ^{60}Ni I, with a log(gf) value of -2.11 and a fraction of 72% and 28% for each isotope, respectively (Johansson et al. (2003)). The atomic information of the spectral lines is shown in Table 3.3.

Since the spatial resolution of the observational atlases is extremely poor (of the order of tens of arcseconds), we mimic this resolution by averaging the profiles synthesized in all pixels of the snapshot. Moreover, we introduce an additional simplification in the forward modeling, given that the model of Socas-Navarro (2011) has 200×200 spatial pixels in the field of view. Synthesizing the wavelength range in each one of the 1000 models in our grid would be very computationally demanding. For this reason, we carried out a random selection of a subset of 1000 pixels, as a good compromise between accuracy and computational time, that produces an average profile that is equivalent to the average profile of the whole snapshot. By *equivalent*, we mean that the maximum difference between the average intensity profile of the full map and that of the subset is smaller than 0.1% in the oxygen line.

Given that the Bayesian analysis that we carry out (and we explain in the following section) requires the evaluation of several tens of thousands of forward models, it is convenient to pre-compute a grid of models and carry out

the Bayesian inference using a simulator that interpolates on the grid of models (O'Hagan 2006). This greatly accelerates the inference by several orders of magnitude. The precomputed database is built using a cartesian grid in all parameters of the model. The model parameters can be separated into two different classes: slow parameters, that require the re-computation of the synthesis in the whole snapshot because they affect the radiative transfer; and fast parameters, that can be applied directly to the profiles with simple manipulations.

The first two slow parameters are the oxygen and nickel abundances (note that the [O I] feature analyzed here has a Ni I blend as described in Sect. 2.6). The third slow parameter is an enhancement factor for the velocities in the lower layers of the snapshot. This parameter is introduced because the model of Socas-Navarro (2011) is constructed fitting the strong Fe I lines at 6301 and 6302 Å, and it misses some of the dynamics in the lower layers of the atmosphere, precisely where the oxygen line forms. Fortunately, the nearby Sc II line, very similar in strength and formation height to the [O I] line, is an excellent calibration tool for this missing turbulence, which we parameterize as a multiplicative enhancement factor applied on the velocities of the lower layers. For more details, see the discussion in Socas-Navarro (2011).

The fast parameters are: two for a linear correction of the continuum, a global velocity shift that takes into account imprecision in the wavelength calibration (this correction is important because a degeneration exists between the ratio of Ni and O abundances; this is explained in more detailed in sect 4.2 below) and the uncertainty of the fit.

To end up with a well-sampled database, we took ten possible values for each one of the slow parameters, resulting in a grid of 1000 models. The oxygen and nickel abundances were varied between typical values reported in the literature (see e.g., Grevesse et al. 1984; Anders & Grevesse 1989; Grevesse & Sauval 1998; Asplund et al. 2009). Their minimum and maximum values are shown in Table 3.4 together with those for the enhancement factor.

In summary, we constructed a grid of 1000 models where each model has 1000 pixels. For each one of them, we synthesized the spectral lines of interest using NICOLE, taking into account the atomic information compiled in Table 3.3. For the sake of reproducibility, the table also includes the references for the log(gf) values. The log(gf) value for the Fe I at 6302.5 Å was taken from Socas-Navarro (2011). The radiative, Stark and van der Waals damping parameters are also provided for each line except the Fe lines. For those, we give instead the α and σ damping parameters using the method of Anstee & O'Mara (1995) obtained with the code of Barklem et al. (1998).

Ion	λ [Å]	χ_e [eV]	log(gf)	γ_{rad}	γ_{Stark}	γ_{Waals}	σ	α
[O I]	6300.304	0.000	-9.717^a	0.0	0.05	1.00	...	...
^{58}Ni I	6300.335	4.266	-2.253^b	2.63	0.054	1.82	...	...
^{60}Ni I	6300.355	4.266	-2.663^b	2.63	0.054	1.82	...	...
Sc II	6300.678	1.507	-1.898^c	2.30	0.05	1.30	...	...
Fe I	6301.501	3.654	-0.718^c	...	...	...	834.4	0.243
Fe I	6302.494	3.686	-1.13	...	...	...	850.2	0.239

Table 3.3: Adopted atomic parameters. χ is the excitation potential. γ_{rad}, γ_{Stark} and γ_{Waals} are the radiative, the Stark and the van der Waals damping parameters (units 10^8 $rad\ s^{-1}$). The log(gf) are taken from: ^{a} Storey & Zeippen (2000), ^{b} Johansson et al. (2003), ^{c} VALD database. In the case of the Fe I lines, the γ_{rad} is introduced by NICOLE as calculated in Gray (1976).

3.3 Bayesian inference

3.3.1 Bayes theory

Bayesian inference is a useful mechanism to establish in a quantitative way how much uncertainty we have in our developments. Therefore, we employ its formalism (e.g., Gregory 2005) to quantify the uncertainties in our conclusions derived from the use of a prescribed model, a set of free parameters, and a set of priors (information known a priori).

To carry out a Bayesian inference, we need to specify what is the *a priori* information that we know about the problem. Once we do that, and we have the data, we the aim is to calculate the posterior distribution for the unknown parameters. The posterior distribution describes our uncertainties about the parameters considering the data available.

Bayesian inference relies on two fundamental tools. The first one is the Bayes theorem that describes very simply how the prior information is updated to the posterior information with the acquisition of new observations. If we denote the model parameters of interest with the vector $\boldsymbol{\theta}$, and the observations with D, the Bayes theorem states that

$$p(\boldsymbol{\theta}|D, I) = \frac{p(\boldsymbol{\theta}|I)p(D|\boldsymbol{\theta}, I)}{p(D|I)}. \tag{3.1}$$

In the Bayes theorem, $p(\boldsymbol{\theta}|I)$ is the prior probability distribution of θ, that encodes all the *a priori* information we know about the parameters (i.e., if a quantity is positive or if a certain region of the space of parameters is more probable than others, etc.). $p(D|\boldsymbol{\theta}, I)$ is the likelihood, which encodes the information about the model parameters that can be extracted from the obser-

vations. $p(D|I)$ is the model evidence, which does not depend on $\boldsymbol{\theta}$ and it is very important for model comparison, and $p(\boldsymbol{\theta}|D, I)$ is the posterior distribution, that describes everything that we know about the model parameters. The posterior distribution is usually narrower than the prior distribution, indicating that we learn something from the data and our uncertainties about the values of the parameters have decreased. Finally, I refers to any important context information that is necessary for the inference, in our case it is the specific radiative transfer model that we use, the 3D model, atmosphere, etc.

The output of the Bayes theorem is a probability distribution for θ indicating our knowledge about θ taking into account the data. We note that the denominator does not depend on θ. Hence, for parameter inference it is a normalizing constant that it is called evidence or marginal likelihood. The second fundamental tool is the marginalization, that is used to obtain the posterior distribution for any parameter taking into account the uncertainties and correlations with other parameters:

$$p(\theta_1|D, I) = \int \mathrm{d}\theta_2 \ldots \mathrm{d}\theta_n p(\boldsymbol{\theta}|D, I). \tag{3.2}$$

The most popular numerical techniques to apply Bayesian inference are the Markov Chain Monte Carlo (MCMC) methods which efficiently obtain samples from the posterior distribution. A Markov chain is a progression of points in parameter space generated by sequentially applying random perturbations. One of the most used algorithms is Metropolis-Hastings, but this algorithm suffers from the well known problem of slow convergence because it uses a random walk behavior to jump from one point to another. This slowness is especially relevant for hierarchical models, which are particularly hard to sample from. More advanced methods have been recently developed.

In this case, we use Nested Sampling (NS, Skilling 2004), which is not technically an MCMC algorithm. This method is very popular in astrophysics because, apart from sampling the posterior distribution, it also gives a good estimation of the evidence (or marginal likelihood). It is specially interesting in case of doing model comparison, for which the evidence is crucial. Moreover, nested sampling can work on harder problems (specially multimodal problems) than a simple Markov Chain Monte Carlo (MCMC). The idea of the nested sampling method is sampling the prior, cutting down the *volume* of the parameter space that it looks at into smaller and smaller ones. The procedure of this technique can be summarized as follow:

i) Produce N points in the parameter space from the prior and determine their likelihoods.

ii) Save the point with the lowest likelihood.

iii) Generate a new point from the prior distribution to replace the one found in the previous step. The likelihood of the new point must be greater that the previous one.

iv) Repeat the last two steps many times.

Thus, the nested sampling technique restricts the domain in which we are generating the points to the region where the likelihood is above the value of the likelihood of the point that we reject. There are some Bayesian computation software packages that use the nested sampling technique. We use the implementation of the Python package `nestle`[3], which uses the single ellipsoid method of Mukherjee et al. (2006). It consists on determining a single ellipsoid that hold all points and selects a new point randomly inside this ellipsoid.

3.3.2 Our analysis

In any Bayesian inference, it is crucial to define the priors. In our case, we define the priors as flat (meaning there is no preference) for almost all parameters in the ranges shown in Table 3.4. As it is shown in the Table, the ranges of the parameters are very small and flat priors can be considered to be quite uninformative on these ranges. The ranges have been chosen taking into consideration the results obtained in previous studies (see e.g., Grevesse et al. 1984; Anders & Grevesse 1989; Grevesse & Sauval 1998; Asplund et al. 2009) but trying not to discard parts of the space of parameters that might be compatible with the observations. The only non-flat prior is that of σ, for which we adopted a Jeffreys prior, $p(\sigma) \propto \sigma^{-1}$, because it is a scale parameter that can potentially have values spanning several orders of magnitude (e.g., Gregory 2005).

For computing the likelihood, we assume the following generative model:

$$O(\lambda_i) = I(\boldsymbol{\theta}, \lambda_i) + n(\lambda_i), \tag{3.3}$$

which states that the observations for the i-th wavelength point, $O(\lambda_i)$, can be modeled with a synthetic intensity profile, $I(\boldsymbol{\theta}, \lambda_i)$, plus some uncertainty, $n(\lambda_i)$, that has zero mean and diagonal covariance with variance σ^2. Following the standard approach (e.g., Gregory 2005) and under the previous assumptions, the likelihood has the form of an uncorrelated multivariate normal distribution, which reduces to:

$$p(D|\boldsymbol{\theta}, I) = \prod_{i=1}^{n} \frac{1}{\sqrt{2\pi}\sigma} \exp\left[-\frac{-\left[O(\lambda_i) - I(\boldsymbol{\theta}, \lambda_i)\right]^2}{2\sigma^2}\right], \tag{3.4}$$

[3]It can be obtained from `http://kbarbary.github.io/nestle/`.

Parameter	Range	Type
$\log(\epsilon_o)$	(8.55, 9.20)	Flat
$\log(\epsilon_{Ni})$	(5.84, 6.36)	Flat
v [km/s]	(-1, 1)	Flat
Enhancement factor	(0.5, 2.3)	Flat
σ	(0.0001, 0.02)	Jeffreys
Cont. slope $[I/I_c \cdot \mathring{A}^{-1}]$	(-0.1, 0.1)	Flat
Cont. y intercept $[I/I_c]$	(0.9, 1.1)	Flat

Table 3.4: Priors selected for each parameter of our analysis.

where n is the number of observed wavelengths.

3.4 Results

3.4.1 Spectral line fit

Figure 3.1 shows some representative fits of the [O I] and Sc II lines in our model (black lines) with respect to the atlases (Neckel in blue and Delbouille in green). The Neckel atlas is plotted in the left panel and the Delbouille atlas in the right one. Instead of a single fit, we provide a sampling of models that are compatible with the observations. They are obtained by synthesizing models with parameters extracted from the posterior distribution. It is clear from the figure that our model fits both atlases very well, even in very weak lines such as those shown here. However, the models present some discrepancies with the observations in the continuum region between the two lines, where the models set the continuum to a higher level. It is probably produced by CN absorption lines as Allende Prieto et al. (2001) pointed out. The lines of interest are very weak, thus, this region could potentially affect our abundance determination indirectly by setting the continuum level to an incorrect value. We tried to minimize this effect by introducing the Sc II line in the analysis, because this line helps to make a much better continuum level estimation.

3.4.2 Marginal posterior distributions

The joint and marginal posterior distributions for the five main parameters (oxygen and nickel abundances, velocity, enhancement factor and σ) are shown in Fig. 3.2. The blue distributions correspond to the inference made using the Neckel atlas while the green distributions correspond to the inference made comparing with the Delbouille atlas. We did not show the distribution for the

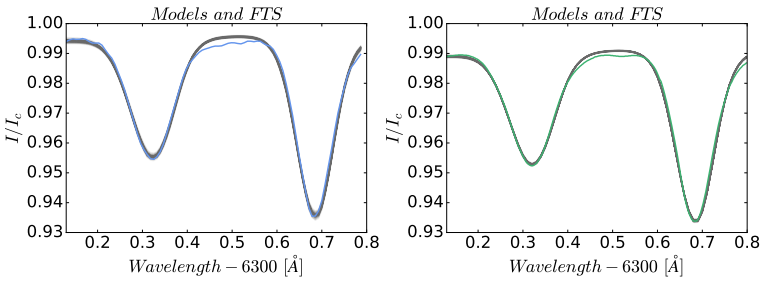

Figure 3.1: Some representative fits of the [O I] 6300.304 Å line and Sc II 6300.678 Å line are shown in black. The blue profile in the *left panel* corresponds to the Neckel solar atlas and the green profile in the *right panel* to the Delbouille atlas.

two parameters of the continuum because they are nuisance parameters that are only needed to have a good fit of the line, but they do not provide relevant information.

For both atlases, the joint and marginal posterior distributions show a Gaussian-like shape, where those corresponding to the Neckel atlas always present a larger width. This width indicates that the uncertainties in the abundances inferred from the Neckel atlas are larger than those obtained from the Delbouille atlas. Moreover, the marginal distribution for σ also shows that this parameter is smaller for the case of the Delbouille atlas. Thus, our model seems to provide more constrained model parameters and better fits for the Delbouille atlas.

It is encouraging that the marginal posterior for the oxygen abundance is consistent in both atlases, with that inferred from the Delbouille atlas being contained inside the uncertainty associated with the Neckel atlas. Further, it is interesting that the maximum marginal a posteriori (the peak of the marginal posterior) is located at approximately the same value for the two cases. This is not the same with the remaining parameters. The marginal posteriors corresponding to the Delbouille atlas tend to be shifted towards smaller values, except for the enhancement factor, where the opposite happens. In this last parameter, the marginal distributions even indicate that the inferred enhancement factors are not compatible (at least to three standard deviations).

If we look at the panels with the joint posteriors (showing the correlation between pairs of parameters), we see a clear correlation between the abundances of oxygen and nickel. This correlation is a direct consequence of the fact that the [O I] line is a blend; we can obtain an equally good fit if we take

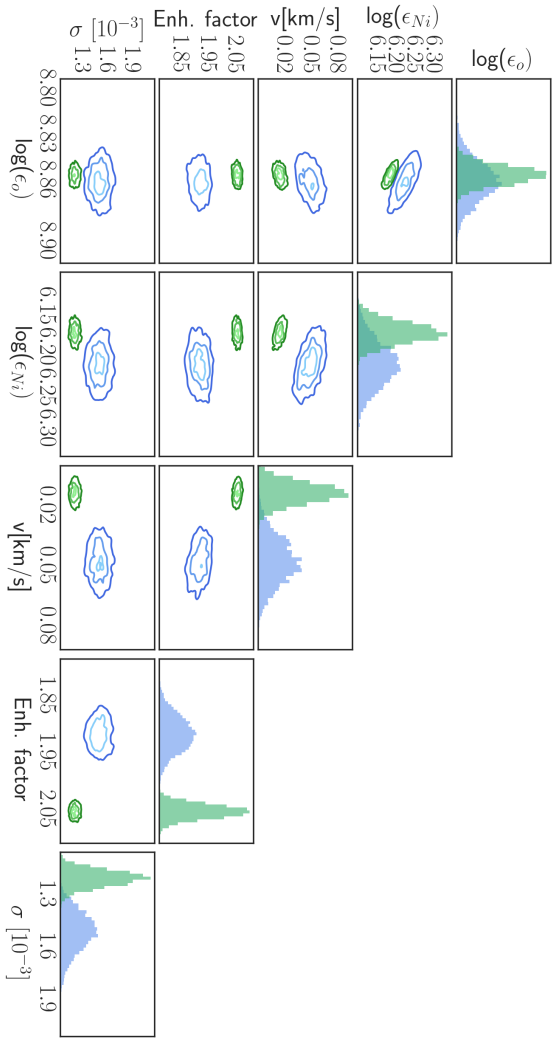

Figure 3.2: Histograms and correlations of the posterior distributions of the main five parameters (in blue for Neckel solar atlas and green for Delbouille atlas). From left to right, and top to bottom, we show: oxygen abundance, nickel abundance, velocity (in km/s), enhancement factor and σ.

a model with a higher nickel abundance and a lower oxygen abundance, and viceversa. Furthermore, these two parameters (oxygen and nickel abundances) are correlated with the velocity shift. This correlation makes sense for small velocities, since a wavelength shift displaces the line and one can still obtain a good fit by appropriately modifying the abundances. For example, a blue shift can be compensated with a lower nickel abundance and a higher oxygen abundance.

Since all marginal posterior distributions have a Gaussian-like shape, we summarize them in Table 3.5 by providing the median and the uncertainty defined by the percentiles 16 and 84 (equivalent to the standard 1σ uncertainty in the Gaussian case). It is clear in the table that the most probable value for the oxygen abundance is the same (down to the second decimal) for both atlases. The value obtained from this study is, hence, $\log(\epsilon_O) = 8.86 \pm 0.01$. This value is within the category of high solar oxygen abundances: lower than the 8.93 ± 0.02 value in Grevesse et al. (1984), but compatible with the 8.83 ± 0.06 revision in Grevesse & Sauval (1998).

Atlas	$\log(\epsilon_o)$	$\log(\epsilon_{Ni})$	v [km/s]	Enh. factor
Neckel	8.861 ± 0.014	6.22 ± 0.03	0.05 ± 0.01	1.92 ± 0.03
Delbouille	8.856 ± 0.006	6.18 ± 0.01	0.014 ± 0.005	2.05 ± 0.01

Table 3.5: Parameters median values and deviations for both atlases. The values for the uncertainties are $\sigma = 0.0015 \pm 0.0001$ in the Neckel atlas case, and $\sigma = 0.00120 \pm 0.00005$ in the Delbouille atlas.

3.4.3 More experiments

In order to quantify how much the impact of the continuum level and the correlation between the oxygen and nickel abundances are, we carried out two more studies. They are also intended to verify the robustness of our results.

In first place, we carried out the same analysis as above but reducing the wavelength range to take into account only the [O I] line. Although we do not display the fits or the marginal posteriors for simplicity, the summary of the results is displayed in Table 3.6 (see corresponding rows labeled as *Only [O I]* and *no prior*). For completeness, in this table, we repeat the results of the previous section for an easier comparison (labeled as *Both lines* and *no prior*). The results made with the Neckel atlas are labeled as N and the corresponding ones for the Delbouille atlas are labeled as D. Thus, modifying the range of wavelengths, the most probable oxygen abundance changes from $\log(\epsilon_O) = 8.86$, a value compatible with Grevesse & Sauval (1998), to $\log(\epsilon_O) = 8.94$, a

			$\log(\epsilon_o)$	$\log(\epsilon_{Ni})$	v [km/s]	Enh. factor
Both lines	N	prior Ni	8.864 ± 0.013	6.21 ± 0.03	0.05 ± 0.01	1.92 ± 0.03
		no prior	8.861 ± 0.014	6.22 ± 0.03	0.05 ± 0.01	1.92 ± 0.03
	D	prior Ni	8.858 ± 0.006	6.18 ± 0.01	0.014 ± 0.005	2.05 ± 0.01
		no prior	8.856 ± 0.006	6.18 ± 0.01	0.014 ± 0.005	2.05 ± 0.01
Only [O I]	N	prior Ni	$8.910^{+0.015}_{-0.019}$	6.02 ± 0.05	$0.17^{+0.03}_{-0.04}$	1.70 ± 0.04
		no prior	$8.940^{+0.007}_{-0.012}$	$5.90^{+0.06}_{-0.04}$	$0.23^{+0.01}_{-0.02}$	1.74 ± 0.04
	D	prior Ni	$8.937^{+0.004}_{-0.007}$	$5.88^{+0.04}_{-0.03}$	$0.171^{+0.007}_{-0.013}$	1.99 ± 0.02
		no prior	8.940 ± 0.002	$5.85^{+0.02}_{-0.01}$	$0.178^{+0.003}_{-0.004}$	2.00 ± 0.01

Table 3.6: Comparison of the results for the different experiments. The values for the uncertainties are, from the first row to the last one: $\sigma_1 = 0.0015 \pm 0.0001$, $\sigma_2 = 0.0015 \pm 0.0001$, $\sigma_3 = 0.00120 \pm 0.00005$, $\sigma_4 = 0.00120 \pm 0.00005$, $\sigma_5 = 0.00052 \pm 0.00005$, $\sigma_6 = 0.00050 \pm 0.00005$, $\sigma_7 = 0.00036 \pm 0.00005$, and $\sigma_8 = 0.00036 \pm 0.00002$.

value compatible with Grevesse et al. (1984). Nevertheless, this large oxygen abundance seems improbable in light of the very low nickel abundance inferred, which is incompatible with all previous reports in the literature (that usually give $\log(\epsilon_{\rm Ni}) > 6$). Because we are neglecting the wing of the Sc II line and the inferred abundance is different, we conclude that a good estimate of the continuum is crucial for the estimation of abundances.

The second test was motivated by the low nickel abundance of the previous results. In this case, we repeated the analysis, this time including a different prior for the nickel abundance. This prior was set to a Gaussian distribution with mean $\mu = 6.17$ and standard deviation of $\sigma = 0.07$, as reported in Scott et al. (2009). We intentionally increased the value of σ to decrease the informativeness of the prior and let the data drive the results. The results of this new analysis are also shown in Table 3.6 (with labels *prior Ni*). The results show that the inference implementing only the [O I] line is not reliable because, when including the Gaussian prior for the nickel abundance, the modification in the oxygen and nickel abundances is greater than the previously quoted uncertainties. This fundamentally means that the result is strongly dependent on the prior. However, this is not the case when using the [O I] and Sc II lines together, where we obtain results that are essentially insensitive to the prior.

3.4.4 Abundance and $\log(gf)$ factor

We are aware that an important source of uncertainty in the determination of abundances are the atomic parameters of the spectral lines, specifically the value of $\log(gf)$. We have tried to use the most recent determinations, but it

is true that a slightly different value of $\log(gf)$ would produce different oxygen and nickel abundances. Therefore, one can consider our determination of the abundance to be indeed an inference over the product $gf\epsilon_O$, which remains valid for weak lines.

The gf value used in this work (Johansson et al. 2003) is accepted as the most accurate, but its uncertainty can go up to 10%. This uncertainty translates into $log(gf) = -9.717 \pm 0.043$. If this is taken into account, it would induce an uncertainty in the oxygen abundance of ± 0.04.

3.5 Conclusions

There are many parameters involved in the determination of abundances. To end up with an accurate result, it is crucial to put emphasis on appropriately considering all of them. This is the motivation of this work and it represents a first step towards a reliable determination of the solar abundances. Several conclusions can be extracted from our work:

- We have used a very flexible generative model that contains seven parameters. Some of these parameters are nuisance parameters that are of no diagnostic interest but which are necessary for a good modeling of the spectral line. Including these nuisance parameters and marginalizing over them is crucial for a reliable determination of abundances.
- Including nearby spectral lines turns out to be very important, because they modify the continuum level. We have found that a good characterization of the continuum level in these weak lines is crucial for the inference of abundances.
- We have found some differences when applying exactly the same modeling to different atlases. Therefore, we find it may be convenient to infer solar abundances using the largest panoply of observations. However, we find a reliable oxygen abundance with only 0.003 dex difference between the studies with the two solar atlases.
- A reliable independent determination of the spectral line atomic parameters is very important. Otherwise, this uncertainty propagates accordingly onto the inferred abundances.

Despite the many factors taken into account, we found a good agreement in our results for the oxygen abundance. Thus, we can conclude that, based on the three-dimensional model used, the most probable value for the oxygen

solar abundance is $log(\epsilon_0) = 8.86 \pm 0.04$. This value is classified as a high solar oxygen abundance and is compatible with the results of Grevesse & Sauval (1998).

Finally, it would be very interesting to repeat the Bayesian analysis with other models, whether they are empirical or simulations. For example, we could employ the simulations used in the previous chapter. Moreover, it would be attractive to develope the spectral synthesis with other code as SIR (Ruiz Cobo & del Toro Iniesta 1992) or RH (Pereira & Uitenbroek 2015). On the other hand, the advantage of the Bayesian framework lies in its transparency (every probability distribution in Eq. (3.1) is conditioned on the a-priori information I).

4

A robust determination of the photospheric oxygen abundance

4.1 Introduction

In this chapter, we develop a study to determine the photospheric oxygen abundance using Bayesian inference, in a way similar to that of the previous chapter. However, in this case, we include the novelty of using spatially resolved observations to create the solar three dimensional empirical model in a fully consistent manner. Almost all the previous abundance determinations carried out by different authors are made with observations with limited spatial resolution because of: on one side, the lack of observations; and, on the other side, they use 3D ab initio models, which can only be compared with observations in a statistical way. We carried out slit-spectroscopy observations simultaneously in Fe I and O I spectral lines, thus collecting spectral profiles at many different spatial locations, including granules and intergranular lanes, spanning a temperature range of nearly 1000 K in the photosphere. The methodology employed here combines the best of the two approaches previously discussed: the model is empirical, obtained by fitting the observed Fe I lines, and the model is 3D because each spatial pixel has its own temperature, density and velocity stratification. Another novel ingredient in this approach with respect to previous works is that we do not compare with the average solar spectrum from the FTS atlas observation to derive the overall solar oxygen abundance. Instead, we fit each individual profile, observed at each pixel using the same instrument and configuration as that used to derive the atmosphere, obtaining therefore an oxygen abundance value for each point. Thus, we have two

ingredients that largely improve the analysis: i) the simultaneous observations of Fe I and O I spectral lines to create the model, and ii) the same resolution when comparing synthesis and observations.

4.2 Observations

Our observations have been acquired with the Vacuum Tower Telescope (VTT, Schroeter et al. 1985; von der Lühe 1998) at the Observatorio de Izaña, Tenerife, Spain. The VTT is a solar telescope with two coelostat mirrors at the top of a building of around 38 meters of height. The advantage of having coelostat mirrors is that they allow to obtain a non-rotating image of the Sun. The primary mirror of the telescope has a diameter of 70 cm and a focal length of 46 m. Moreover, the telescope has an adaptive-optics systems (KAOS, von der Lühe et al. 2003; Rimmele & Marino 2011) with a wavefront sensor, a deformable mirror and a high-speed camera. The telescope is shown in Fig. 4.1.

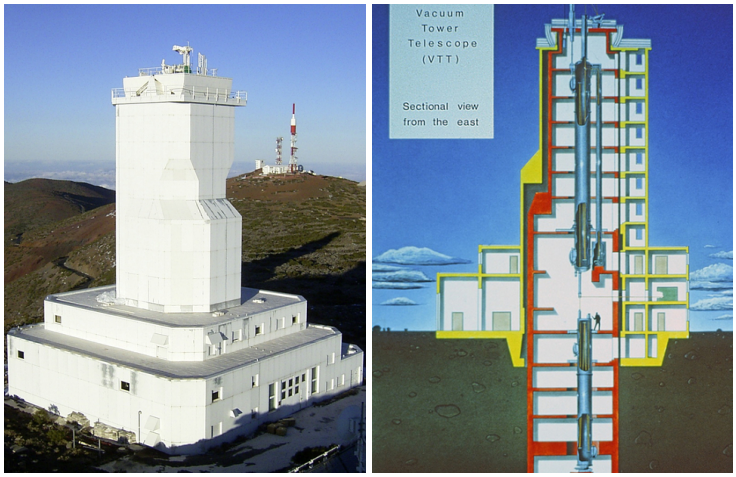

Figure 4.1: Image of the VTT telescope at the Izaña observatory (*left panel*) and squeme of the interior of the telescope (*right panel*). These figures are taken from the website http://www.leibniz-kis.de/en/observatories/vtt/

The VTT have several optical laboratories, we use the Echelle spectrograph. It consists on a grating spectrograph with high spectral resolution of about a

Resolving power at 543.4 nm	0.196
Image scale in primary focus	4.59 arcsec/mm
Aperture ratio f/D	65.7
Focal length	46 m
Diameter of primary mirror	70 cm

Table 4.1: Table with information about the VTT telescope.

million, and a spatial resolution of about 0.5 arcsec at a 500 nm. The slit covers about 200 arcsec on the Sun. Moreover, the VTT is equipped with a slit-jaw camera for observations in white light, Ca K, and Hα. Some numbers are given in Table 4.1; for more information of the telescope see von der Lühe (1998).

The observational data used in this work were acquired on July 15 2016 starting at 11:34 UTC and the exposure time is 200 ms per slit position. The scanning time to cover the entire map was around four minutes (without taking into account the overheads for data saving and slit motion). The observations consist of 2D maps of spectra in a quiet Sun region near active region AR12565 (see the rectangle plotted in Fig. 4.2), located very close to the solar disk center. Pores in the nearby active region were used as targets for the KAOS adaptive optics system to lock on. Following standard procedures, we also took dark current and flat-field images. The standard data reduction procedure was applied, consisting of subtracting the dark current and normalizing by the flat-field images to correct for different pixel sensitivities. The flat-field images are taken with the VTT, due to the telescope has it own system to take solar images without the granulation structure that are used as flat-field images. Wavelength calibration and correction by the prefilter curvature were also applied. Absolute wavelengths were determined by fitting an average disk-center quiet-Sun profile to the FTS atlas (Neckel 1999). The same fit provides the counts to intensity calibration and an estimate of the amount of stray light in the observations. Continuum rectification is done by fitting a third-order polynomial to a few selected continuum windows. The noise estimated in the observations is around 10^{-3} in units of the continuum intensity.

A 2D map at a continuum wavelength in the 6300 Å region and the mean spectrum in the region are plotted on Fig. 4.3. The spectral lines of interest are, from left to right: the [O I] forbidden line that we use to infer the oxygen abundance; a Sc II line used for the calibration of the missing dynamics in the inversions (see next section) and the three Fe I lines that we used to construct the model atmosphere: the two widely-used Fe I lines at 6301.5 Å and 6302.5 Å, and a weak Fe I line at 6303.5 Å. The two narrow spectral lines at 6302.0 Å and 6302.7 Å are telluric contamination from the Earth atmosphere.

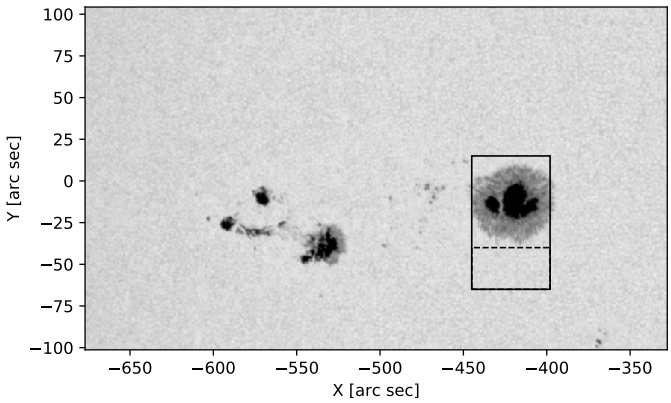

Figure 4.2: Continuum context image of active region AR12565 on July 15 2016. Image from the HMI instrument onboard SDO (Scherrer et al. 2012). Our observations are represented by the solid rectangle in the image. The area under the dashed line correspond to the data taken for this work.

4.3 Model atmosphere

We carry out inversions of the observed spectrum using the NICOLE inversion code, following a similar procedure as in the previous chapter, but in this case we only used one cycle. The inversions are done independently in 40 different pixels, which are the pixels marked in Fig. 4.3 (left panel). Pixels belonging to granules are marked in green while these assigned to intergranular lanes are marked in pink. We did not use all pixels in the image because we wanted to reduce the computation time and, at the same time, having a sample that was statistically valid. The pixels were selected by their brightness in the continuum, choosing the among the brightest and darkest in the field of view. This selection will enhance any possible difference between granules and intergranules. Thus, from the inversions, we obtain 40 different oxygen abundance determinations which can then be compared amongst each other. As the inversion is done pixel by pixel, the resulting model is spatially-resolved with a spatial resolution of 0.8 arc sec per pixel. As in Socas-Navarro (2015) we also have the problem that the model is derived mainly from relatively strong lines, which present reduced sensitivity to velocity in the lower layers (near the continuum) where the [O I] line is formed. For that reason we add

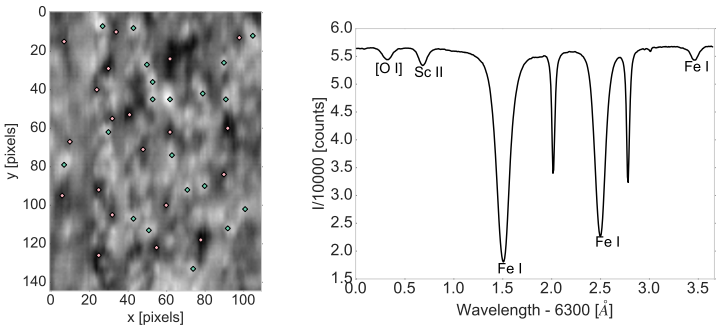

Figure 4.3: Continuum map (*left panel*), marking the position of the pixels considered for this study: granules in green and intergranular lanes in pink (40 pixels in total). As usual, they were selected by their brightness in the continuum, choosing the brightest and darkest in the field-of-view. The average spectrum in the field of view (*right panel*) shows the lines of interest in our work.

the weak Fe I line at 6303.5 Å to constrain the relevant dynamics that might have been missed by the stronger lines. We have an advantage over the Hinode observations used by Socas-Navarro (2015) because this line is out of their spectral range. The atomic data used for all transitions in the spectral range is summarized in Table 4.2.

The inversions are performed by using eight nodes for the temperature and one for the Doppler velocity. We did not invert the magnetic field because our observations do not include polarimetry. Since we are working with quiet Sun profiles, we assume that magnetic fields do not strongly affect the intensity profiles. This turns out to be a good approximation according to Borrero (2008); Fabbian & Moreno-Insertis (2015). We select six nodes for the microturbulence to allow for vertical stratification. This is important because the synthethic Sc II line close to the oxygen feature appears too deep in the model when we compare it with solar atlases, pointing to a lack of dynamics at the base of the photosphere, where these lines are formed. Thus, applying this microturbulence in the model we account for the missing broadening in deepest layers. The inferred temperature stratifications of all considered models are displayed in Fig. 4.4. Granular models are shown in green, while those of lanes are displayed in pink. All of them share a very similar temperature stratification in the range of $\log \tau_{5000}$ (with τ_{5000} the optical depth measured at 5000 Å) between -2.5 and 0.5, which is where the iron lines used are formed.

Ion	λ [Å]	χ_e [eV]	log(gf)	γ_{rad}	γ_{Stark}	γ_{Waals}	σ	α
[O I]	6300.304	0.000	-9.717[a]	0.0	0.05	1.00	...	...
^{58}Ni I	6300.335	4.266	-2.253[b]	2.63	0.054	1.82	...	...
^{60}Ni I	6300.355	4.266	-2.663[b]	2.63	0.054	1.82	...	...
Sc II	6300.678	1.507	-1.970	2.30	0.05	1.30	...	...
Fe I	6301.501	3.654	-0.718[c]	...	...	...	834.4	0.243
Fe I	6302.494	3.686	-1.000	...	...	...	850.2	0.239
Fe I	6303.462	4.320	-2.66	2.40	0.11	1.95	...	...

Table 4.2: Adopted atomic parameters. χ is the excitation potential. γ_{rad}, γ_{Stark} and γ_{Waals} are the radiative, the Stark and the van der Waals damping parameters (units 10^8 $rad\ s^{-1}$). The log(gf) are taken from: [a] Storey & Zeippen (2000), [b] Johansson et al. (2003), [c] VALD database. In the case of the Fe I lines, the γ_{rad} is introduced by NICOLE as calculated in Gray (1976). The log(gf) values for the Sc II and Fe I 6302.5 Å lines have been revised in this chapter.

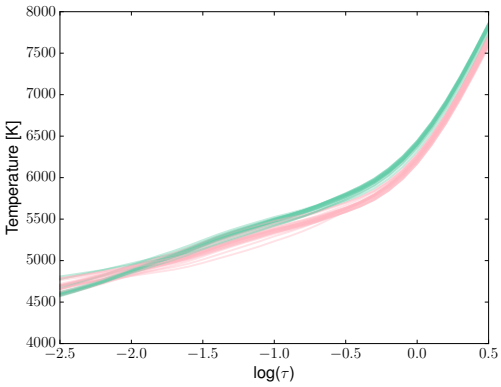

Figure 4.4: Temperature stratification of each inferred model. The optical depth scale is measured at 5000 Å.

However, we found two distinct families where granules show temperatures a little higher than lanes. We note here that our model extends from log τ_{5000}=-7 to log τ_{5000}=2. The quality of the fits is shown for two pixels in Fig. 4.5, where in the top panel we show the inversion of a pixel corresponding to a granule and in the bottom panel an inversion of a lane. For both examples we get an good fit of the three lines.

Once the thermodynamical properties of the 40 pixels are inferred, we build

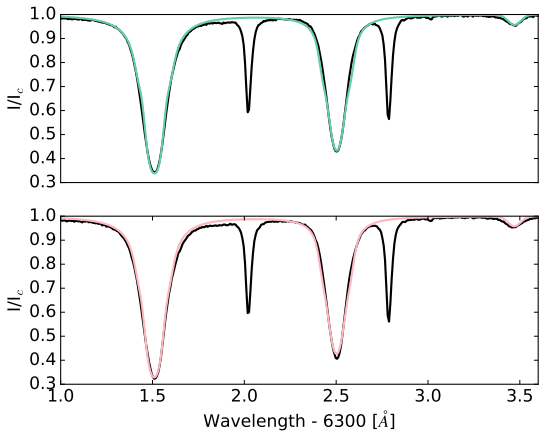

Figure 4.5: Inversions of two spatial pixels. Upper panel: spectral profile of a granule (black) and fit (green). Lower panel: spectral profile of an intergranular lane (black) and fit (pink). I_c is the average quiet Sun continuum intensity.

a grid of synthetic [O I] lines by modifying the solar oxygen abundance in the range [8.50, 9.20] and the nickel abundance in the range [5.80, 6.36]. We considered the two major isotopes ^{58}Ni I and ^{60}Ni I as in Johansson et al. (2003). We sample each interval uniformly with a step of 0.05 for oxygen and 0.04 for nickel. The considered ranges include high and low abundance values as reported in the literature (e.g., Anders & Grevesse 1989; Grevesse & Sauval 1998; Asplund et al. 2009). The results of the synthesis are used as a precomputed database to carry out Bayesian inference using a simulator (O'Hagan 2006). A simulator is a mathematical complex model that is built to simulate the behaviour of a real-world system. The computer program that implements it is also called simulator.

4.4 Bayesian analysis

Similarly to the previous chapter, we apply Bayesian inference (e.g., Gregory 2005) to compute the marginal posterior probability distribution of the oxygen abundance in our 40 models taking into account the information provided by the observations and the priors. The generative model that we use now has the

following form:

$$I_{\rm obs,i} = I_{\rm syn,i}(T_i, v_i, A(O)_i, A(Ni)_i, v({\rm ws})_i, c_i, s_i) + \epsilon_i, \tag{4.1}$$

where i represent each pixel. Thus, the observations can be modeled by a synthetic profile that depend of the temperature and velocity of the model, T and v respectively, and the subsequent parameters: $A(O)$ or $\log(\epsilon_O)$, which is the oxygen abundance (our main parameter of interest); $A(Ni)$ or $\log(\epsilon_{Ni})$, which is the nickel abundance and it is needed to reproduce the line shape because of the blend between oxygen and nickel; a Doppler velocity to introduce a possible wavelength shift due to inaccuracies in the wavelength scale, $v(\rm ws)$; a continuum correction factor c used to set all profiles to the same continuum level; and one parameter s that describes the uncertainty of our observations and the quality of our modeling. We add ϵ_i to the equation to account for the intrinsic noise of our observations. The variance of the noise is given by s^2. All parameters except the oxygen abundance are considered as nuisance parameters and will be marginalized out at the end. For computational reasons, we consider the temperature and velocity of the model without taking into account their uncertainty. We leave carrying out the fully Bayesian approach for the future. Consequently, we take their priors as Dirac deltas, which have no effect when marginalized. The specific priors used in this work for the rest of parameters are specified in Table 4.3. Since we have no clear preference for any value of the oxygen abundance, we choose a flat prior. On the contrary, the nickel abundance is very well determined from previous works and we choose a Gaussian prior with a mean equal to the consensus value and a small dispersion inferred from the results of Scott et al. (2009). The posterior distribution, following the Bayes theorem, is:

$$\begin{aligned} &p(T, v, A(O), A(Ni), v(ws), c, s|D) \propto \\ &p(T, v, A(O), A(Ni), v(ws), c, s)p(D|T, v, A(O), A(Ni), v(ws), c, s), \end{aligned} \tag{4.2}$$

where D are the observations, and the priors can be expressed as

$$\begin{aligned} &p(T, v, A(O), A(Ni), v(ws), c, s) = \\ &\prod_{i=1}^{n} p(T_i)p(v_i)p(A_i(O))p(A_i(Ni))p(v_i(ws))p(c_i)p(s_i), \end{aligned} \tag{4.3}$$

Because we are considering all parameters to be a priori independent.

Parameter	Range	Type
T_i	—	$\delta(T_i$ - $T_{model})$
v_i	—	$\delta(v_i$ - $v_{model})$
$\log(\epsilon_O)$	[8.50, 9.20]	Uniform
$\log(\epsilon_{Ni})$	[5.80, 6.36]	Bounded normal μ=6.17; σ=0.05[a]
v(ws) [km/s]	—	Normal μ=0; σ=2
c factor	—	Normal μ=1; σ=0.2
log(s)	[-3,6]	Uniform

Table 4.3: Prior selected for each parameter of our unpooled Bayesian analysis. [a]taking into account Scott et al. (2009).

We explore two different Bayesian models for our data. In the first one, each pixel is considered independent of the rest (also known as an unpooled model), obtaining the marginal posteriors distribution for the oxygen abundance of each pixel. In the second model, the oxygen abundance is allowed to vary from pixel to pixel but all of them are extracted from a common prior, which is known as hierarchical partial pooling model. As defined in Table 4.4, this common prior is chosen to be a Gaussian distribution, where the hyperparameters are the mean value, μ_O and the standard deviation σ_O. Therefore, in this case, the prior for $A(O)$ depends on the hyperparameters μ_O and σ_O, so that:

$$\prod_{i=1}^{n} p(A_i(O), \mu_O, \sigma_O) = p(\mu_O)p(\sigma_O)\prod_{i=1}^{n} p(A_i(O)|\mu_O, \sigma_O).$$

We note that in this case, the parameter s is also let vary from pixel to pixel and a common prior is imposed as a prior. The probabilistic models are displayed in Fig. 4.6 (left panel corresponding to the unpooled model and right panel to the hierarchical partial pooling model), where all conditional dependences are shown as directed links.

The sampling of the posterior is done with the PyMC3 Python package (Salvatier et al. 2016). It is a package for Bayesian statistical modeling that uses advanced Markov Chain Monte Carlo (MCMC) sampling algorithms to generate samples from the posterior distribution. In this case, we used one of the most advanced, that is based on the Hamiltonian Monte Carlo (HMC). Hierarchical Bayesian models are specially difficult to sample from. HMC-like methods are well suited for this purpose for their ability to generate samples from difficult posteriors. For this reason, we have relied on the no-U-turn (NUTS, Hoffman & Gelman 2014) method coded in PyMC3.

The NUTS sampler automatically tunes the parameters of the HMC algorithm in order to allow for an efficient sampling of the posterior. Thus, it works

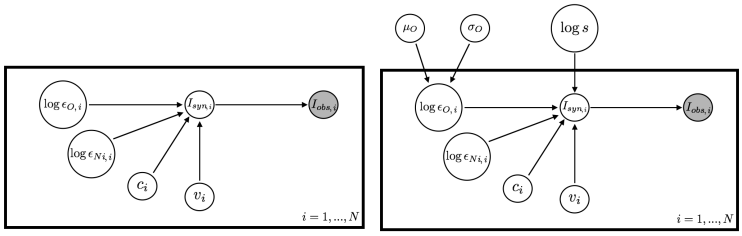

Figure 4.6: Representation of the parameters for the unpooled model (*left panel*) and the hierarchical partial pooling model (*right panel*). For each pixel we have four parameters that contribute to the shape of the synthetic intensity profile. In addition to those parameters, in the hieararchical partial pooling model, we have two hyperparameters: the mean value and the standard deviation of the Gaussian that represent the global oxygen distribution. The parameter s accounts for the uncertainties of our model.

well on high dimensional and complex posterior distributions[1].

Once the posterior is correctly described, we can produce plots like the one shown in Fig. 4.7, where we display the posterior predictive checks, in which the synthetic [O I] line is obtained from different samples from the posterior in the unpooling model for all the granules. Correspondingly, Fig. 4.8 shows the same for intergranular lanes. The noisy observations are displayed in black. The goodness of our model in explaining the observed [O I] line is remarkable. Similar plots are presented in Fig. 4.9 (for the granules) and Fig. 4.10 (lanes) for the hierarchical partial pooling model. Finally, we decided to repeat the hierarchical partial pooling model considering the granules and the lanes together. The plot for this last analysis is shown in Fig. 4.11.

4.5 Results and discussion

4.5.1 Unpooled model

The marginal posterior distributions for the oxygen abundance are shown in Fig. 4.12, where the granules are plotted in green (left panel), and the lanes in pink (right panel). The horizontal line inside the color boxes represents the median value of the marginal posterior distributions, and the color box covers from the first to the third quartile (amounting to 50% probability). The lines going beyond the box extend to show the distribution up to 2 standard

[1]For a precise definition of the NUTS algorithm, see Neal (2012); Hoffman & Gelman (2014); Betancourt (2017).

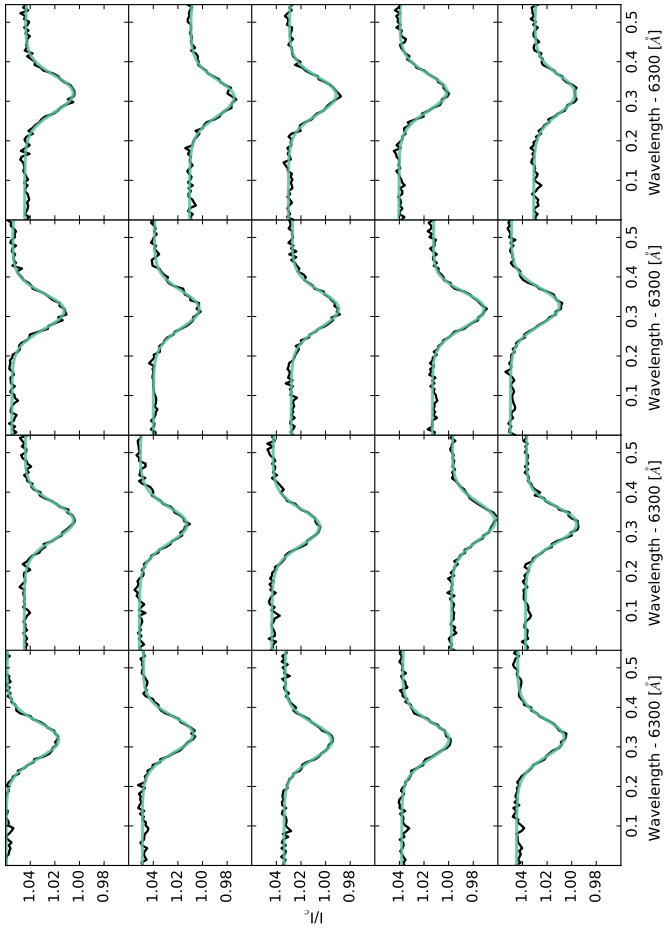

Figure 4.7: Observed (black) and synthetic (green) profiles using values extracted from the posterior for the granules. The continuum took to normalize the intensity is the mean continuum between granules and lanes pixels.

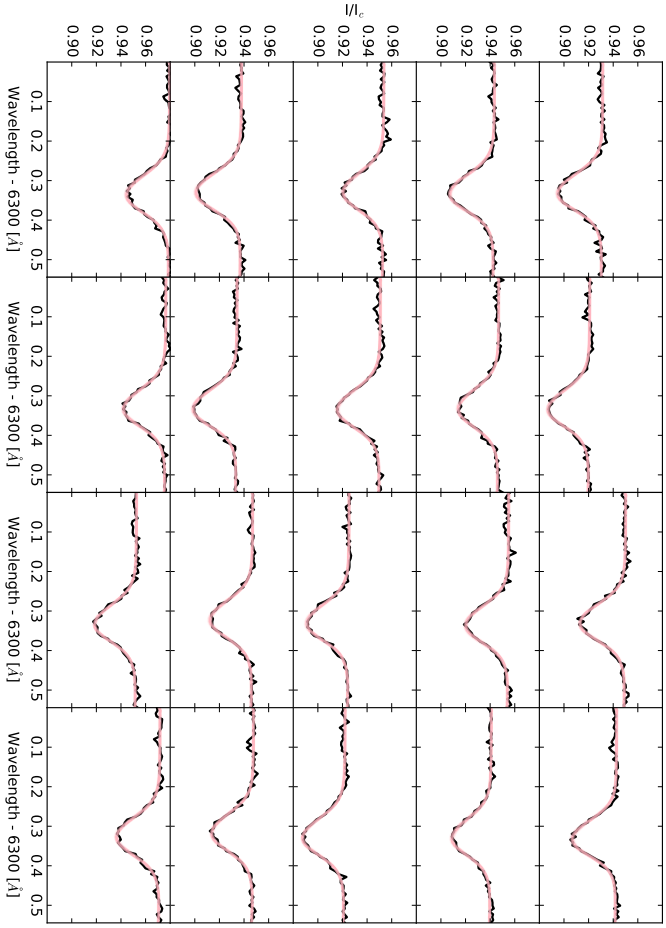

Figure 4.8: Observed (black) and synthetic (pink) profiles using values extracted from the posterior for the lanes. The continuum took to normalize the intensity is the mean continuum between granules and lanes pixels.

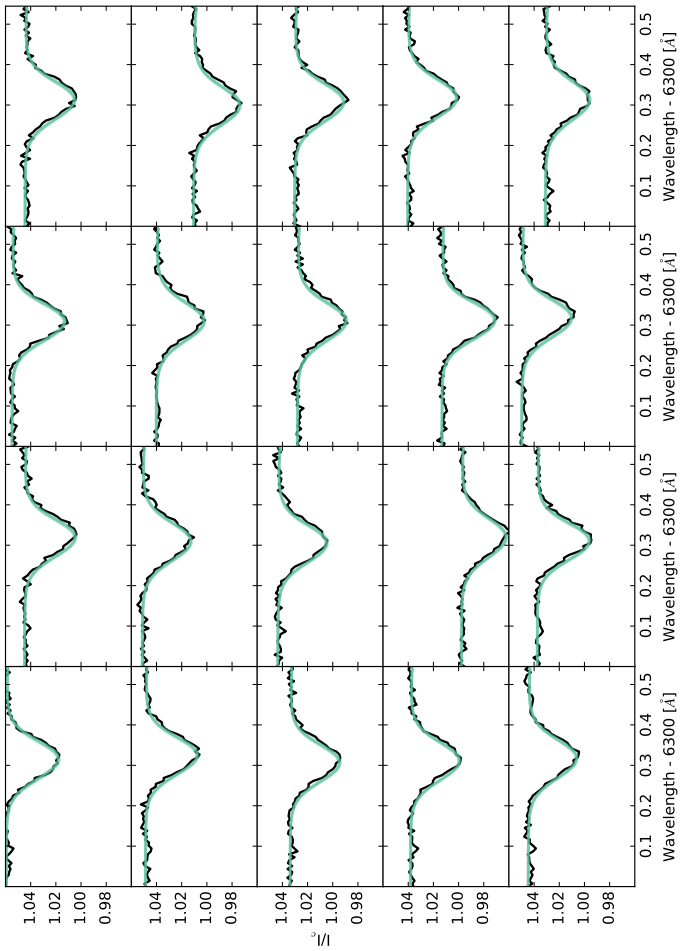

Figure 4.9: Same that Fig. 4.7 but for the hierarchical partial pooling model.

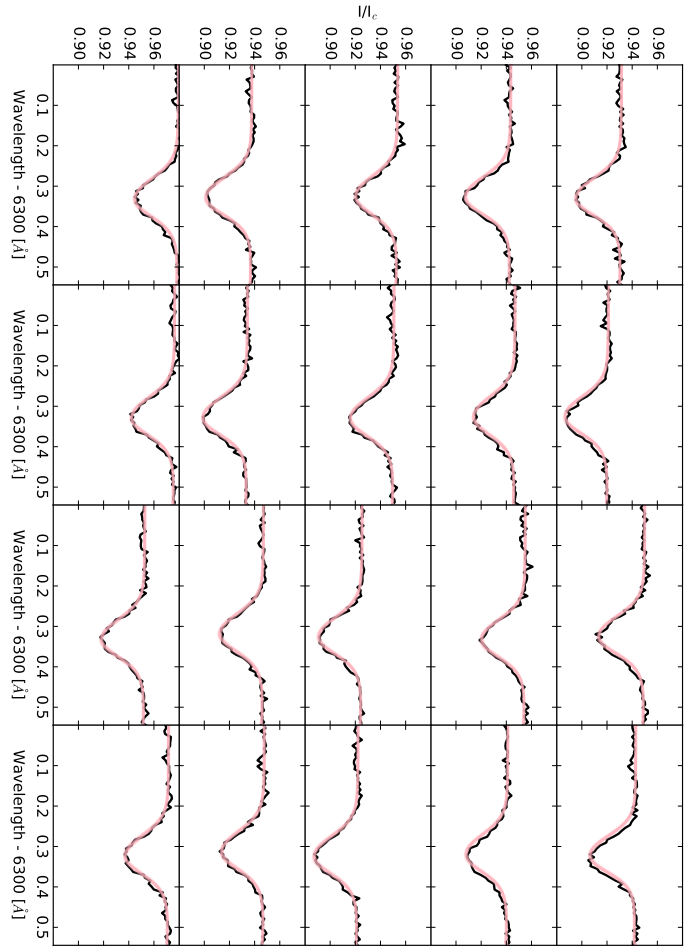

Figure 4.10: Same that Fig. 4.8 but for the hierarchical partial pooling model.

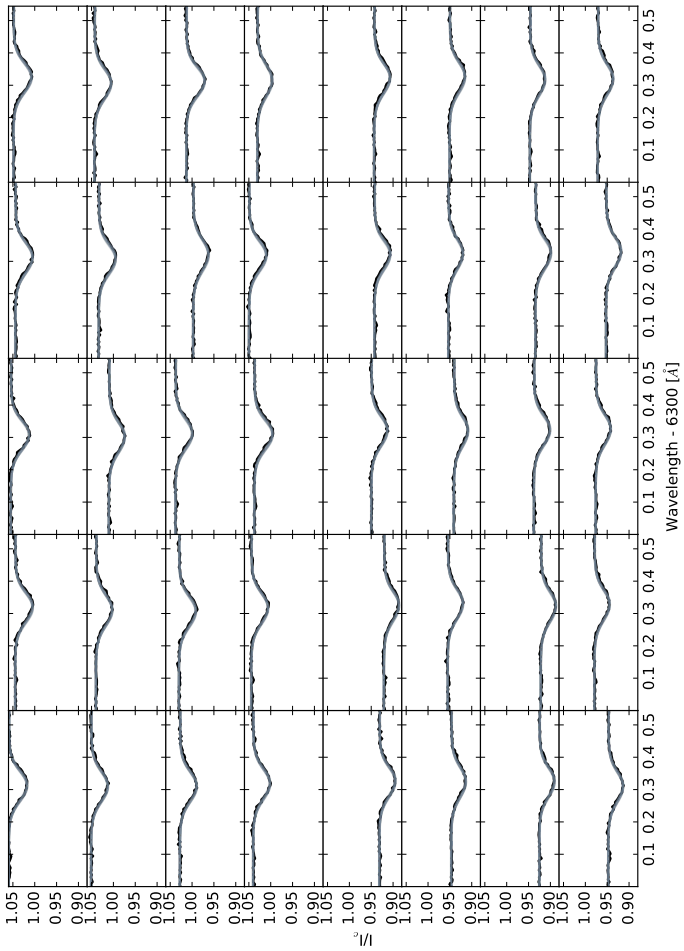

Figure 4.11: Same that Fig. 4.9 and Fig. 4.10 but considering the granules and the lanes together in the Bayesian inference.

Parameter	Range	Type
T_i	—	$\delta(T_i$ - $T_{model})$
v_i	—	$\delta(v_i$ - $v_{model})$
μ_O	[8.40, 9.10]	Uniform
σ_O	σ=1	Half Normal
$\log(\epsilon_O)$	[8.40, 9.10]	Bounded normal μ=μ_O; σ=σ_O
$\log(\epsilon_{Ni})$	[5.80, 6.36]	Bounded normal μ=6.17; σ=0.05[a]
v(ws) [Å]	[-0.2, 0.2]	Bounded normal μ=0; σ=0.1
c factor	—	Normal μ=1; σ=0.2
log(s)	[-3,6]	Uniform

Table 4.4: Prior selected for each parameter of the Bayesian analysis using hierarchical partial pooling model.[a]taking into account Scott et al. (2009).

deviations. The remaining points are determined to be outliers. The horizontal gray line corresponds to the global mean (the mean of the individual means) and the gray area shows one standard deviation.

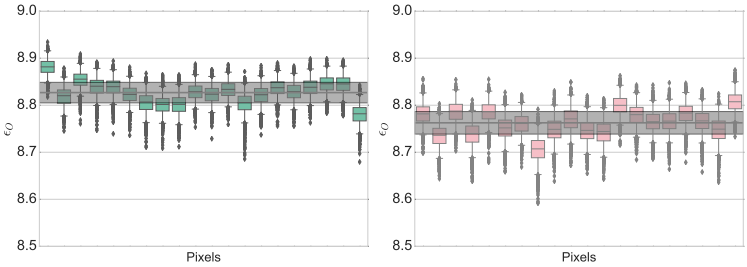

Figure 4.12: Distribution of oxygen abundance for each pixel. Granules are shown in the *left panel* and lanes in the *right panel*. The gray horizontal line represent the mean of the means of each pixel and the gray area represent the standard deviation. The horizontal line inside each color box represents the median value of the marginal posterior distribution, and the color box covers the range encompassing 50% of the probability.

The results show that all 20 granules analyzed independently yield values that are statistically consistent and compatible with the error bars of each individual determination. This also happens with the lanes. Moreover, granules and lanes show results that are compatible within less than two sigmas. This is an indication that the result is robust, because there is no reason to expect that all 40 pixels analyzed would result in the same abundance. In that

sense, this is a consistent determination of the photospheric abundance. The inferred abundance for oxygen in granules is $\log(\epsilon_O)$=8.83±0.02, while it is $\log(\epsilon_O)$=8.76±0.02 for intergranular lanes. These values are obtained computing the means of the individual means in each pixel. Thus, oxygen abundance for the granules is compatible with high metallicity values while oxygen abundance for the lanes is compatible with intermediate metallicity values.

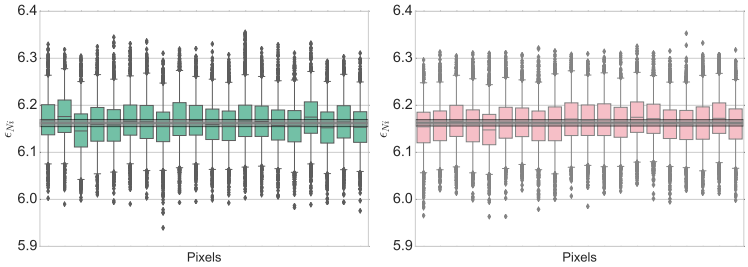

Figure 4.13: Distribution of nickel abundances for each pixel. The gray horizontal line represent the mean of the means of each pixel and the gray area represent the standard deviation. Granules are shown in the *left panel* and lanes in the *right panel*.

The small difference between the oxygen abundance obtained in granules and lanes could be a real effect of the Sun, but we consider that it is more likely a consequence of some systematic effects that were not considered in the study. On one hand, we are considering the model as a perfect representation of the Sun, which is obviously not true: errors in the determination of the temperature and velocity affects considerably to the line shape. Thus, if we repeat the inversions changing the number of nodes or the weight that we give to some region of the spectra, the model that we obtain will surely differ, and therefore, the inferred oxygen abundance. On the other hand, there are also errors in the atomic parameters and other uncontrolled systematic effect that we do no consider here. A possible extension of this work would require exploring all these systematics and include them in the Bayesian analysis.

For completitude, in Fig. 4.13 we show the distribution obtained for the nickel abundance. Here, the marginal posterior distributions are very narrow because the data are extremely consistent with the priors. The mean of the means of the individual pixels is $\log(\epsilon_{Ni})$=6.16±0.01, both for the granules and for the lanes. Therefore, both distributions are totally compatible.

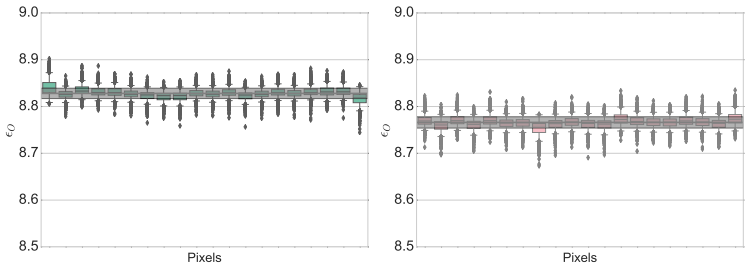

Figure 4.14: Distribution of oxygen abundance for each pixel. The gray horizontal line represent the hyperparameter of oxygen abundance and the gray area covers the probable values between the standard deviation, which is the other hyperparameter. Granules are shown in the *left panel* and lanes in the *right panel*.

4.5.2 Hierarchical partial pooling model

The results of the marginal posterior distribution for the oxygen abundance in the partial pooling model are shown in Fig. 4.14. In this case, the horizontal line represents the mean of the marginal posterior for the hyperparameter μ_O, while the shaded area represents the range from μ_O-σ_O to μ_O+σ_O. The hierarchical model displays a strong shrinkage effect, in which the estimates of the oxygen abundance for individual pixels are pulled towards the group-mean, with a much smaller dispersion. This is a consequence of using hierarchical models. Thus, we find μ_O=8.83±0.01 and σ_O=0.01±0.01 for the granules and μ_O=8.77±0.01 and σ_O=0.01±0.01 for the lanes.

The marginal posterior distributions for the nickel abundance are shown in Fig. 4.15. The mean value obtained is $\log(\epsilon_{Ni})$=6.16±0.03, both for the granules and for the lanes. Therefore the values obtained with the unpooled model for A(O) and A(Ni) are compatible with the values obtained with the hierarchical partial pooling model, which gives more consistency to the results.

As the last experiment, we take into account granules and lanes together in the hierarchical partial pooling model. The aim is to test whether the differences in the results found when they are done separately is a robust result. For this purpose, we use the same prior distribution both for granules and lanes. Fig. 4.16 shows the results for this case, where the marginal posterior distribution for the oxygen abundance is shown in the left panel, and the marginal posterior distribution for the nickel abundance is displayed in the right panel. For this case, the value for the nickel abundance is the same that in the previous inferences, $\log(\epsilon_{Ni})$=6.16±0.02, but the error is smaller. In the case of

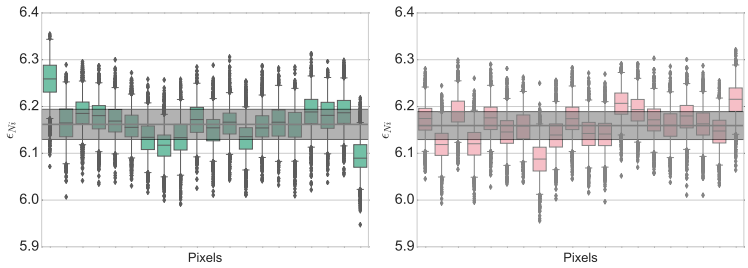

Figure 4.15: Distribution of nickel abundance for each pixel. The gray horizontal line represent the mean value of the mean values for the nickel abundance in each pixel and the gray area covers the probable values between the standard deviation. Granules are shown in the *left panel* and lanes in the *right panel*.

the oxygen abundance, we obtain a distribution where the mean value is in between the values that we were obtaining between granules and lanes, i. e., μ_O=8.80±0.01 and σ_O=0.03±0.01. This value is compatible with high solar metallicity.

Finally, for clarity purposes, Fig. 4.17 shows the posterior distributions for the hyperparameters both in the case of making the hierarchical model of granules and lanes separately (top panels) or together (bottom panels). The left panels show the distribution of oxygen abundances, where in the top panel granules are in green and lanes in pink, and in the bottom panel are all in gray since we do not segregate them. The right panels show the distribution of the standard deviation. In this case, the distribution for the oxygen abundance in the bottom panel is situated in between the distributions for the granules and lanes from the top panel, taking the winds of both distributions. If we focus in the standard deviation panels, we see that in this last case (oxygen and lanes considered together) the uncertainty is larger, but the width of the distributions are the same. Summarizing, in the decision to give a value for the oxygen abundance, we do it giving this last value, that takes into account all spatial location that we consider in our study, as coming from the same prior distribution, i.e., log(ϵ_O)=8.80±0.03. This is a high oxygen abundance value compatible with Grevesse & Sauval (1998).

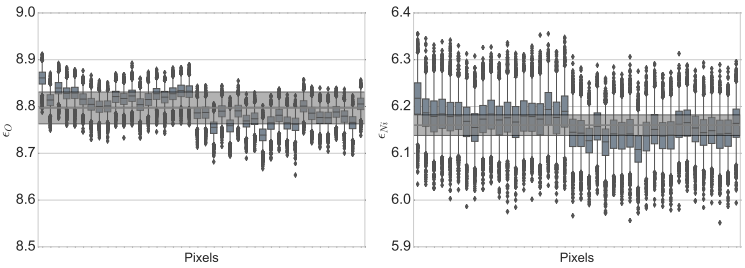

Figure 4.16: Distribution of oxygen abundance (*left panel*) and nickel abundance (*right panel*) for each pixel considering granules and lanes together. For the oxygen abundance, the gray horizontal line represent the hyperparameter of oxygen abundance and the gray area covers the probable values between the standard deviation, which is the other hyperparameter. For the nickel abundance, the gray horizontal line is the mean of the means of nickel abundance in each pixel and the gray area covers the probable values between the standard deviation.

4.6 Discussion and conclusions

In this chapter, we invert observations from the VTT to obtain a three dimensional empirical solar model. After getting the solar model, we synthesize the forbidden oxygen line at 6300 Å to obtain the photospheric oxygen abundance from it. We created a grid of models modifying the nickel and oxygen abundances to get a database of profiles after synthesizing the lines mentioned before with the NICOLE code which is later used in a Bayesian framework.

We made two different Bayesian analysis. The first one consist of doing the inference of each pixel separately, which is known as unpooled model. In this case, we obtained for the oxygen abundance: $\log(\epsilon_O)$=8.83±0.02 for the granules and $\log(\epsilon_O)$=8.76±0.02 for intergranular lanes. Moreover, in the case of the nickel abundance, granules and lanes gave us the same distribution, $\log(\epsilon_{Ni})$=6.16±0.01.

The second analysis uses a hierarchical model considering that the oxygen distribution of all pixels comes from a global Gaussian distribution. It is known as hierarchical partial pooling model and we carry out this inference in two different configurations: first considering granules and lanes independently and second taking all pixels together without distinctions in the inference. In the first case, we achieve the following values for the hyperparameters: μ_O=8.83±0.01 and σ_O=0.01±0.01 for the granules, and μ_O=8.77±0.01 and σ_O=0.01±0.01 for the lanes. Moreover, the nickel abundance is $\log(\epsilon_{Ni})$=6.16±0.03. In the second experiment, we get μ_O=8.80±0.01 and σ_O=0.03±0.01 for the hy-

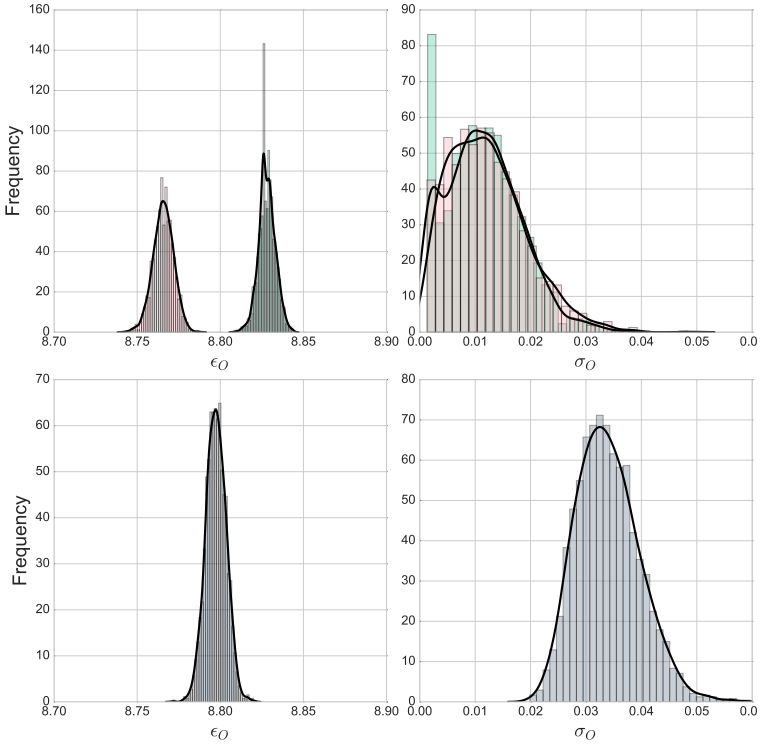

Figure 4.17: Distributions of the hyperparameters for the hiearchical partial pooling model. The *left panels* show the global oxygen abundance and the *right panels* the standard deviation. Top panel is done for the granules (green) and lanes (pink) separately and the bottom panel is done taking all the pixels together.

perparameters and $\log(\epsilon_{Ni})$=6.16±0.02 for the nickel abundance.

We took as a global value for the oxygen abundance the result of the last experiment, as it includes granules and lanes simultaneously, and consider that every pixel comes from a global oxygen distribution that includes all the uncertainties that we may have in determining the abundance value. This result is $\log(\epsilon_O)$=8.80±0.03, which is compatible with the results obtained by Grevesse & Sauval (1998) and the results that we achieved in the previous chapter (see Cubas Armas et al. 2017). Therefore,we infer an oxygen abundance on the high range. However, we note that the results we get in this chapter are strictly dependent on the empirical model obtained with the VTT observations and the radiative transfer of NICOLE. Thus, any change in these two would probably imply a modification in the results. It would be interesting to repeat the procedure using other code to make the spectral synthesis and the inversions. It may be also attractive to use three dimensional HD models instead of an empirical one or even MHD models as the simulations used in the second chapter. Finally, it is obvious that we need more accurate atomic data, and observations to have more reliable results.

5

Conclusions

In this section, we summarize the main conclusions of each chapter of this thesis. Moreover, we make a final remark of which value of what we have obtained for the photospheric oxygen abundance is more reliable.

5.1 Comparison between MURaM and STAGGER simulations of solar faculae

In the second chapter, we analyzed results from 3D MHD simulations of the solar faculae performed by `STAGGER` and `MURaM` numerical codes, and initiated with similar setups. We compared radiative diagnostics synthesized from these results at the grid resolution of the simulations and after these diagnostics are spatially and spectrally smeared to the resolution of the SP/SOT Hinode. In addition, we carried out an analysis of the photospheric oxygen abundance using both simulations. The main conclusions are:

- The results of the two codes show a good agreement, confirming the conclusions of the cross-validation study by Beeck et al. (2012).
- The distribution of physical quantities for the samples of 1D columns that are representative of the cores of the magnetic field concentrations and of the surrounding canopy is nearly identical in the two codes, as well as similar to that derived by Buehler et al. (2015).
- The `MURaM` run is somewhat hotter across almost the whole range of optical depths considered, while the `STAGGER` one has more inclined magnetic fields in the mid photosphere.

- After smearing the radiative diagnostics to replicate the SP/SOT Hinode observations, the differences between the two simulation runs disappear.
- The oxygen abundance value obtained with the `MURaM` snapshots is $\log(\epsilon_O) = 8.66$, which is compatible with the value of Asplund et al. (2004). The corresponding result for the `STAGGER` simulation is $\log(\epsilon_O) = 8.60$. Therefore, with both theoretical three-dimensional MHD models, we achieve an oxygen abundance that is compatible with low solar metallicity.

As a future work related to comparison between solar simulation codes, it would be interesting to compare in detail our synthetic line profiles to those in the raw data acquired by Buehler et al. (2015) as well as those they obtained after inversion/deconvolution. Moreover, comparison with observations obtained with the new 4-meter class of solar telescopes (DKIST, Tritschler et al. 2016; EST, Collados et al. 2013) and eventually with a next-generation space mission for solar data at ultrahigh spatial resolution (Collet et al. 2016) should clarify which (if any of the two) setup provides the most realistic solar simulations of solar faculae. Furthermore, it would be interesting to study the effect of different numerical algorithms, mathematical implementations, and boundary and initial conditions in 3D solar/stellar atmospheric magnetoconvection simulations.

5.2 Uncertainties in the solar photospheric oxygen abundance

In chapter three, we used a three dimensional empirical model to obtain the photospheric oxygen abundance trying to take into account as many sources of uncertainties as possible. To end up with an accurate result, it is crucial to put emphasis on appropriately considering all of them. Several conclusions can be extracted from this work:

- A good characterization of the continuum level in these weak lines is crucial for the inference of abundances.
- We find a reliable oxygen abundance with only 0.003 dex difference between the studies with two solar atlases.
- A reliable independent determination of the spectral line atomic parameters is very important. Otherwise, this uncertainty propagates accordingly onto the inferred abundances.
- Based on the three dimensional empirical model used, the most probable value for the oxygen solar abundance is $\log(\epsilon_O) = 8.86 \pm 0.04$. This value

is classified as a high solar oxygen abundance and is compatible with the results of Grevesse & Sauval (1998).

5.3 A robust determination of the photospheric oxygen abundance

In chapter four, we inverted observations from the VTT to obtain a spatially-resolved empirical solar model. We used 40 spatial locations, 20 corresponding to granules and 20 to lanes, which where selected by their continuum brightness in a quiet Sun area. After obtaining the solar model, we used it to derive the photospheric oxygen abundance by synthesized the forbidden oxygen line at 6300 Å . We computed a grid of spectra varying the nickel and oxygen abundances to obtain a database of profiles with the NICOLE code. We made two different Bayesian analyses. In the first analysis, the inference is done separately for each pixel, an approach known as "unpooled model". We analyzed granules and lanes independently in this approach. The second analysis uses a hierarchical model considering that the oxygen distribution of all pixels follows a global Gaussian distribution. It is known as "hierarchical partial pooling model" and we carried out this inference in two different ways: first considering granules and lanes independently and second taking all pixels at the same time in the inference. The conclusions that we obtain are:

- We obtain results that are compatible between granules and lanes and between the two types of inferences at a level of two sigmas. This is a good level of consistency and coherence and gives us confidence to trust the results.
- Granules exhibit a higher abundance than lanes.
- The abundance obtained for granules is $\log(\epsilon_O)$=8.83±0.02, and for intregranular lanes $\log(\epsilon_O)$=8.76±0.02.
- The hierarchical partial pooling model considering the 40 pixels together is a robust study which gives an oxygen abundance of $\log(\epsilon_O)$=8.80±0.03, which is compatible with the value obtained in the previous chapter and with the values of Grevesse & Sauval (1998).

5.4 Final comments and future work

As a final comment about the oxygen abundance, we recall than in chapter 2 we obtained a low oxygen abundance using three dimensional MHD theoretical codes. However, when we used empirical models, we obtained high oxygen

abundances (chapters 3 and 4). This correlation does not imply causality, as Caffau and colaborators have obtained intermediate metallicity values using models computed with CO^{5}BOLD (Caffau et al. 2015). Therefore, low abundances vs high abundances is not necessarily a matter of theoretical vs empirical models.

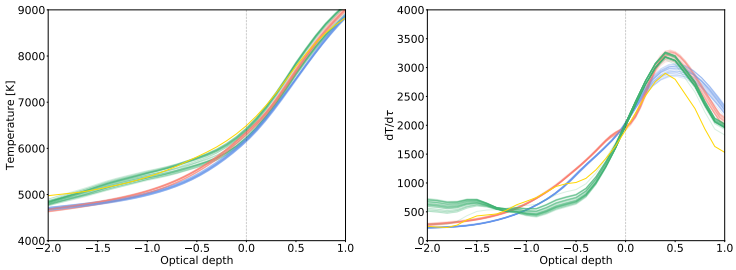

Figure 5.1: Distribution of temperature (*left panel*) and derivative of the temperature respect to τ (*right panel*). The color code is as follow: blue and red lines correspond to the 25 snapshots of `STAGGER` and `MURaM` respectively, the yellow one is for the model used in the chapter 3 of the thesis (the one made from the Hinode observations) and the green ones are from the 40 pixels taken in chapter 4.

The various models are shown in Fig 5.1. The most important parameters in the formation of spectral lines are the temperature and its derivative with optical depth (for a given opacity, a larger derivative results in a stronger line). In this figure, the blue and red lines correspond to the 25 snapshots of the `STAGGER` and `MURaM` simulations respectively, the yellow one is for the model used in Chapter 3 of the thesis (empirical, derived from Hinode observations) and the green ones are from the VTT observations adopted for the inversions in Chapter 4. While the models are qualitatively similar, they are not identical and therefore yield different abundance values.

The temperature is similar in all the models from $\tau = -0.3$ to 1.0, but the empirical models are hotter in the region $\tau = -0.3$ to -2.0, where the inversions are more flat (which is evident in the plot of the derivative of temperature with optical depth). Because of the lower temperature gradient, the synthetic lines computed in the models from the inversions are generally weaker and therefore require higher abundances to fit the observations.

In this thesis we have arrived at different abundance values depending on the model employed. The novel aspect of our work is that, for the first time, we have performed spatially-resolved determinations that lead to a consistent

value (chapter 4). This is therefore, the value that we consider the most realiable, since the error bar accounts for possible systematics in the model. Other forms of abundance determinations rely on the assumption that the model atmosphere is perfectly known and one encounters discrepant values depending on the model choice. With the novel technique employed here, we have made 40 independent determinations in different atmospheres. The Bayesian analysis allows us to properly assess the uncertainties and recommend a value of $\log(\epsilon_O)$=8.80±0.03.

The solar abundance determination is an open topic that has not easy solution. We think there is still much room for improvement to resolve this issue and to end up with a reliable spectroscopic estimation of the solar metallicity. In particular, we think that the following studies could be interesting to pursue:

- One important upgrade in the abundance determinations is to improve the accuracy of the atomic parameters, since the log(gf) of the lines usually have a great uncertainty.
- It could be very interesting to use different spectral lines. In particular, molecular lines and the infrared triplet, which also means to apply non-LTE effects. This could be used to check if the oxygen abundance obtained with different lines are compatible.
- We could determine the oxygen abundance by applying Bayesian inference to synthetic lines made with different theoretical models, and to analyze whether marginalizing out the nuisance parameters the obtained oxygen abundance is compatible among different theoretical three dimensional models.
- The center-to-limb variation introduces valuable information for abundance determination. Consequently, it could be interesting to deal with these observations in a Bayesian framework.
- Another diagnostic that could be made is repeating all inversions and spectral synthesis using another code, such as SIR (Ruiz Cobo & del Toro Iniesta 1992) or RH (Pereira & Uitenbroek 2015), to determine how large is the uncertainty introduced by the code used.
- Finally, we could use the same Bayesian framework to determine the abundances of other abundant elements, like nitrogen or carbon, which also contribute to the CNO cycle. These elements also affect the structure of the stars.

Bibliography

Afram, N., Unruh, Y. C., Solanki, S. K., et al. 2011, A&A, 526, A120

Allende Prieto, C., Lambert, D. L., & Asplund, M. 2001, ApJ, 556, L63

Anders, E., & Grevesse, N. 1989, Geochim. Cosmochim. Acta, 53, 197

André, M. K., Oliveira, C. M., Howk, J. C., et al. 2003, ApJ, 591, 1000

Anstee, S. D., & O'Mara, B. J. 1995, MNRAS, 276, 859

Antia, H. M., & Basu, S. 2006, ApJ, 644, 1292

Asplund, M. 2000, A&A, 359, 755

Asplund, M., & García Pérez, A. E. 2001, A&A, 372, 601

Asplund, M., Grevesse, N., & Sauval, A. J. 2005, in Astronomical Society of the Pacific Conference Series, Vol. 336, Cosmic Abundances as Records of Stellar Evolution and Nucleosynthesis, ed. T. G. Barnes, III & F. N. Bash, 25

Asplund, M., Grevesse, N., Sauval, A. J., Allende Prieto, C., & Kiselman, D. 2004, A&A, 417, 751

Asplund, M., Grevesse, N., Sauval, A. J., & Scott, P. 2009, ARA&A, 47, 481

Asplund, M., Nordlund, Å., Trampedach, R., Allende Prieto, C., & Stein, R. F. 2000a, A&A, 359, 729

Asplund, M., Nordlund, Å., Trampedach, R., & Stein, R. F. 2000b, A&A, 359, 743

Ayres, T. R. 2008, ApJ, 686, 731

Ayres, T. R., Plymate, C., & Keller, C. U. 2006, ApJS, 165, 618

Badnell, N. R., Bautista, M. A., Butler, K., et al. 2005, MNRAS, 360, 458

Bailey, J. E., Nagayama, T., Loisel, G. P., et al. 2015, Nature, 517, 56

Barklem, P. S., Anstee, S. D., & O'Mara, B. J. 1998, PASA, 15, 336

Basu, S. 2009, in Astronomical Society of the Pacific Conference Series, Vol. 416, Solar-Stellar Dynamos as Revealed by Helio- and Asteroseismology: GONG 2008/SOHO 21, ed. M. Dikpati, T. Arentoft, I. González Hernández, C. Lindsey, & F. Hill, 193

Basu, S., & Antia, H. M. 2008, Phys. Rep., 457, 217

Beck, C., Fabbian, D., Moreno-Insertis, F., Puschmann, K. G., & Rezaei, R. 2013, A&A, 557, A109

Beck, C., Fabbian, D., Rezaei, R., & Puschmann, K. G. 2017, ApJ, 842, 37

Beeck, B., Collet, R., Steffen, M., et al. 2012, A&A, 539, A121

Bellot Rubio, L. R., Ruiz Cobo, B., & Collados, M. 2000, ApJ, 535, 489

Bercik, D. J. 2002, PhD thesis, MICHIGAN STATE UNIVERSITY

Bercik, D. J., Nordlund, A., & Stein, R. F. 2003, in ESA Special Publication, Vol. 517, GONG+ 2002. Local and Global Helioseismology: the Present and Future, ed. H. Sawaya-Lacoste, 201–206

Bergemann, M., Lind, K., Collet, R., Magic, Z., & Asplund, M. 2012, MNRAS, 427, 27

Betancourt, M. 2017, ArXiv e-prints, arXiv:1701.02434

Blancard, C., Cossé, P., & Faussurier, G. 2012, ApJ, 745, 10

Borrero, J. M. 2008, ApJ, 673, 470

Buehler, D., Lagg, A., Solanki, S. K., & van Noort, M. 2015, A&A, 576, A27

Caffau, E., Ludwig, H.-G., Steffen, M., et al. 2008, A&A, 488, 1031

Caffau, E., Ludwig, H.-G., Steffen, M., Freytag, B., & Bonifacio, P. 2011, Sol. Phys., 268, 255

Caffau, E., Ludwig, H.-G., Steffen, M., et al. 2015, A&A, 579, A88

Caffau, E., Maiorca, E., Bonifacio, P., et al. 2009, A&A, 498, 877

Carlsson, M., Stein, R. F., Nordlund, Å., & Scharmer, G. B. 2004, ApJ, 610, L137

Cattaneo, F., Lenz, D., & Weiss, N. 2001, ApJ, 563, L91

Centeno, R., & Socas-Navarro, H. 2008, ApJ, 682, L61

Cheung, M. C. M., Schüssler, M., & Moreno-Insertis, F. 2007, A&A, 461, 1163

Christensen-Dalsgaard, J., di Mauro, M. P., Houdek, G., & Pijpers, F. 2009, A&A, 494, 205

Collados, M., Bettonvil, F., Cavaller, L., et al. 2013, Mem. Soc. Astron. Italiana, 84, 379

Collet, R., Criscuoli, S., Ermolli, I., et al. 2016, ArXiv e-prints, arXiv:1612.02348

Criscuoli, S. 2013, ApJ, 778, 27

Criscuoli, S., & Uitenbroek, H. 2014a, ApJ, 788, 151

—. 2014b, A&A, 562, L1

Cubas Armas, M., Asensio Ramos, A., & Socas-Navarro, H. 2017, A&A, 600, A45

Danilovic, S., Gandorfer, A., Lagg, A., et al. 2008, A&A, 484, L17

Danilovic, S., Röhrbein, D., Cameron, R. H., & Schüssler, M. 2013, A&A, 550, A118

Danilovic, S., van Noort, M., & Rempel, M. 2016, A&A, 593, A93

de Wijn, A. G., Stenflo, J. O., Solanki, S. K., & Tsuneta, S. 2009, Space Sci. Rev., 144, 275

Delbouille, L., Roland, G., & Neven, L. 1973, Atlas photometrique du spectre solaire de [lambda] 3000 a [lambda] 10000

Doerr, H.-P., Vitas, N., & Fabbian, D. 2016, A&A, 590, A118

Dunn, R. B., & Zirker, J. B. 1973, Sol. Phys., 33, 281

Ecuvillon, A., Israelian, G., Santos, N. C., et al. 2006, A&A, 445, 633

Fabbian, D., Khomenko, E., Moreno-Insertis, F., & Nordlund, Å. 2010, ApJ, 724, 1536

Fabbian, D., & Moreno-Insertis, F. 2015, ApJ, 802, 96

Fabbian, D., Moreno-Insertis, F., Khomenko, E., & Nordlund, Å. 2012, A&A, 548, A35

Fabbian, D., Simoniello, R., Collet, R., et al. 2017, Astronomische Nachrichten, 338, 753

Feautrier, P. 1964, SAO Special Report, 167, 80

Freytag, B., Steffen, M., & Dorch, B. 2002, Astronomische Nachrichten, 323, 213

Galsgaard, K., & Nordlund, Å. 1996, J. Geophys. Res., 101, 13445

Gingerich, O., Noyes, R. W., Kalkofen, W., & Cuny, Y. 1971, Sol. Phys., 18, 347

Gizon, L., & Birch, A. C. 2005, Living Reviews in Solar Physics, 2, 6

Gray, D. F. 1976, The observation and analysis of stellar photospheres

Gregory, P. C. 2005, Bayesian Logical Data Analysis for the Physical Sciences (Cambridge: Cambridge University Press)

Grevesse, N., Asplund, M., Sauval, A. J., & Scott, P. 2010, Ap&SS, 328, 179

Grevesse, N., & Sauval, A. J. 1998, Space Sci. Rev., 85, 161

Grevesse, N., Sauval, A. J., & van Dishoeck, E. F. 1984, A&A, 141, 10

Grossmann-Doerth, U., Schuessler, M., & Solanki, S. K. 1988, A&A, 206, L37

—. 1989, A&A, 221, 338

Grossmann-Doerth, U., Schüssler, M., Sigwarth, M., & Steiner, O. 2000, A&A, 357, 351

Gustafsson, B., Bell, R. A., Eriksson, K., & Nordlund, A. 1975, A&A, 42, 407

Gustafsson, B., Edvardsson, B., Eriksson, K., et al. 2008, A&A, 486, 951

Haxton, W. C., & Serenelli, A. M. 2008, ApJ, 687, 678

Hoffman, M. D., & Gelman, A. 2014, The Journal of Machine Learning Research, 30

Holweger, H., & Mueller, E. A. 1974, Sol. Phys., 39, 19

Iglesias, C. A., & Rogers, F. J. 1996, ApJ, 464, 943

Illing, R. M. E., Landman, D. A., & Mickey, D. L. 1975, A&A, 41, 183

Johansson, S., Litzén, U., Lundberg, H., & Zhang, Z. 2003, ApJ, 584, L107

Jurčák, J., Martínez Pillet, V., & Sobotka, M. 2006, A&A, 453, 1079

Keller, C. U., Schüssler, M., Vögler, A., & Zakharov, V. 2004, ApJ, 607, L59

Keller, C. U., Steiner, O., Stenflo, J. O., & Solanki, S. K. 1990, A&A, 233, 583

Khomenko, E., & Collados, M. 2007, ApJ, 659, 1726

Khomenko, E., Vitas, N., Collados, M., & de Vicente, A. 2017, A&A, 604, A66

Khomenko, E. V., Shelyag, S., Solanki, S. K., & Vögler, A. 2005, A&A, 442, 1059

Kiselman, D. 1991, A&A, 245, L9

Kosugi, T., Matsuzaki, K., Sakao, T., et al. 2007a, Sol. Phys., 243, 3

—. 2007b, Sol. Phys., 243, 3

Kunasz, P. B., & Olson, G. L. 1988, J. Quant. Spec. Radiat. Transf., 39, 1

Kuridze, D., Zaqarashvili, T. V., Shergelashvili, B. M., & Poedts, S. 2008, Annales Geophysicae, 26, 2983

Kurucz, R. 1993, ATLAS9 Stellar Atmosphere Programs and 2 km/s grid. Kurucz CD-ROM No. 13. Cambridge, Mass.: Smithsonian Astrophysical Observatory, 1993., 13

Kurucz, R. L. 1979, ApJS, 40, 1

Lambert, D. L. 1968, MNRAS, 138, 143

—. 1978, MNRAS, 182, 249

Leenaarts, J., & Wedemeyer-Böhm, S. 2005, A&A, 431, 687

Lind, K., Amarsi, A. M., Asplund, M., et al. 2017, MNRAS, 468, 4311

Lites, B. W., Elmore, D. F., & Streander, K. V. 2001a, in Astronomical Society of the Pacific Conference Series, Vol. 236, Advanced Solar Polarimetry – Theory, Observation, and Instrumentation, ed. M. Sigwarth, 33

Lites, B. W., Elmore, D. F., Streander, K. V., et al. 2001b, in Presented at the Society of Photo-Optical Instrumentation Engineers (SPIE) Conference, Vol. 4498, Proc. SPIE Vol. 4498, p. 73-83, UV/EUV and Visible Space Instrumentation for Astronomy and Solar Physics, ed. O. H. Siegmund, S. Fineschi, & M. A. Gummin, 73

Lodders, K. 2003, ApJ, 591, 1220

—. 2010, Astrophysics and Space Science Proceedings, 16, 379

López Ariste, A. 2002, ApJ, 564, 379

Maiorca, E., Caffau, E., Bonifacio, P., et al. 2009, PASA, 26, 345

Martínez Pillet, V., Lites, B. W., & Skumanich, A. 1997, ApJ, 474, 810

McIntosh, S. W., & Judge, P. G. 2001, ApJ, 561, 420

Meléndez, J., & Asplund, M. 2008, A&A, 490, 817

Mészáros, S., Allende Prieto, C., Edvardsson, B., et al. 2012, AJ, 144, 120

Meyer, D. M., Jura, M., & Cardelli, J. A. 1998, ApJ, 493, 222

Mihalas, D., Dappen, W., & Hummer, D. G. 1988, ApJ, 331, 815

Moll, R., Cameron, R. H., & Schüssler, M. 2012, A&A, 541, A68

Mukherjee, P., Parkinson, D., & Liddle, A. R. 2006, ApJ, 638, L51

Neal, R. M. 2012, ArXiv e-prints, arXiv:1206.1901

Neckel, H. 1994, in Invited Papers from IAU Colloquium 143: The Sun as a Variable Star: Solar and Stellar Irradiance Variations, ed. J. M. Pap, C. Frohlich, H. S. Hudson, & S. K. Solanki, 37

Neckel, H. 1999, Sol. Phys., 184, 421

Neckel, H., & Labs, D. 1984, Sol. Phys., 90, 205

Nordlund, A. 1982, A&A, 107, 1

Nordlund, A. 1984, in Small-Scale Dynamical Processes in Quiet Stellar Atmospheres, ed. S. L. Keil, 174

Nordlund, Å., Stein, R. F., & Asplund, M. 2009, Living Reviews in Solar Physics, 6, 2

O'Hagan, A. 2006, Reliability Engineering & System Safety, 91, 1290

Olson, G. L., & Kunasz, P. B. 1987, J. Quant. Spec. Radiat. Transf., 38, 325

Pehlivan Rhodin, A., Belmonte, M. T., Engström, L., et al. 2017, MNRAS, 472, 3337

Pereira, T. M. D., Asplund, M., & Kiselman, D. 2009a, A&A, 508, 1403

Pereira, T. M. D., Kiselman, D., & Asplund, M. 2009b, A&A, 507, 417

Pereira, T. M. D., & Uitenbroek, H. 2015, A&A, 574, A3

Rempel, M. 2014, ApJ, 789, 132

—. 2017, ApJ, 834, 10

Rempel, M., Schüssler, M., & Knölker, M. 2009, ApJ, 691, 640

Rezaei, R., Steiner, O., Wedemeyer-Böhm, S., et al. 2007, A&A, 476, L33

Riethmüller, T. L., & Solanki, S. K. 2017, A&A, 598, A123

Rimmele, T. R., & Marino, J. 2011, Living Reviews in Solar Physics, 8, 2

Ruiz Cobo, B., & del Toro Iniesta, J. C. 1992, ApJ, 398, 375

Russell, H. N. 1929, ApJ, 70, 11

Salvatier, J., Wiecki, T., & C., F. 2016, PeerJ Computer Science, doi:10.7717/peerj-cs.55

Scharmer, G. B., & Carlsson, M. 1985, Journal of Computational Physics, 59, 56

Scherrer, P. H., Schou, J., Bush, R. I., et al. 2012, Sol. Phys., 275, 207

Schrijver, C. J., & Title, A. M. 2003, ApJ, 597, L165

Schroeter, E. H., Soltau, D., & Wiehr, E. 1985, Vistas in Astronomy, 28, 519

Scott, P., Asplund, M., Grevesse, N., Bergemann, M., & Sauval, A. J. 2015, A&A, 573, A26

Scott, P., Asplund, M., Grevesse, N., & Sauval, A. J. 2009, ApJ, 691, L119

Scott, P. C., Asplund, M., Grevesse, N., & Sauval, A. J. 2006, A&A, 456, 675

Shchukina, N., & Trujillo Bueno, J. 2001, ApJ, 550, 970

Shelyag, S. 2004, PhD thesis, Georg-August-Universität, Göttingen

Shelyag, S., Schüssler, M., Solanki, S. K., & Vögler, A. 2007, A&A, 469, 731

Sigwarth, M. 2001, ApJ, 563, 1031

Sigwarth, M., Balasubramaniam, K. S., Knölker, M., & Schmidt, W. 1999, A&A, 349, 941

Skilling, J. 2004, in American Institute of Physics Conference Series, Vol. 735, American Institute of Physics Conference Series, ed. R. Fischer, R. Preuss, & U. V. Toussaint, 395–405

Socas-Navarro, H. 2011, A&A, 529, A37

—. 2015, A&A, 577, A25

Socas-Navarro, H., de la Cruz Rodríguez, J., Asensio Ramos, A., Trujillo Bueno, J., & Ruiz Cobo, B. 2015, A&A, 577, A7

Socas-Navarro, H., Martínez Pillet, V., & Lites, B. W. 2004, ApJ, 611, 1139

Socas-Navarro, H., & Norton, A. A. 2007, ApJ, 660, L153

Solanki, S. K. 1989, A&A, 224, 225

Solanki, S. K., & Brigljevic, V. 1992, A&A, 262, L29

Stasińska, G., Prantzos, N., Meynet, G., et al. 2012a, in EAS Publications Series, Vol. 54, EAS Publications Series, ed. G. Stasińska, N. Prantzos, G. Meynet, S. Simón-Díaz, C. Chiappini, M. Dessauges-Zavadsky, C. Charbonnel, H.-G. Ludwig, C. Mendoza, N. Grevesse, M. Arnould, B. Barbuy, Y. Lebreton, A. Decourchelle, V. Hill, P. Ferrando, G. Hébrard, F. Durret, M. Katsuma, & C. J. Zeippen, 1–1

Stasińska, G., Prantzos, N., Meynet, G., et al., eds. 2012b, EAS Publications Series, Vol. 54, Oxygen in the Universe

Stein, R. F. 2012, Living Reviews in Solar Physics, 9, 4

Stein, R. F., & Nordlund, Å. 1998, ApJ, 499, 914

Steiner, O. 2000, Sol. Phys., 196, 245

Storey, P. J., & Zeippen, C. J. 2000, MNRAS, 312, 813

Tritschler, A., Rimmele, T. R., Berukoff, S., et al. 2016, Astronomische Nachrichten, 337, 1064

Trujillo Bueno, J., Shchukina, N., & Asensio Ramos, A. 2004, Nature, 430, 326

Tsuneta, S., Ichimoto, K., Katsukawa, Y., et al. 2008, Sol. Phys., 249, 167

Uitenbroek, H. 2001, ApJ, 557, 389

Vernazza, J. E., Avrett, E. H., & Loeser, R. 1976, ApJS, 30, 1

Vitas, N. 2011, PhD thesis, Utrecht University

Vitas, N., Viticchiè, B., Rutten, R. J., & Vögler, A. 2009, A&A, 499, 301

Viticchié, B., & Sánchez Almeida, J. 2011, A&A, 530, A14

Viticchié, B., Sánchez Almeida, J., Del Moro, D., & Berrilli, F. 2011, A&A, 526, A60

Vögler, A. 2003, PhD thesis, Georg-August-Universität, Göttingen

Vögler, A. 2005, Mem. Soc. Astron. Italiana, 76, 842

Vögler, A., Shelyag, S., Schüssler, M., et al. 2005, A&A, 429, 335

von der Lühe, O. 1998, New Ast. Rev., 42, 493

von der Lühe, O. 1998, New Astronomy Reviews, 42, 493

von der Lühe, O., Soltau, D., Berkefeld, T., & Schelenz, T. 2003, in Proc. SPIE, Vol. 4853, Innovative Telescopes and Instrumentation for Solar Astrophysics, ed. S. L. Keil & S. V. Avakyan, 187–193

von Steiger, R., & Zurbuchen, T. H. 2016, ApJ, 816, 13

Wedemeyer, S., Freytag, B., Steffen, M., Ludwig, H.-G., & Holweger, H. 2004, A&A, 414, 1121

Wedemeyer-Böhm, S. 2008, A&A, 487, 399

Wittmann, A. 1974, Sol. Phys., 35, 11

Zwaan, C. 1978, Sol. Phys., 60, 213